# Optical Coherence Tomography and Elastography for Tissue Imaging and Biomechanical Characterization

A Dissertation

Presented to

The Faculty of the Department of Biomedical Engineering

University of Houston

In Partial Fulfillment

Of the Requirement for the Degree

Doctor of Philosophy

In Biomedical Engineering

By

Chen Wu

December 2018

Optical Coherence Tomography and Elastography for Tissue Imaging and Biomechanical Characterization

_____

Chen Wu

Approved:

_____

Chair of the Committee
Kirill V. Larin, Professor,
Department of Biomedical Engineering

Committee Members:

_____

Metin Akay,
John S Dunn Endowed Chair Professor,
Department of Biomedical Engineering

_____

Yingchun Zhang, Assistant Professor,
Department of Biomedical Engineering

_____

David Mayerich, Assistant Professor,
Department of Electrical and Computer Engineering

_____

Irina V. Larina, Assistant Professor,
Department of Molecular Physiology and Biophysics,
Baylor College of Medicine

_____

Suresh K. Khator, Associate Dean,
Cullen College of Engineering

_____

Metin Akay,
John S Dunn Endowed Chair Professor and Chair,
Department of Biomedical Engineering

**Acknowledgements**

Undertaking this PhD has been a truly life-changing experience for me and it would not have been possible to do without the support and guidance that I received from many people.

First and foremost, I would like to express my sincere gratitude to my advisor Prof. Kirill V. Larin for his continuous support of my PhD study and related research, for his patience, motivation, and immense knowledge. He is more than a supervisor to me in providing all the possible help and guidance right from the beginning of my PhD study till the completion of this thesis. Had it not been his challenging and positive attitudes towards my academic and personal life, I could never dream of today.

Besides my advisor, I would also sincerely like to thank the members of my dissertation committee, Prof. Metin Akay, Prof. Irina V. Larina, Prof. David Mayerich, and Prof. Yingchun Zhang for their insightful comments and encouragement, but also for the hard questions which incented me to widen my research from various perspectives.

My time at Biomedical Optics Laboratory (BOL) was made enjoyable in large part due to the many friends and colleagues. I would like to thank Dr. Narendran Sudheendran, Dr. Shang Wang and Dr. Jiasong Li for their detailed guidance and helpful suggestions when I joined the lab. I am thankful to Dr. Salavat R. Aglyamov and Dr. Zhaolong Han for the immense help to my research with their valuable knowledge in mechanics. More specifically, I would like to thank Dr. Manmohan Singh for his endless help in almost every stage of my PhD work. I want to thank Dr. Alexander Schill for all the optical, electrical, and mechanical engineering training which make me a much better engineer. I would like to thank Chih-hao Liu for all the fruitful discussions of various research topics, from which

I have benefited so much. I would also like to extend my gratitude and thankfulness to all other lab mates that include Raksha Raghunathan, Achuth Nair, Justin Rippy, Hongqiu Zhang and Dr. Susobhan Das for working with me and bringing their expertise. None of my work can be achieved without the support of you guys.

Lastly, I would like to express my gratitude to my family for all their love, support and sacrifices. I deeply thank my parents, Xibao Wu and Xumei Zhang for their unconditional trust and endless encouragement. The last word of acknowledgement I have saved for my wife Yutong Li, who went through all the hard times together with me, cheered me on, and celebrated each accomplishment during this challenging period.

Optical Coherence Tomography and Elastography for Tissue Imaging and Biomechanical Characterization

An Abstract

of a

Dissertation

Presented to

The Faculty of the Department of Biomedical Engineering

University of Houston

In Partial Fulfillment

Of the Requirement for the Degree

Doctor of Philosophy

In Biomedical Engineering

by

Chen Wu

December 2018

## Abstract

This dissertation reports the developments of novel methods for tissue imaging and characterization of their biomechanical properties based on optical coherence tomography (OCT) and optical coherence elastography (OCE) techniques. This dissertation focuses on the development of: 1) novel optical imaging techniques for mouse embryonic imaging and; 2) quantitative evaluation of the mechanical properties of biological tissues. The optical embryonic imaging section has two sub-sections: a) development of new technique to extend the OCT imaging depth for mouse embryonic imaging by performing multi-angle scanning and b) demonstration of the feasibility of combining the OCT and selective plane illumination microscopy (SPIM) for more comprehensive murine embryonic tissue characterization. The OCE section is subdivided into three sub-sections: a) investigating the age-related changes in the viscoelastic properties of crystalline lens with a co-focused ultrasound and OCE system; b) investigating the effect of intraocular pressure (IOP) elevation on the mechanical properties of the crystalline lens; and c) utilizing Lorentz force excitation and ultra-fast OCE to quantify tissue biomechanical properties. This dissertation presents advanced imaging techniques to further improve developmental biology research as well as elastography. The results of this dissertation were published in 22 peer-reviewed manuscripts (including 4 as the first author) [1-22].

**Table of Contents**

## List of Figures

## List of Tables

# Chapter 1 - Introduction

## 1.1 Background of optical coherence tomography

Optical coherence tomography (OCT) is a powerful imaging technique [23], which was first introduced for ophthalmological imaging in the early 1990s [24]. Since then OCT has been widely implemented in ophthalmic medical imaging and revolutionized the clinical practice of ophthalmology, because it can perform high resolution, cross sectional, and three-dimensional imaging of tissue in real time. Due to these advantages, OCT has gained wide popularity in several other medical and research fields, such as cardiology, dermatology, and developmental biology [25-28].

The mechanisms of OCT are analogous to ultrasound imaging, but OCT uses light instead of sound waves, and therefore, is capable of much higher resolution imaging. OCT measures the echo time delay of the backscattered light, and two-dimensional cross-sectional images (B-scans) are created by laterally scanning the incident optical beam and collecting the data from separate axial scans (A-lines). Three dimensional datasets are subsequently created by combining B-scans. The volumetric information can be processed and further interpreted for various structural or functional imaging applications.

OCT fills the gap between ultrasound imaging and microscopy, as shown in Figure 1-1. Typical clinical ultrasound imaging has a resolution of 0.1-1 mm depending on the sound wave frequency (3-40 MHz), and it can image deep inside the body due to low attenuation of sound waves in biological tissues [29]. High frequency ultrasound (~100 MHz) has been developed for research and can achieve 15-20 μm resolution [30], but the imaging depth is limited to a few millimeters due to strong attenuation high-frequency waves. In contrast,

confocal microscopy can provide extremely high resolution (< 1 μm), but the imaging depth in biological tissues is limited to ~200 μm [31]. The resolution and imaging depth of OCT fall between ultrasound and confocal microscopy. The axial resolution of OCT is typically from 1 to 15 μm (approximately one or two orders of magnitude better than ultrasound imaging), and the penetration depth is 1 to 2 mm in scattering tissues.

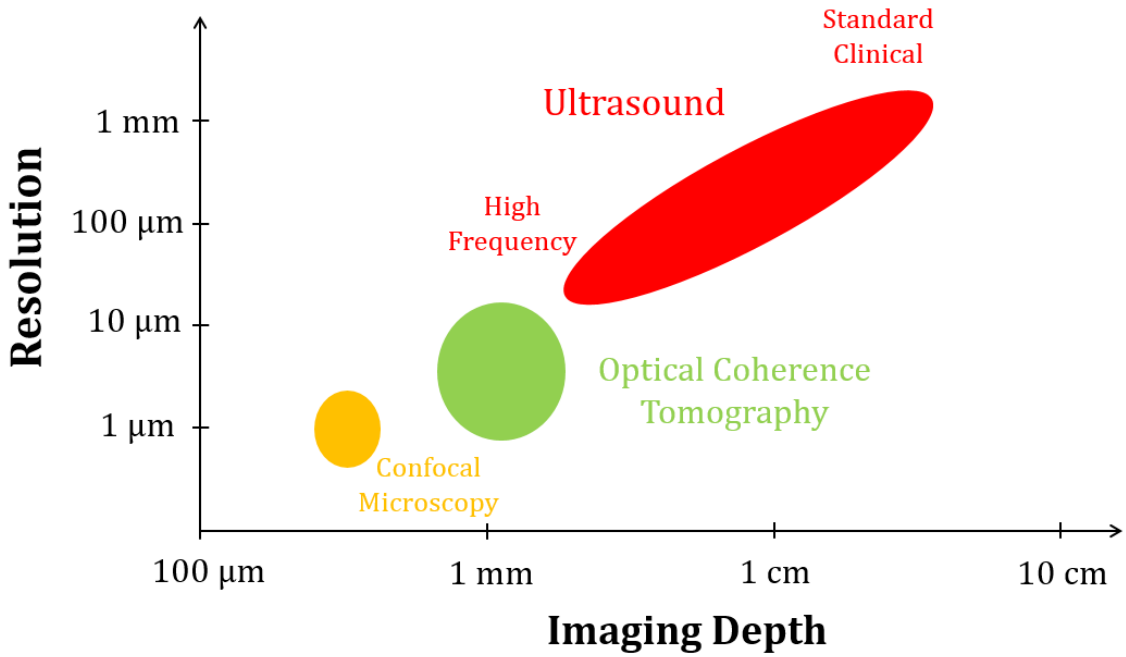


**Figure** 1-1**:** Comparison between OCT, confocal microscopy, and ultrasound imaging.

## 1.2 OCT Theory

The basic principle of OCT imaging is low coherence interferometry (LCI) [32]. LCI was originally implemented for measuring the magnitude and echo time delay of backscattered light [33]. The first biological application of LCI was reported by Fercher et al. in 1988 [34], for measurement of axial length of the eye.

In an OCT system, the light from a low-coherence source is split into two arms of an interferometer. One arm is designated as the reference arm, while the other is the sample

arm. In the reference arm, the light, $E_r$, is reflected by a mirror and it returns into the interference system. The light in the sample arm is directed at the target of interest, and the backscattered light, $E_s$, is collected and interferes with the light from the reference arm. In an inhomogeneous sample, different structures within the sample have different indices of refraction, and light is backscattered when it encounters an interface between materials of different refractive index. The electric field of light, $E$, and the interference pattern recorded by the detector, $I_o$, can be expressed as

$$E = E_0 \cos\left(2\pi ft - \frac{2\pi}{\lambda} z\right) \text{ and} \tag{1.1}$$

$$I_o = \left|E_r + E_s\right|^2 = \left|E_r\right|^2 + \left|E_s\right|^2 + 2E_r E_s \cos\left(2k\Delta l\right), \tag{1.2}$$

where $f$ denotes frequency, $\lambda$ denotes the wavelength of light, $t$ is time, $z$ is the propagation distance, $k$ is the wavenumber, and $\Delta l$ is the optical path length difference between the sample arm and reference arm. Due to the low coherence property of the light, the interference can only be observed when the path lengths of sample arm and reference arm are matched within the coherence length of the light, which is detailed in sub-section 1.3.

There are two main categories of OCT: Time Domain OCT and Fourier Domain OCT.

### **1.2.1** Time Domain OCT

The first implementations of OCT are termed Time Domain OCT (TD-OCT) [35], which acquired the A-line profile by scanning a mirror in the reference arm as a function of time. Figure 1-2 shows a schematic of TD-OCT system based on a fiber optic Michelson interferometer. TD-OCT imaging speed is significantly restricted by the mechanical movement of the mirror in the reference arm. Thus, most TD-OCT systems are limited to a few thousand A-lines per second. Because of the low imaging speed, TD-OCT systems were limited in their capability to image live samples in 3D. For example, in retinal imaging,

not many cross-sectional images can be captured before movements such as blinking cause drastic motion artifacts.

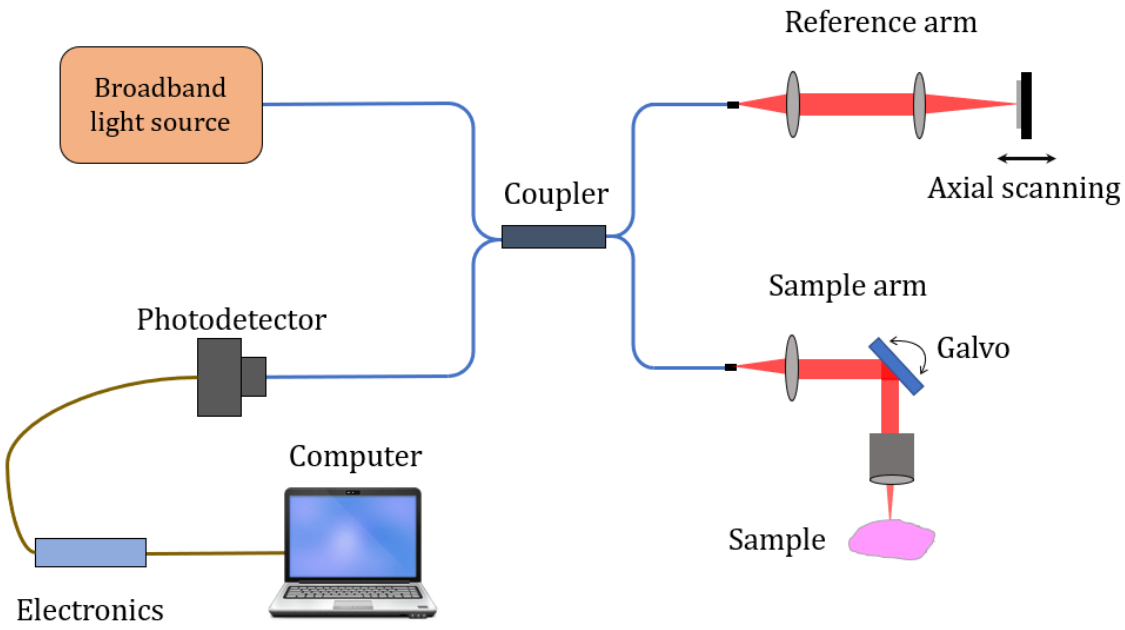


**Figure 1-2**: General schematic of a time domain OCT system.

### 1.2.2 Fourier Domain OCT

In TD-OCT, a depth profile is obtained by mechanically translating the reference arm. In contrast, depth information can be retrieved by detecting the spectral interference signal with a fixed reference mirror in Fourier Domain OCT (FD-OCT). The main advantage of FD-OCT versus TD-OCT is a marked increase in sensitivity and imaging speed [36, 37]. FD-OCT systems can be split into two main schemes: spectral domain OCT (SD-OCT) [38, 39] and swept source OCT (SS-OCT) [40-42]. SD-OCT and SS-OCT share almost same imaging protocols except source operating and detection mechanism.

### 1.2.3 Spectral domain OCT

In SD-OCT, a superluminescent diode is generally used for illumination, and the spectral interference is detected by a spectrometer. Figure 1-3 shows a general schematic of SD-OCT system. The interference spectrum is separated into various spectral lines by a grating and detected by a line-scan detector, which is usually a CCD or CMOS camera. The detected interference signal, $I_D(k)$, can be expressed as

$$I_D(k) = \frac{\rho}{4}[S(k)(R_R + R_{S1} + R_{S2} + ...)] + \frac{\rho}{2}[S(k)\sum_{n=1}^{N}\sqrt{R_R R_{Sn}}\cos(2k(z_R - z_{Sn}))] + \frac{\rho}{4}[S(k)\sum_{n\neq m=1}^{N}\sqrt{R_{Sn}R_{Sm}}\cos(2k(z_{Sn} - z_{Sm}))] \quad , \qquad (1.3)$$

where $k$ is the wavenumber, $S(k)$ is the power spectrum of the light source, $\rho$ denotes the responsivity of detector, $Rs_n$ is the sample reflectivity at $Sn$ layer, $R_R$ is the reference mirror reflectivity, $(z_R\text{-}zs_n)$ denotes the optical path difference between the sample layer and reference mirror, and $(zs_n\text{-}zs_m)$ denotes optical path difference between different sample layers. There are three terms in the interference signal: $\frac{\rho}{4}[S(k)(R_R + R_{S1} + R_{S2} + ...)]$, which is the DC term, $\frac{\rho}{2}[S(k)\sum_{n=1}^{N}\sqrt{R_R R_{Sn}}\cos(2k(z_R - z_{Sn}))]$, which is the cross-correlation term, and $\frac{\rho}{4}[S(k)\sum_{n\neq m=1}^{N}\sqrt{R_{Sn}R_{Sm}}\cos(2k(z_{Sn} - z_{Sm}))]$, which is the auto-correlation term. The DC term is detector current offset, which is independent of pathlength and is proportional to the power reflectivity of the reference mirror plus the sum of the sample reflectivity. The cross-correlation term depends on the light source wavenumber and the pathlength difference between the reference arm and sample arm. This cross-correlation component is typically smaller than the DC component but is the main term of interest for OCT imaging. The auto-

correlation term is due to interference between different layers within the sample, and usually manifests as low-depth artifacts in OCT images.

The OCT A-line profile, $i_D(z)$, can be obtained by inverse Fourier transform of the spectral interference signal and is given by

$$i_D(z) = \frac{\rho}{4}[\gamma(z)(R_R + R_{S1} + R_{S2} + ...)] + \frac{\rho}{4}\sum_{n=1}^{N}\sqrt{R_R R_{Sn}}[\gamma(2(z_R - z_{Sn})) + \gamma(-2(z_R - z_{Sn}))] + \frac{\rho}{8}\sum_{n\neq m=1}^{N}\sqrt{R_{Sn}R_{Sm}}[\gamma(2(z_{Sn} - z_{Sm})) + \gamma(-2(z_{Sn} - z_{Sm}))] \quad , \quad (1.4)$$

where $\gamma(z)$ denotes the inverse Fourier transform of source spectrum, $\rho$ is the responsivity of detector, $Rs_n$ is the internal sample reflectivity at the $s_n$ layer, $R_R$ is the reference mirror reflectivity, and $(z_R\text{-}zs_n)$ is the optical path difference between the reference mirror and sample $s_n$ layer.

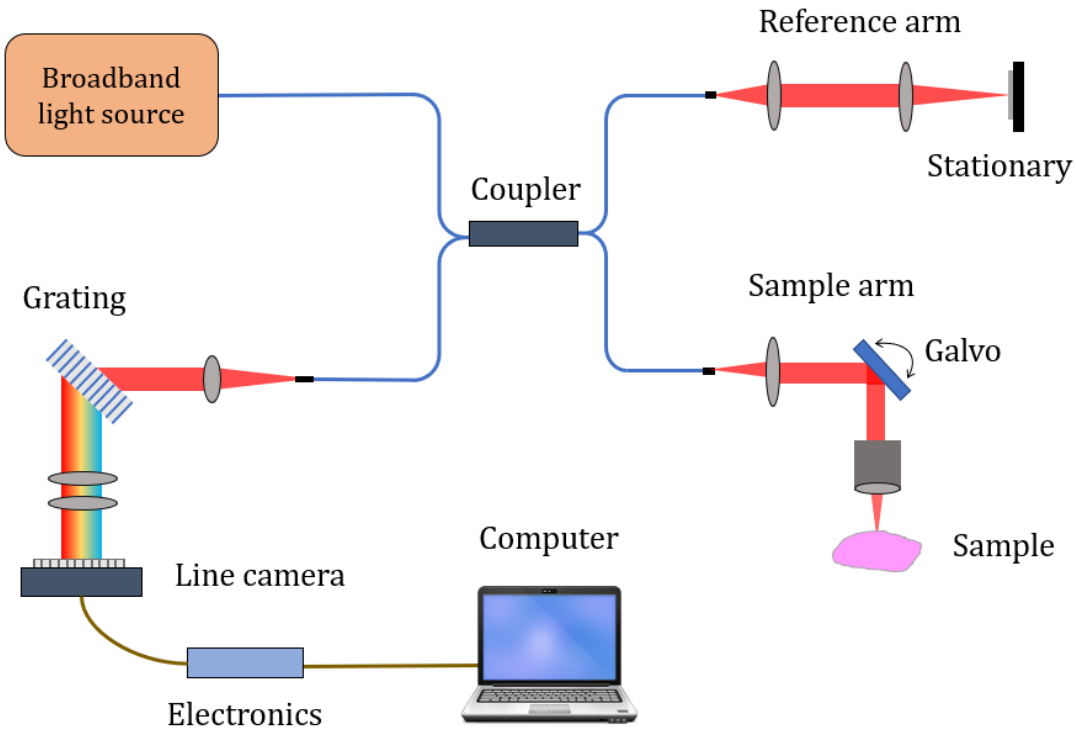


**Figure 1-3**: General schematic of a spectral domain OCT system.

### 1.2.4 Swept source OCT

SS-OCT is the other primary scheme of FD-OCT systems. SS-OCT utilizes a wavelength-tunable laser, which rapidly sweeps through a range of wavelengths. Thus, the spectral interferogram is recorded sequentially in time using a photodetector instead of spectrometer. A separate interferometer, such as Mach-Zehnder interferometer (MZI) [43, 44] or Fabry-Pérot (FP) interferometer [45, 46], can be used to generate a calibration signal for resampling the spectral interferogram linearly as a function of wavenumber, *k*. However, sources can be developed to sweep linearly in wavenumber. After the linearly k-spaced spectrum is acquired, the A-scan can be then obtained by performing a Fourier transform on the linearly k-spaced interferogram as in SD-OCT. Compared to SD-OCT, SS-OCT enables deeper range imaging without compromising the sensitivity at deeper position caused by the SNR roll-off, which is further detailed in sub-section 1.3.3.

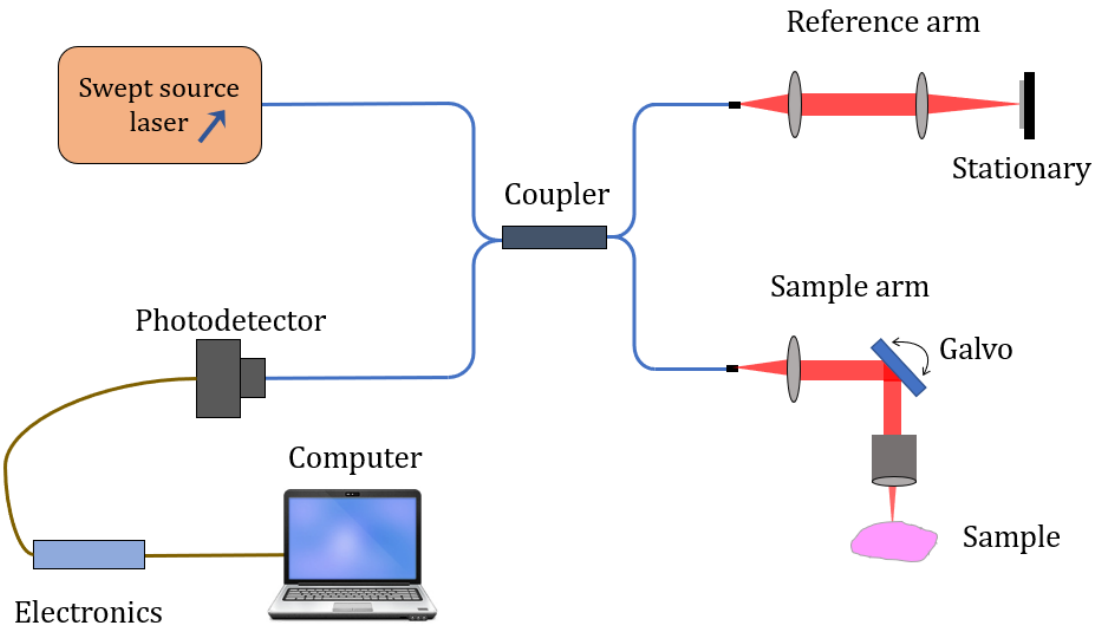


**Figure 1-4**: General schematic of a swept source OCT system.

## 1.3 OCT system parameters

The performance of an OCT system can be characterized by several parameters, which include axial resolution, transverse resolution, imaging depth, signal to noise ratio, sensitivity roll-off.

### 1.3.1 Resolution

The axial and transverse resolution of an OCT system are decoupled. In contrast to conventional microscopy, OCT enables high axial image resolution independent of focusing conditions. The axial resolution is inversely proportional to the spectral bandwidth of the low coherence light source. For a Gaussian profile spectrum, the axial resolution is given by [47]

$$\Delta z = \frac{2\ln 2}{\pi}\frac{\lambda_0^2}{\Delta\lambda}, \tag{1.5}$$

where $\lambda_0$ is the center wavelength, and $\Delta\lambda$ is the full width half maximum (FWHM) of the light source. From equation 1.5, it can be seen the axial resolution is dependent on the light source, and hence high axial resolution can be achieved even with low numerical aperture (NA) optics. Either increasing the spectral bandwidth or decreasing the center wavelength results in an improvement of the axial resolution. However, dispersion mismatch between sample and reference arm can cause deterioration of the axial resolution. Dispersion compensation can be performed optically or numerically [48-50].

The transverse resolution of an OCT system, as in conventional microscopy, is determined by the NA of the imaging optics. The transverse resolution is the diffraction limited spot size on the sample and is given by

$$\Delta x = \frac{4\lambda_0}{\pi}\frac{f_{obj}}{d}, \tag{1.6}$$

where $f_{obj}$ is focal length of the objective lens and *d* is the beam spot size on the objective lens. There is a trade-off between the transverse resolution and depth of focus. The depth of focus is defined as twice the Rayleigh range, $z_R$, by

$$2z_R = \frac{\pi \Delta x^2}{2\lambda_0}. \tag{1.7}$$

### **1.3.2** Imaging depth range

In TD-OCT, the imaging depth of the system is decided by the maximum scanning range of reference arm mirror. Theoretically the imaging depth of TD-OCT could be infinite since the reference arm could be translated to infinity. Compared to TD-OCT, the imaging depth of FD-OCT systems is theoretically governed by two mechanisms: spectral sampling interval (maximum observable depth) and system spectral resolution (signal to noise ratio roll-off as a function of imaging depth). The imaging depth of an FD-OCT system is typically given as

$$\Delta z_{\max} = \frac{\pi}{2\delta_s k} = \frac{N}{4}\frac{\lambda_0^2}{\lambda_{full}}, \tag{1.8}$$

where $\delta_s k$ indicates the spectral sampling interval of FD-OCT system, *N* is the total pixel number of the detector for an SD-OCT system, and $\lambda_{full}$ is the detected full spectral bandwidth. Sensitivity roll-off is the second parameter that limits the imaging depth of FD-OCT system. The signal sensitivity will degrade as a function of imaging depth due to fringe washout. The -6dB falloff depth is given by [51]

$$\Delta z_{-6dB} = \frac{2\ln 2}{\delta_r k}, \tag{1.9}$$

where $\Delta z_{-6dB}$ indicates the imaging depth at which signal to noise ratio is decayed by half and $\delta_r k$ is the spectral resolution of the system. In an SS-OCT system, the instantaneous linewidth of the laser decides the spectral resolution, but it is limited by spectrometer optics in an SD-OCT system. In practice, the imaging depth of and OCT system is primarily limited by the depth of penetration of the light in the sample, which is governed by the optical attenuation of the sample [52].

### **1.3.3** Signal to noise ratio

Signal to noise ratio (SNR), sensitivity, and dynamic range are commonly used to denote the minimum detectable reflected optical power to a perfect reflector for an OCT system. FD-OCT provides better detection sensitivity compared to TD-OCT method. A multi-element array detector (CCD or CMOS) is used in SD-OCT systems in contrast to the single element detector used in TD-OCT, which significantly reduces the shot noise. In a single detector TD-OCT system, the shot noise generated by the power density at one specific wavelength is present at all electronically detected frequencies, and therefore adversely affects the SNR at all other wavelengths. By spectrally dispersing each wavelength to a separate detector, the cross shot-noise term can be eliminated in both hybrid and fully parallel SD-OCT systems.

The theoretical shot-noise-limited SNRs in TD and SD-OCT system, are given respectively by [53, 54]

$$SNR_{TD} = \frac{\eta P_{sample}}{E_{\upsilon} B_w} \text{ and } SNR_{SD} = \frac{\eta P_{sample} \tau_i}{E_{\upsilon}}, \tag{1.10}$$

where $\eta$ = 0.85 for PIN diode in TD-OCT and $\eta$ = 0.28 is the overall detection efficiency of spectrometer in SD-OCT, $B_w$ is electronic detection bandwidth, $P_{sample}$ is the sample

arm power returned to the detection arm, $\tau_i$ is the detector integration time, and $E_\upsilon$ is the photon energy.

### **1.3.4** Sensitivity roll-off

Although the fundamental principle of FD-OCT is determined based on the spectral interferogram and its continuous-time inverse Fourier transform, additional real-world complications will arise due to the practical implementation of FD-OCT. For example, the depth dependent falloff in sensitivity is closely related to the resolution of the interference spectrum, which is decided by the instantaneous linewidth of light source in SS-OCT or spectral resolution of the spectrometer in SD-OCT. The spectral interferogram is acquired by spectrometer that has finite spectral resolution. Therefore, a gradual decay of sensitivity as a function of depth will occur as the fringe visibility decreases at higher spectral interferogram modulation frequencies, which correspond to deeper depths in the sample. The signal roll-off rate, *R*(*z*), is given by [55]

$$R(z) = \left( \frac{\sin \zeta}{\zeta} \right) \exp\left[ -\frac{\omega^2}{2\ln 2} \zeta^2 \right], \tag{1.11}$$

where $\zeta = (\pi / 2)(z / z_{\max})$ denotes the depth normalized to the maximum ranging depth and $\omega = \delta\lambda / \alpha\lambda$ where $\delta\lambda$ is the FWHM spectral resolution of the spectrometer and $\alpha\lambda$ is the wavelength spacing between pixels. The Sinc and Gaussian functions in the equation are related by Fourier transform to the square shape of CCD pixels in the spectrometer and incident Gaussian beam profile on the spectrometer, respectively.

## 1.4 OCT data processing steps

Compared to conventional microscopy, which directly acquires image from a camera, OCT images need to be reconstructed through a series of processing steps. Figure 1-5 illustrates typical data processing procedures for a FD-OCT system.

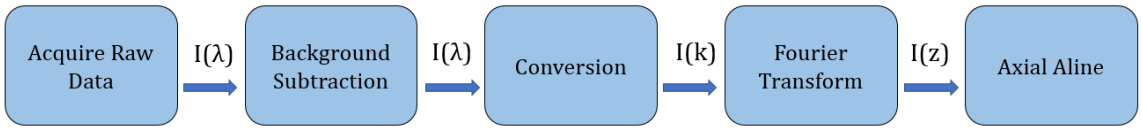


**Figure 1-5**: Typical data processing steps for a FD-OCT system.

1）Acquire raw data:

In SD-OCT, the interference signal is collected by a line-scan camera and digitized by a frame grabber. Since the light is spectrally dispersed by the diffraction grating onto the line-detector array, the intensity data is recorded as a function of wavelength. The spatial distribution of wavelengths on the array can be determined from the spectrometer geometry or by the reference peaks of the light source;

2）Background subtraction:

Background subtraction is essential for removing fixed-pattern noise artifacts in FD-OCT system, which appear as straight lines across the entire OCT image. Such static noise can be produced by many factors, such as the light source spectrum itself or interference between optical elements of the OCT system. Different methods have been proposed to remove this fixed-pattern artifact. The subtraction of a reference spectrum measured in the absence of sample is commonly used for static noise removal [56]. However, frequent noise calibrations may be needed due to the variations in optical phase or polarization, which can make imaging inconvenient. Mean-spectrum subtraction, median-line subtraction, and minimum-variance mean-line subtraction are effective approaches, which take advantage

of signal processing methods to extract reference spectrum and eliminate the need for reference spectrum measurements [56].

3）Conversion from wavelength to wavenumber:

The Fourier transform pair of axial depth, *z*, is complementary to wavenumber, *k*. The conversion of raw signal from the wavelength to wavenumber domain is necessary before the Fourier transform since the OCT signal is linear as a function of wavenumber. Performing Fourier transform on a spectral interferogram that is not linear in wavenumber results in a broad point spread function and subsequent loss of axial resolution. Measured by the spectrometer, *N* sampled points evenly spaced in wavelength are resampled into *N* points evenly spaced in wavelength. Numerous approaches have been proposed to resample the spectra data. The simplest way is to perform basic linear interpolation during resampling, which usually yields sufficient results. Cubic B-spline interpolation is more accurate but is far more computationally expensive [57]. However, the advent of GPU-accelerated processing has minimized the performance penalty. Another commonly used method for spectral calibration is to use a single reflector, which can provide a calibrated reference spectral interferogram. A mapping function from wavelength to wavenumber can then be obtained. In addition to software solutions, hardware solutions, such as linear-in-wavenumber spectrometers, have been developed to eliminate the resampling step. An extra prism can used in the spectrometer to disperse the light evenly in wavenumber, which results in better sensitivity roll-off but also significantly increases system complexity [58, 59];

4）Fourier transform to obtain depth profile:

A Fast Fourier transform (FFT) is performed on the resampled spectral interferogram to reconstruct the axial scan. The depth dependent OCT signal is complex-valued after FFT. The magnitude is often displayed in log scale to display the OCT intensity image since the dynamic range is large. The phase information can be extracted for other functional applications, such as Doppler imaging or optical coherence elastography (OCE) [60, 61].

## 1.5 OCT imaging in developmental biology

One important area of biomedical research that has widely adopted OCT is developmental biology [62]. Embryonic studies are highly valuable for understanding the mechanisms of normal development and congenital defects. Common examples of congenital birth defects include cardiac malformations [63], neural tube defects [64] and Down Syndrome [65]. Birth defects affect 1 in 33 babies and are leading cause of infant mortality in United States, accounting for 20% of all infant deaths in 2015 [66]. Understanding the mechanisms that cause birth defects will help early diagnosis and subsequent interventions. Commonly used animal models for studying human diseases include Zebrafish, fruit flies, frogs, and mice [67-71]. Mouse models are particularly useful because of their genetically similarity to humans, short gestation period, low maintenance cost, and wide availability of transgenic and mutant models [72-74]. Although the genetic basis of several diseases has been identified, corresponding phenotypic information is often lacking. Large scale projects have been initiated to catalog these phenotypes [75], so there is a need for high throughput and high-resolution 3D imaging capable of resolving micrometer-scale features.

A variety of imaging modalities have been employed in mouse embryonic studies, including confocal microscopy, optical projection tomography (OPT), ultrasound biomicroscopy (UBM), and micro magnetic resonance imaging (micro-MRI) [76-79]. However, most of these methods have limitations such as invasiveness, low resolution, or limited penetration depth. Confocal microscopy can image embryos with very high resolution (< 1 μm), but the imaging depth is limited to 100-200 μm [80]. In contrast, UBM and micro-MRI can image deeper structures in mouse embryos [81, 82]. However, the spatial resolution of UBM is limited to ~30-100 μm, and UBM has relatively poor contrast in tissue as compared to optical techniques. Micro-MRI requires extended acquisition periods to obtain images with acceptable contrast, which limits its use for live imaging [79]. Similarly, OPT requires lengthy immobilization and clearing procedures to acquire high resolution 3D images of mouse embryos with high contrast [83].

OCT has been widely adopted for mouse embryonic imaging due to its noninvasive nature, rapid imaging speed, and high spatial resolution [28]. However, compared to transparent ocular tissues, embryo tissue is highly scattering. Therefore, the penetration depth of OCT in embryonic tissue is limited, which is insufficient for imaging embryos at later stages. Another hurdle which limits further application of OCT in embryonic imaging is its inability to target specific tissues, since the contrast of OCT images comes from optical scattering properties of tissues. Tissue differentiation can be performed based on differences in optical scattering [84], but these techniques are not highly specific as with traditional immune-histochemical techniques. This dissertation focuses on the improvement of OCT techniques to overcome these limitations, which will extend the capabilities of OCT for small mammal embryonic imaging.

## 1.6 Optical coherence elastography for tissue biomechanical characterization

Tissues can be characterized based on different properties, such as optical, mechanical, and electrical property [52]. For diseases like the congenital defects, the disease progression and severity could be evaluated by directly analyzing of the normal and abnormal embryonic tissue development using imaging techniques to detect the optical scattering property. In addition to change in optical property, the mechanical properties of tissues can be also drastically altered by diseases. For example, the malignant tumors tend to appear stiffer than benign tumors and normal tissues [85], which suggests that mechanical contrast can enhance disease detection. Hence, manual palpation is routine practice during physical examination. However, manual palpation is subjective, so there is a direct need for imaging techniques that can quantify the biomechanical properties of tissues.

Elastography was formalized in the 1990s and has been widely used to measure the biomechanical properties of tissues [86-89]. The basic principle of elastography is to translate an externally induced tissue deformation to mechanical parameters such as elasticity. Clinically proven elastography techniques include ultrasound elastography (USE) [90] and magnetic resonance elastography (MRE) [91], but the relatively low spatial resolution of these techniques poses a limitation for certain applications, particularly for ocular tissues. Optical elastography techniques have become increasingly more popular for characterizing tissue elasticity with nanometer-scale sensitivity and micrometer-scale spatial resolution [92].

As is discussed in sub-section 1.4, two types of information can be extracted from the OCT signal after Fourier transform: magnitude and phase. The magnitude information is

primarily used for the OCT structural imaging, but can be also used to perform elastography, usually by cross-correlation based techniques [93]. However, artifacts due to speckle decorrelation and unknown applied stresses result in inaccurate results. In contrast, the phase information can be utilized to obtain the absolute displacement, which enables more accurate and quantitative elastographic imaging [61]. Since OCE is based on OCT, it benefits from the inherent advantages of OCT, such as high resolution, non-invasiveness, and rea-time cross-sectional imaging. In comparison to USE and MRE, OCE is able to image mechanical properties at the micron-scale [94-96]. The development of OCE for different applications results in various excitation techniques that have been proposed, such as the use of piezoelectric actuator for contact excitation [97, 98], the employment of air pulse for noncontact stimulation [99, 100], the utilization of ultrasound for remote loading [3, 101] and so on. However, due to the various application environments of tissues of interest, OCE must often be further adapted to fit specific task at hand.

## 1.7 Organization of this dissertation

This dissertation presents the development of imaging techniques to meet the demand of noninvasive high-resolution tissue characterization. The research focuses on two areas: development of new optical imaging techniques for embryonic imaging and the development of new OCE methods for evaluating the biomechanical properties of tissues.

In Chapter 2, a new methodology named rotational imaging OCT (RI-OCT) is presented, which improves the imaging depth of OCT and enables full body imaging of mouse embryos by multi-angle scanning. In Chapter 3, RI-OCT and selective plane illumination microscopy (SPIM) are combined to provide more comprehensive tissue characterization for mouse embryonic research. In Chapter 4, a co-focused ultrasound-

OCE (US-OCE) system was developed to noninvasively investigate the age-related changes in the biomechanical properties of crystalline lenses. In Chapter 5, the relationship between intraocular pressure (IOP) elevation and biomechanical properties of the crystalline lens is further investigated with the US-OCE system. In Chapter 6, a new stimulation technique based on the Lorentz force is combined with ultra-fast OCE to perform measurements of tissue elasticity. Finally, in Chapter 7, the conclusion of this dissertation is presented with implications for future work.

# Chapter 2 - Rotational imaging OCT for full-Body mouse embryonic imaging

This chapter reports a new OCT imaging methodology, called rotational imaging OCT (RI-OCT), to enhance the imaging range and extend the potential applicability of OCT. Although OCT has been widely adopted to study the development of mammalian embryos, light attenuation in biological tissues remains a challenge and inhibits the study of the structural features of mouse embryos. For RI-OCT, three-dimensional structural imaging of the sample is first performed at different angles, followed by a series of post-processing procedures to obtain the final composited image of the whole sample. The results demonstrate that RI-OCT can improve the visualization of structural features compared to conventional OCT.

## 2.1 Introduction

OCT has been demonstrated to be a useful technique for biological tissues imaging [102]. With the advantages of noninvasiveness, fast imaging speed, non-destructive near infrared illumination and high spatial resolution, OCT has become popular in murine embryonic research [5, 10, 103, 104]. Despite advancements in OCT technology, imaging depth remains a major challenge for studying mouse embryos older than E9.5 (9.5 days post-coitum). Optical clearing method has been proposed to enhance OCT imaging depth in mouse embryos, but the clearing procedures are not yet compatible with live imaging [105].

In this chapter, a novel methodology is developed to overcome the challenge of imaging depth and extend the applicability of OCT [1]. Conventional 3D structural imaging was initially performed at four orthogonal angles. The data sets were then registered into a

single full-body image through a series of post-processing procedures. RI-OCT results show that it effectively improves the imaging depth and enables the complete 3D structure of mouse embryo at stages of E9.5 and E10.5 to be obtained.

## 2.2 Materials and Methods

### 2.2.1 Experimental Setup

The RI-OCT hardware setup includes a SS-OCT system, and a square glass tube mounted on a rotational stage to hold the embryo. A schematic representation of the experimental setup is shown in Figure 2-1. The SS-OCT system has a central wavelength of 1300 nm, bandwidth of 100 nm and A-scan rate of 200 kHz. The axial resolution of the SS-OCT system was 12 μm, and transverse resolution was 10 μm. The quartz tubes utilized in this study were custom-made by Precision Cell Inc. The tube used for E9.5 embryo imaging had an outer width of 5 mm, and inner width of 4 mm. The tube used for the E10.5 embryo had an outer width of 7 mm and inner width of 5 mm. The refractive index of the glass was measured as 1.5.

The laser beam was scanned across the sample using galvanometer-mounted mirrors. The 3D axes (x-,y-, and z-) are depicted in the inset of Figure 2-1. Here, a B-scan (2D image) is set along the xz-plane, which is the horizontal plane. The stage is rotated around the y-axis during RI-OCT image acquisition.

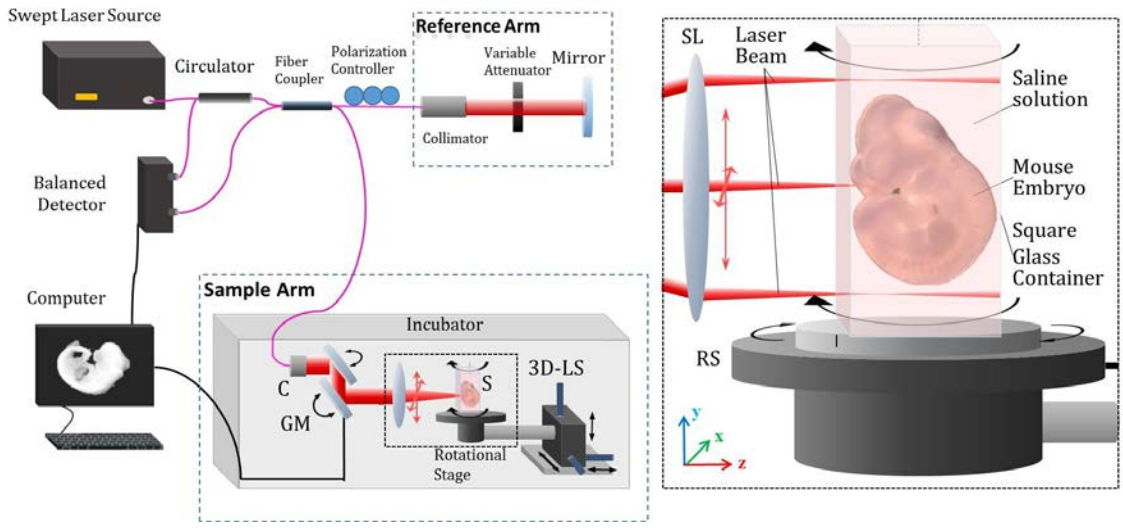


**Figure 2-1**: Schematic diagram for RI-OCT system. C: Collimator; RS: Rotational stage; SL: Scan Lens; LS: Linear Stage; GM: Galvo Mirrors.

### **2.2.2** Mouse embryo preparation

Timed matings of CD-1 mice were set up overnight and checked for vaginal plugs on the following morning. The day on which the vaginal plug was observed was recorded as E0.5. Mouse embryos were dissected at E9.5 stage (9.5 days after a vaginal plug was found) with the yolk sac intact. The embryos were transferred to the square glass tube, which was filled with 0.9% saline solution for imaging. In order to demonstrate the capability of this technique for live embryonic imaging, mouse embryos at E10.5 stage were dissected and kept alive in a culturing medium in a controlled incubator environment. The live E10.5 embryos were then transferred to the square glass tube for RI-OCT imaging.

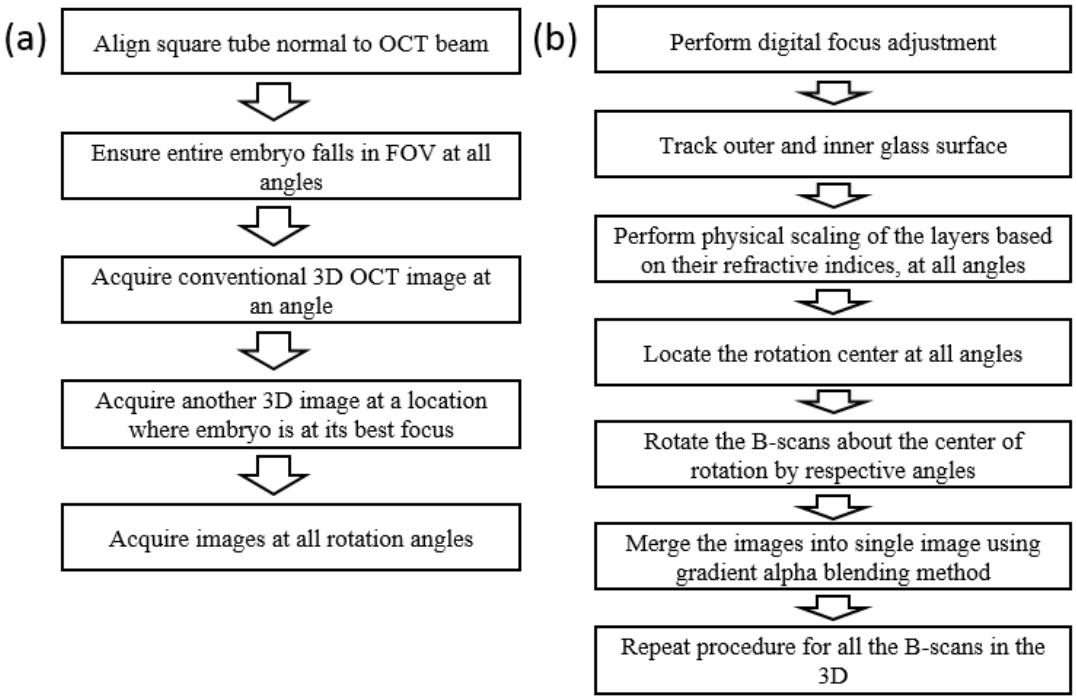


**Figure 2-2**: RI-OCT procedure for (a) imaging acquisition and (b) image construction.

### **2.2.3** RI-OCT imaging procedure

The embryo was placed within the square tube with the coronal and sagittal planes parallel to the walls of the glass tube. This minimized the propagation distance of the OCT probe beam through the embryo, which subsequently decreased light attenuation. The glass tube surface was aligned with the imaging system as shown in Figure 2-1, and conventional 3D OCT images were acquired at four different angles of rotation (0, 90, 180 and 270 degrees).

#### **2.2.3.1** Square tube alignment

The square tube was first placed on the rotational stage as shown in Figure 2-1. The image acquisition flow chart is presented in Figure 2-2(a). First, the glass surface was aligned to be almost normal to the OCT probe beam to reduce any image artifacts due to refraction. The glass surface was set slightly off normal to the beam to avoid direct

reflections from glass surface and subsequent saturation artifacts. Then the tube was aligned so that the embryo was within the field-of-view (FOV) of the OCT imaging system at all four RI-OCT imaging angles.

#### **2.2.3.2** Image acquisition

Image acquisition was performed once the glass tube was aligned. As shown in Figure 2-3(a), if the embryo is out of focus at a particular RI-OCT imaging angle, a conventional 3D image was acquired at the original location. Next, the embryo was brought into focus and another 3D image was acquired. Then, the embryo was moved back to its original location and the stage was rotated by 90 degrees. The entire process was repeated for four orthogonal angles of 0, 90, 180, and 270 degrees.

### **2.2.4** RI-OCT image registration

An algorithm was developed to register the data sets obtained at four angles into a single 3D image (described below).

#### **2.2.4.1** Digital focus adjustment

As mentioned above, conventional 3D OCT images were acquired for every rotation angle at the original position as well as the position where the embryo is in focus. These two images are shown in Figures 2-3 (a) and (b), respectively. In this step, the image of the embryo at its original location was replaced with the image of the in-focus embryo. The resulting image is depicted in Figure 2-3(c). Figure 2-3(c) shows how the in-focus embryo depicted in Figure 2-3(b) is replaced by the in-position embryo in Figure 2-3(a). This process is repeated for each of the four RI-OCT acquisition angles.

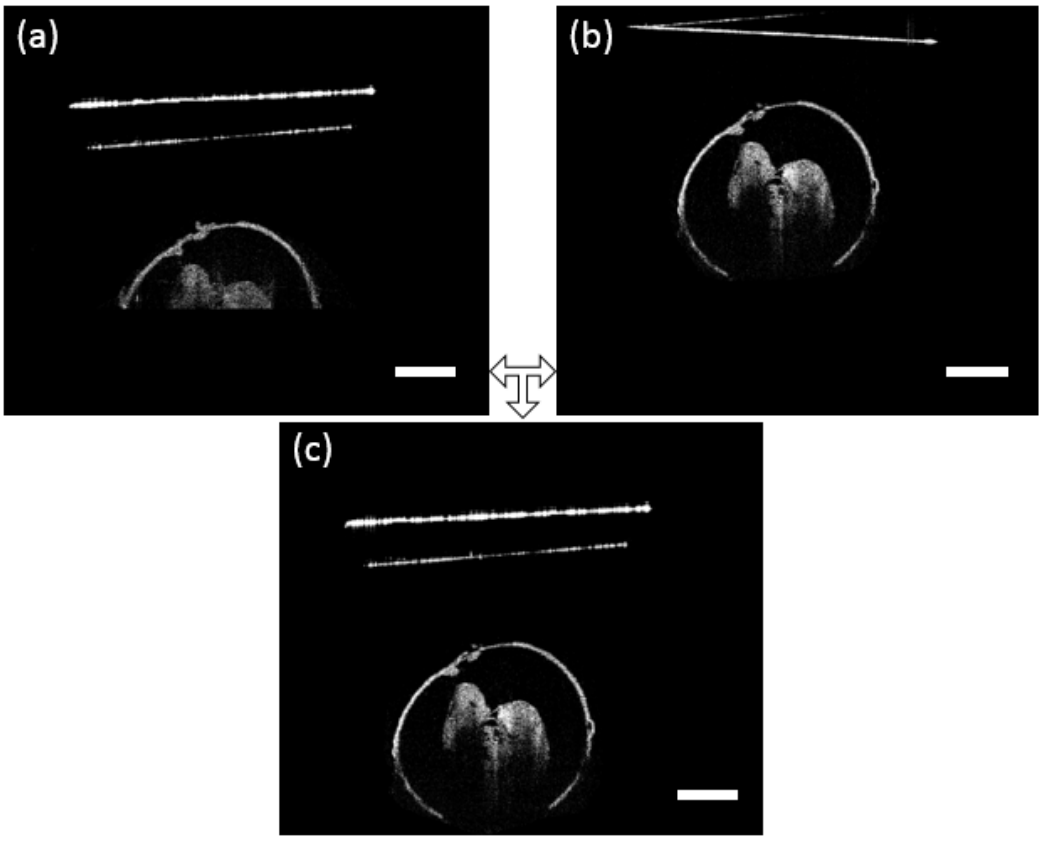


**Figure 2-3**: The OCT images (a) before adjustment, (b) after adjustment, and (c) combination. Scale bars are 500 μm.

#### **2.2.4.2** Physical scaling

Because OCT relies on the optical path difference between the sample and the reference mirror, OCT images are scaled based on the respective refractive indices of the individual components of the sample. Therefore, the images were rescaled to their correct physical dimensions. Each B-scan was divided into regions based on refractive indices. The outer and inner glass surfaces were traced first. The region above the glass tube outer surface is composed of air with refractive index of 1. The region of the glass tube wall assigned refractive index of 1.5. The region below the glass tube inner surface is comprised on saline and the embryo, and the average refractive index was assigned as 1.38. This procedure was performed on images from all four angles.

### 2.2.4.3 Locating center of rotation

Although the glass tube was carefully aligned with respect to the rotation stage, perfect adjustment of the center of the tube along the axis of rotation of the stage is difficult due to effect of optical path. This implies that the center of rotation had to be computed from the OCT B-scans. To accomplish this, a point which could be tracked in two B-scans, before and after rotation, was used to determine the rotation center. In Figure 2-4(a), a point marked as $(x_1,y_1)$ in the OCT B-scan at 0 degrees, could be tracked and is marked as $(x_2,y_2)$ in the OCT B-scan obtained after rotation by 90 degrees. Let $(x_1,y_1)$ and $(x_2,y_2)$ be the points before and after rotation by 90 degrees, respectively, about an unknown center of rotation (m,n), as shown in Figure 2-4(c). The coordinates are defined with respect to the center of the image, (0,0). The point after rotation $(x_2,y_2)$, can be obtained from the initial point $(x_1,y_1)$ rotated about an arbitrary point (m,n) by angle θ, by the following relation,

$$\begin{bmatrix} x_2 - m \\ y_2 - n \end{bmatrix} = \begin{bmatrix} \cos\theta & \sin\theta \\ -\sin\theta & \cos\theta \end{bmatrix} \begin{bmatrix} x_1 - m \\ y_1 - n \end{bmatrix}. \tag{2.1}$$

By using θ = 90 degrees, equation (2.1) can be simplified as

$$m = \left(-x_1 + x_2 - y_1 - y_2\right)/2 \text{ and} \tag{2.2}$$

$$n = \left(-x_1 - x_2 + y_1 - y_2\right)/2 \ . \tag{2.3}$$

The rotation center (m,n) can therefore be determined using equations (2.2) and (2.3).

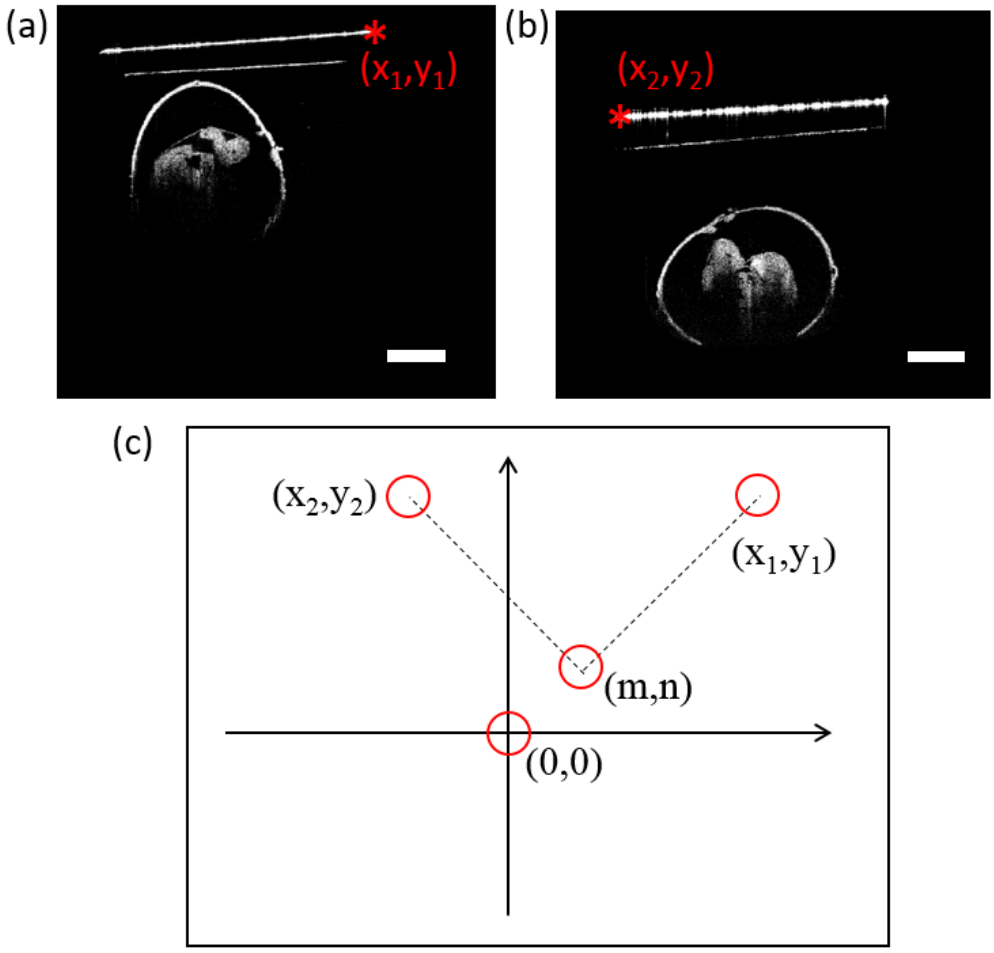


**Figure 2-4**: Locating the center of rotation. (a) Image acquired from 0 degrees; (b) image acquired from 90 degrees; (c) the coordinates from the same position (corner of the tube) and rotation center. Scale bars are 500 µm.

#### **2.2.4.4** Merging images

Once the center of rotation (m,n) was determined, the B-scans obtained at different angles were rotated about (m,n) by the respective angle of rotation. These individual images were then merged to form a single B-scan by gradient alpha blending (feathering) [106]. First, the overlap between two opposing individual images ($I_A$ and $I_B$) were identified, and then the pixel values in the blended regions were weighted and averaged

from the two overlapping images by the coefficients $\alpha$ (alpha mask) which varied as a function of the distance from the seam as described by

$$I_{com}(i, j) = \alpha I_A(i, j) + (1-\alpha) I_B(i, j). \quad (2.4)$$

The gradient blending method minimized the effects of intensity variations on the registration. The entire process was performed on all the B-scans in the 3D OCT stack.

## 2.3 Results

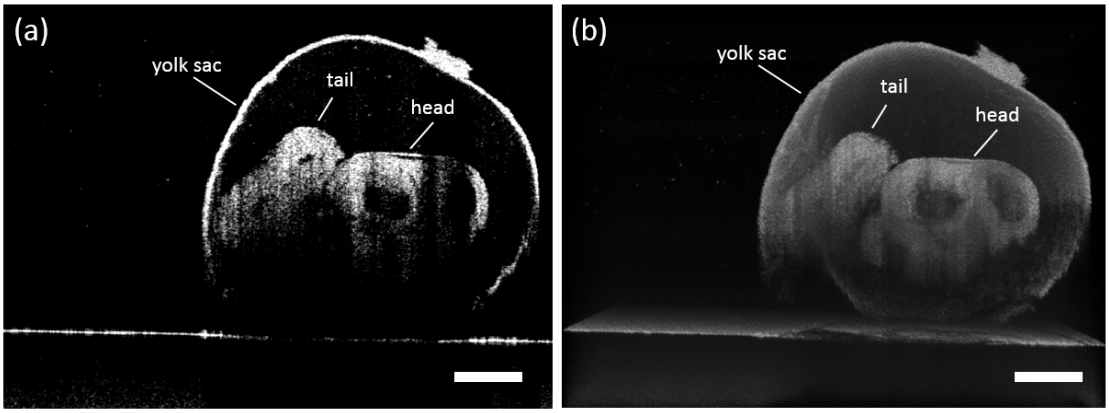


**Figure 2-5**: (a) Cross section image of the E9.5 mouse embryo and (b) 3D OCT rendering of the same embryo. Scale bars are 500 µm.

The typical B-scan and 3D rendering of a mouse embryo at E9.5 obtained using OCT is presented in Figures 2-5 (a) and (b), respectively. The effect of light attenuation in depth is clearly seen. The head and the tail of the embryo are still visible in the image, but the structures below them cannot be seen due to attenuation and subsequent shadowing. Figure 2-6 demonstrates the rotational imaging approach for the same embryo. Figures 2-6 (a), (b), (d) and (e) depict selected cross-sectional OCT images obtained from different angles. The rendering was performed using Amira software. Figure 2-6 (c), (f) and (g) were obtained by combining OCT images from 0 and 180 degrees, 90 and 270 degrees, and all four angles, respectively. Figure 2-6 (h) is a 3D projection of the embryo for the combined

image from all four angles. In the RI-OCT composite obtained from the images acquired at 90 and 180 degrees, shown in Figure 2-6(f), fine structures within the embryo heart are clearly resolvable. Various structures became visible after application of RI-OCT, such as the yolk sac, head, spinal cord, heart and yolk sac vessels. However, these structures are not resolvable from the composite obtained from 0 and 180 degrees, as depicted in Figure 2-6(c). The cross-sectional and 3D projection images of the E10.5 stage embryo from one angle and combined angles are presented in Figure 2-7. The complete brain cavity structure is difficult to discern from a single angle, but it can be clearly visualized in the combined images. Some structures were blurred due to the decidua, but removing the decidua can improve the imaging quality of the final composited image. In the 3D projection view, the embryo and yolk sac structures are labeled as different colors for better visualization. The head and tail are only visible after combining the images. Figure 2-7(e) is a selected frame from the video of E10.5 mouse embryo heartbeat [1]. The heartbeat video was recorded for 4 seconds at frame rate of 250 Hz after RI-OCT imaging. In total, seven heartbeats were observed during this period, which corresponds to a heartbeat of approximately 105 beats per minute and corroborates with previous work [107].

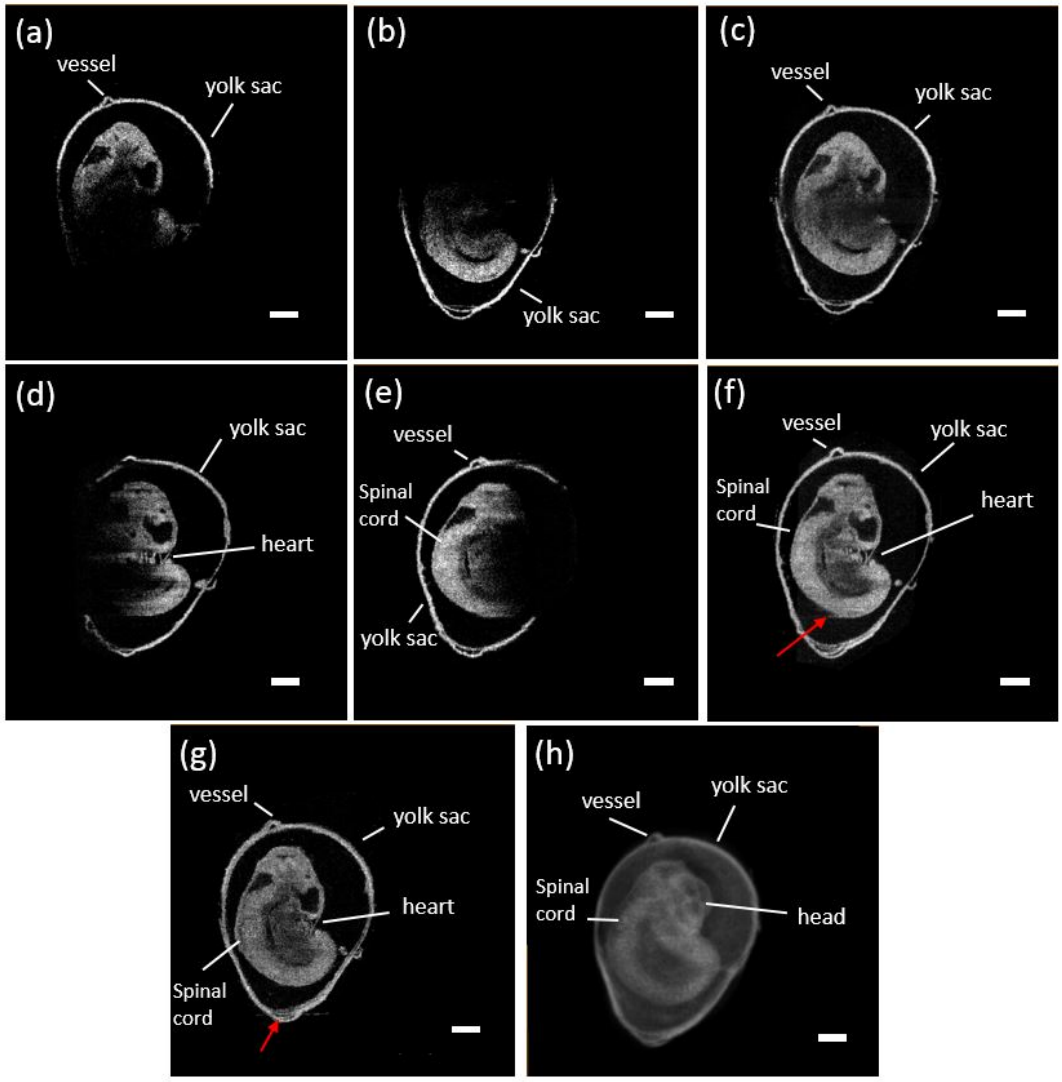


**Figure 2-6**: Selected OCT image at (a) 0 degree, (b) 180 degree, (c) combined composite, (d) 90 degree, (e) 270 degree, (f) combined composite, (g) composite from all four angles, (h) corresponding 3D rendering. Scale bars are 500 µm.

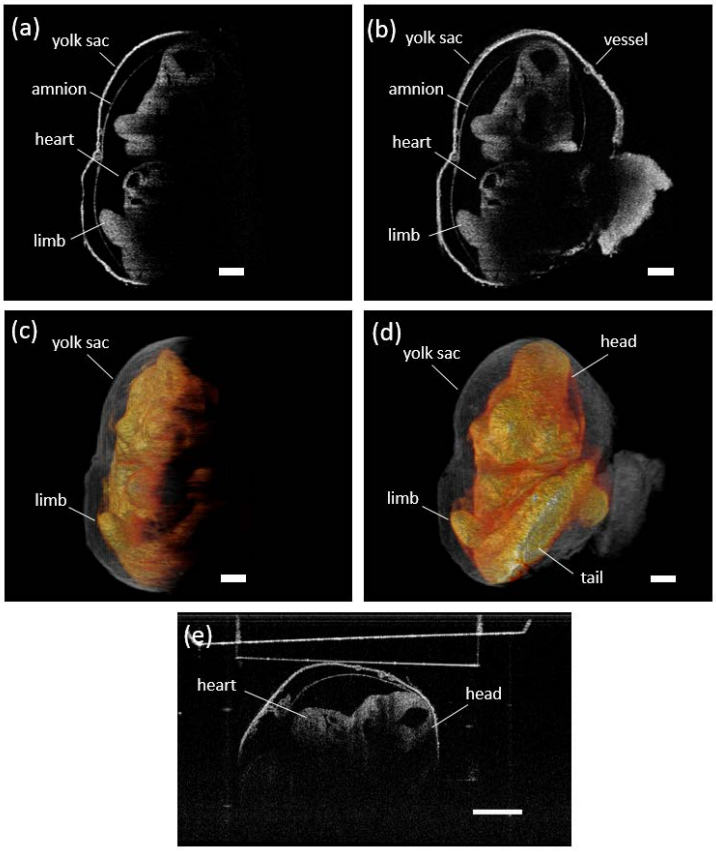


**Figure 2-7**: Selected OCT image at (a) 0 degree, (b) composite from all four angles, (c) 3D rendering at 0 degree, (d) 3D rendering from all four angles, (e) a video frame of the heartbeat of an E10.5 embryo. Scale bars are 500 μm.

## 2.4 Discussion

The main disadvantage of using conventional 3D OCT structural imaging is the loss of SNR and contrast of deeper structures due to light attenuation. Figure 2-5 shows that the deeper structures of a E9.5 mouse embryo within an intact yolk sac cannot be resolved by traditional OCT, even when the sample is in-focus. This necessitates the development of new imaging methods that can be used to obtain complete structural information of the mouse embryo.

As described in this work, the imaging protocol requires conventional 3D OCT images of the in-focus embryo at four orthogonal angles: 0, 90, 180, and 270 degrees. This

procedure ensures that structural information from different parts of the embryo was captured. Using the registration algorithm, images from different angles were reconstructed into a single 3D structural image. The main advantage of this approach is that it overcomes the limited imaging depth of OCT by retrieving structural information from multiple perspectives. A similar concept has also been applied to mouse embryo cardiac phenotyping [108]. In our current setup, a small tilt is introduced between the glass surface and the beam (to avoid specular reflection from the glass surface) that might lead to imperfect overlapping of the images during the registration process. Anti-reflection coating on the glass surface could further reduce specular reflections and minimize the incidence angle. Furthermore, the concavity or convexity of the glass tube will result in convergence or divergence of the OCT probe beam, resulting in imprecise reconstruction of the embryonic structures. Hence, we have utilized a square glass tube to reduce imaging deformation. Precautions should be taken to avoid any displacement of the embryo during this step to minimize blurring and inaccurate registration of the final composited RI-OCT image. There are several methods to help ensure stabilization of the mouse embryo during RI-OCT imaging. For example, the stages were moved very slowly. Additionally, the cuvette can be customized to more precisely match the dimension of embryos at various stages.

The first step during the RI-OCT image registration process (Sub-section 2.2.4) is digital focus registration (Sub-section 2.2.4.1). The glass surface and the embryo must be displaced only along the optical axis. To obtain the correct physical dimensions and locations of the glass tube and the embryo, it is imperative to correctly estimate the refractive index of the glass, saline, and the embryo. This will ensure that the proper

physical dimensions are obtained and utilized in the registration process. The final step is to determine the center of rotation accurately from the images as described in Section 2.2.4.3. The center of rotation was determined using images obtained from successive rotation steps. After rotation of the B-scan images from different angles with respect to the calculated center coordinates, a slight translational offset might be needed to ensure accurate overlapping of the images.

By comparing the combined images (Figure 2-6 (c,f,g)) to the single perspective images (Figure 2-6 (a,b,d,e)), the benefit of RI-OCT is evident. Since in-focus imaging was performed at each angle, embryonic structures imaged at the corresponding angles are clearly visualized in the combined image. For example, the head and tail of the embryo are well-defined in Figure 2-6(c), but fine heart structures are blurred because the heart was positioned deep within the embryo when it was imaged at 0 and 180 degrees. However, the heart was superficially positioned at 270 degrees, so the heart structures were well-resolved as seen in Figure 2-6(f). On the other hand, careful inspection of the regions marked by the red arrows in Figures 2-6(f,g) shows that although the general outline and large structures of the embryo were reconstructed well, there is blurring at the edges due to imperfect overlap in some regions. This suggests that there were minute errors during the image acquisition and registration process, which may not be entirely resolvable. The initial alignment of the cuvette is very important for the final registration. More sophisticated methods can be used to ensure the accuracy of the alignment. For example, an agar phantom containing microbeads can be constructed as a base for the mouse embryo inside the cuvette, and the microbeads can be used as reference for more accurate alignment calibration. The appearance of the same microbeads in images taken at the different angles

would ensure that the same cross-section of the sample was imaged. In this work, a gradient alpha blending method was used to merge the images, but more sophisticated image registration techniques would also improve the image quality of the final composited images.

Figure 2-7 demonstrates the capability of RI-OCT for conducting live mouse embryonic imaging. The current method of whole mouse embryo culture is only able to support *in vitro* development of E5.5-E8.0 embryo for a period of 2-3 days. It is not yet feasible to extend embryonic development *in vitro* beyond the organogenesis stages [109], and therefore mouse embryos younger than E10.5 would be more suitable.

Due to its benefits of whole-body imaging of mouse embryos, RI-OCT could be a powerful tool for phenotyping embryonic structural abnormalities in genetically engineered mice to study developmental diseases such as brain malformation [110, 111] and congenital heart defects [112-114] . The non-invasive nature, relatively rapid imaging speed, and minimal computational complexity means that RI-OCT can provide high-throughput imaging for large-scale phenotyping projects that heavily rely on evaluating phenotypic outcomes.

## 2.5 Conclusion

In this chapter, a new method to visualize a whole E9.5 and E10.5 mouse embryo within their intact yolk sac by combining traditional 3D OCT images obtained at different angles, is demonstrated. From the final RI-OCT image, the whole embryo and yolk sac structure can be visualized. The results demonstrate that RI-OCT was able to significantly improve the OCT imaging depth and contrast of deep structures of mouse embryos, which can benefit future embryonic investigations. RI-OCT could also be combined with other

techniques such as speckle variance for functional analysis of deeper structures, which traditional OCT imaging would be unable to image. In addition, the proposed RI-OCT technique is not limited to mouse embryonic research, it can also be extended to other biomedical research fields which encounter similar issues here.

# Chapter 3 - Comparison and combination of rotational imaging optical coherence tomography and selective plane illumination microscopy for embryonic study

In this chapter, RI-OCT proposed in Chapter 2 is further combined with selective plane illumination microscopy (SPIM) for mouse embryonic imaging, and side by side comparisons are supplemented with co-registered images. Since these two imaging techniques have different contrast mechanisms, they can be used to complement each other and provide more comprehensive tissue characterization for embryonic study.

## 3.1 Introduction

The imaging contrast of OCT is determined by optical scattering properties of tissue. Therefore, OCT can capture structural features by depicting tissue boundaries. OCT can provide important anatomical information for mouse embryonic study. For example, OCT has been successfully utilized to study embryonic heart morphogenesis during the cardiac looping process, to image neural tube closure, and monitor the formation of the brain and limb growth in normal and pathological states [7, 62, 115-117]. Due to light attenuation in tissues, the imaging depth of OCT is limited. In Chapter 2, RI-OCT is proposed to improve the imaging depth by acquiring structural information at four orthogonal angles. This method allows us to effectively image deeper embryonic structures, particularly beneficial for stages E9.5 and E10.5.

In contrast to OCT, fluorescence imaging techniques can acquire biochemical and metabolic information through fluorescent labelling or using transgenic animals. Among all the available imaging modalities, SPIM is a powerful fluorescence microscopic technique for studying murine embryonic development with microscopic resolution and high throughput [118]. For SPIM imaging, a light sheet is constructed to optically section

fluorophore-labelled samples. The resolution of SPIM is comparable to confocal microscopy but imaging speed is much faster. Therefore, SPIM can produce high-quality serial sections with minimal photo-bleaching, which makes it very powerful for three-dimensional imaging [119, 120].

With the advantages mentioned above, SPIM is well suited for longitudinal imaging of developmental processes at multiple scales for investigating early embryogenesis. It has been used in applications such as imaging molecular interactions and gene expression patterns, large fixed specimens and early developmental dynamics [121-123]. Given the different contrast mechanisms, the combination of OCT and SPIM can provide complementary information for a deeper understanding of embryogenesis. Another benefit of combining both RI-OCT and SPIM is that sample rotation can be performed so that each side of the sample is imaged with the highest possible contrast.

In this chapter, we have investigated the feasibility of combining RI-OCT and SPIM for whole body morphological assessment of mouse embryos. Experimental procedures of RI-OCT and SPIM image registration processes are tested and verified with microbeads embedded in agar gel. E9.5 mouse embryos are then imaged via the two techniques for biological study.

## 3.2 Materials and methods

### **3.2.1** OCT and SPIM imaging systems

The schematic of the RI-OCT and SPIM setup is illustrated in Figure 3-1. The detailed description of the RI-OCT setup has been introduced in Chapter 2. The SPIM system was slightly modified from a commercial system (Lightsheet Z.1, Carl Zeiss Microscopy, GmbH, Germany). The system splits fluorescence excitation and detection into two

separate paths, with the detection axis perpendicular to the illumination axis. The sample was illuminated from both sides at 488 nm and 561 nm. The samples were imaged with a 5X air detection objective (Plan-Neofluar N.A. of 0.16), with 5X (N.A. of 0.1) illumination objective, respectively. The axial resolution was 5.2 μm and lateral resolutions was 1.3 μm respectively, at a magnification of 0.7 for the images taken with the 5X objective. The sample cuvette was placed inside a water filled chamber and positioned precisely in three dimensions with piezoelectric actuators. Half the sample was scanned through from one side with dual illumination, then the sample was rotated 180 degrees and imaged from the other side with same settings. The dual illumination and imaging angles were fused after imaging using mean fusion method in Zen 2.1 lightsheet software, where the pixel in the fused image is determined by averaging the intensity level of the pixels for the involved views.

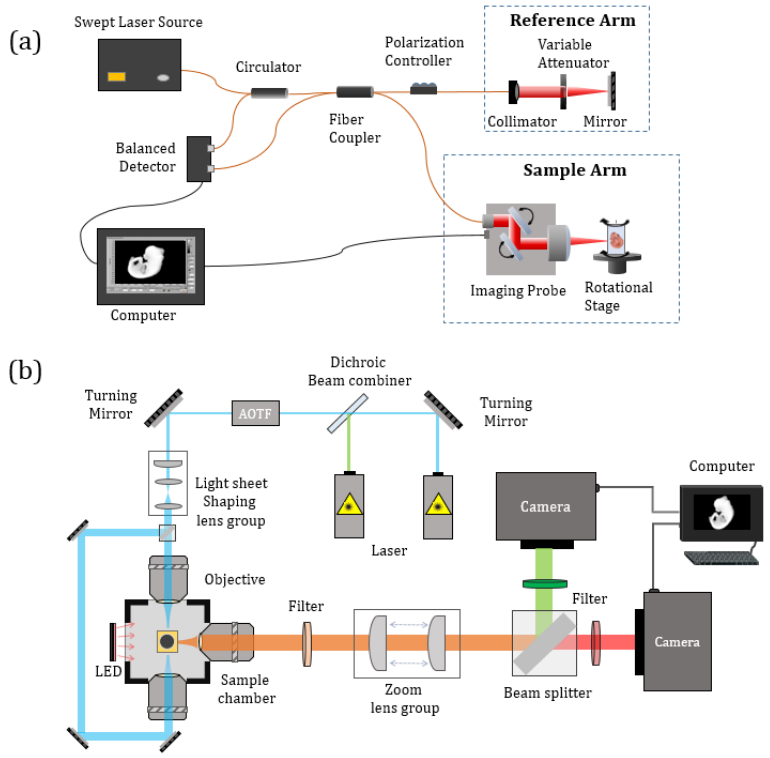


**Figure 3-1**: Schematic of (a) RI-OCT experimental setup and (b) SPIM setup.

### **3.2.2** Phantoms

To investigate the feasibility of multimodal imaging with SPIM and OCT, a phantom was prepared using fluorescence microbeads (various sizes of 10-20μm, 63-75μm, 300-355μm and 500-600μm) distributed in 1% (w/w) agar. The agar was then poured into a cuvette and imaged after hardening using both techniques. Special care was taken to image the phantom at the same position and orientation to ensure precise image registration.

### **3.2.3** Animals

Mouse embryos (strain Tg; ε-globin-GFP) were imaged by both techniques. Tg; ε-globin-GFP is expressed in early erythroblast formation and previously used to study the role of hemodynamic forces during embryonic development [124]. Embryos were dissected out of the mothers at E9.5, and then were fixed for 2h in 4% paraformaldehyde before being permeabilized in 1x PBS + 0.5% Triton X-100 (PBS-T). Non-specific antibody binding was blocked with 2% bovine goat serum in PBS-T for 2h at 4 ºC. Embryos were incubated primary anti-PECAM1 antibody (1:200, Mec13.3, BD Pharmingen) diluted in blocking solution overnight at 4 ºC. Primary antibody was counter stained with Alexa Fluor 568 goat anti-rat secondary antibody (1:500, Invitrogen, Corp), which was diluted in blocking solution for 1h at 4 ºC. The embryos were first imaged by the RI-OCT method, and then imaged using SPIM.

### **3.2.4** Image process and registration

Image acquisition and processing procedures for RI-OCT have been detailed in Chapter 2. Briefly, RI-OCT acquires normal 3D OCT structural images at different angles by rotating the sample, which is mounted on a rotational stage. After rescaling the images to physical dimensions by correcting for refractive indices, the images were rotated and co-

registered based on the rotation and translation of the sample. For SPIM imaging, the datasets acquired from both sides were initially aligned and combined with the instrument software (ZEN, Carl Zeiss Microscopy GmbH, Germany). Manual image co-registration and volumetric rendering of OCT and SPIM images were conducted in Amira (FEI Co., OR, USA) after rescaling the images to physical dimensions. Both data sets were imported into Amira, rescaled to proper physical dimensions by setting pixel sizes, and translated/rotated to achieve proper alignment. The transformation was edited interactively in the 3D viewer using the Open Inventor draggers in Amira. The transformation parameters were adjusted until the general contours overlapped. Finer alignment was performed by simultaneous visualization of cross sections from two data sets. For 3D rendering of matched volumes, the OCT data was assigned to the grey color channel, and the SPIM data was assigned to the red channel. The intensity and opacity of each individual color channel were adjusted for better visualization.

### 3.3 Results

Figures 3-2 (a) and (b) show 3D rendering of the bead phantoms imaged using OCT and SPIM (at an excitation wavelength of 488nm), respectively. Two large beads can be easily identified, and their relative positions in the image is the same in the OCT and SPIM images. Small microbeads (indicated by the yellow arrows and yellow dished circles) are also located in the same relative positions in both images. Figure 3-2(c) is an OCT cross sectional image from a selected plane, and Figure 3-2(d) is same OCT cross sectional image overlapped with the corresponding SPIM image, which indicates that the data from the two imaging modalities can be well co-registered.

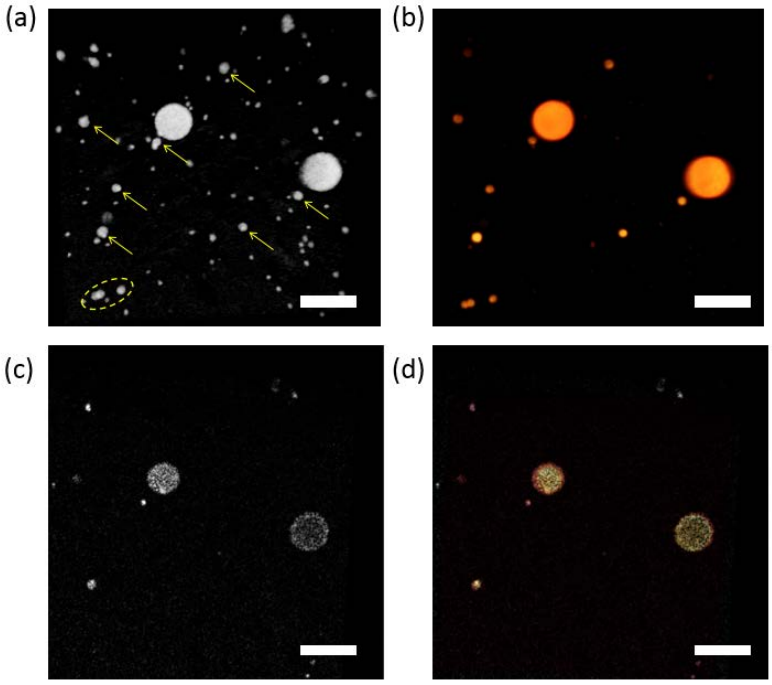


**Figure 3-2**: (a) 3D OCT and (b) SPIM imaging of beads phantom. (c) Cross-sectional OCT image of selected plane. (d) Combined OCT and SPIM images of the same cross-sectional plane. Scale bars are 500 μm.

Figures 3-3(a-d) depict volumetric renderings of the RI-OCT of mouse embryo obtained from different angles, and Figures 3-3(e-h) are combined RI-OCT images from different views. Figures 3-3(i) and (j) present the SPIM images of the embryos from opposite sides, and Figure 3-3(k) and (l) show the merged SPIM images.

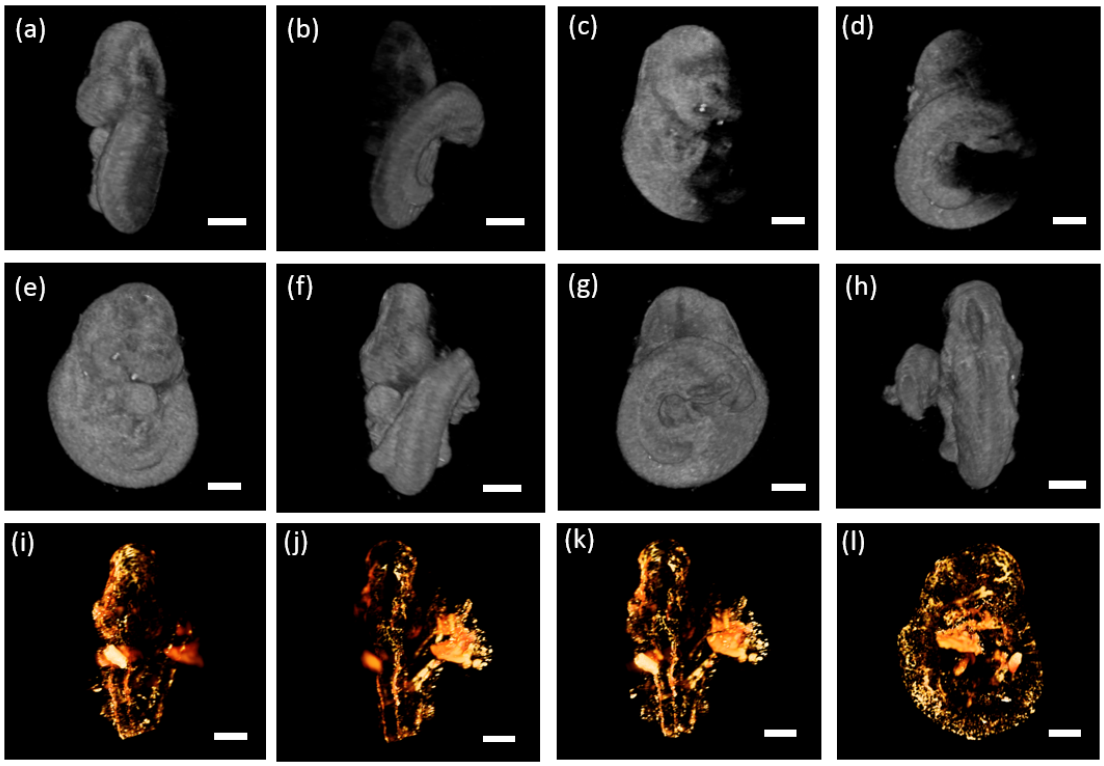


**Figure 3-3**: RI-OCT imaging of E9.5 mouse embryo at (a) 0 degree, (b) 180 degree, (c) 90 degree, (d) 270 degree, (e-h) composite from all four angles. SPIM imaging of same embryo from (i) one side, (j) opposite side, and (k-l) combined. Scale bars are 500 μm.

The co-registered OCT and SPIM images of an E9.5 mouse embryo are shown in Figure 3-4. Figure 3-4(a) presents a 3D RI-OCT rendering of the mouse embryo, Figure 3-4(b) and (c) shows the 3D SPIM images of same embryo excited at 488nm and 561nm, respectively. Figure 3-4(d) presents the co-registered 3D OCT and SPIM images. Figures 3-4(e-h) are co-registered images from selected 2D cross-sections. Endothelial cells labelled by PECAM1 show that the embryo vascular structure can be visualized in high detail with SPIM. The vasculature is widely distributed in the brain, spine, and tail of the embryo. Various embryonic structures could be identified, such as the dorsal aorta, neuro lumen, and intersomitic vessel. Combined with the ϵ-globin-GFP excited at 488 nm, it is possible to see how blood was distributed in different organs at the time of fixation. The

brain had more erythrocytes trapped in the microvascular network, and many erythrocytes were also found in the heart, limb, and dorsal aorta. The PECAM1 signal is much stronger in and around the heart due to the presence of the rapidly developing cardiovascular system at this embryonic stage. From SPIM cross sectional images, it is possible to visualize the internal and external structure of the heart. GFP and PECAM1 labelled cells show the myocardium and erythrocytes, while OCT can reveal the heart wall thickness as indicated by the arrowhead in Figure 3-4(e). However, the light was aberrated due to the embryo tissue, resulting in blurring that is visible in the images, particularly in the internal structures of the embryo. Clearing protocols can ameliorate this issue, but their toxicity is not suitable for live imaging [125]. Moreover, most SPIM publications focus on clear samples, such as zebrafish, which do not encounter such issues during imaging [126, 127].

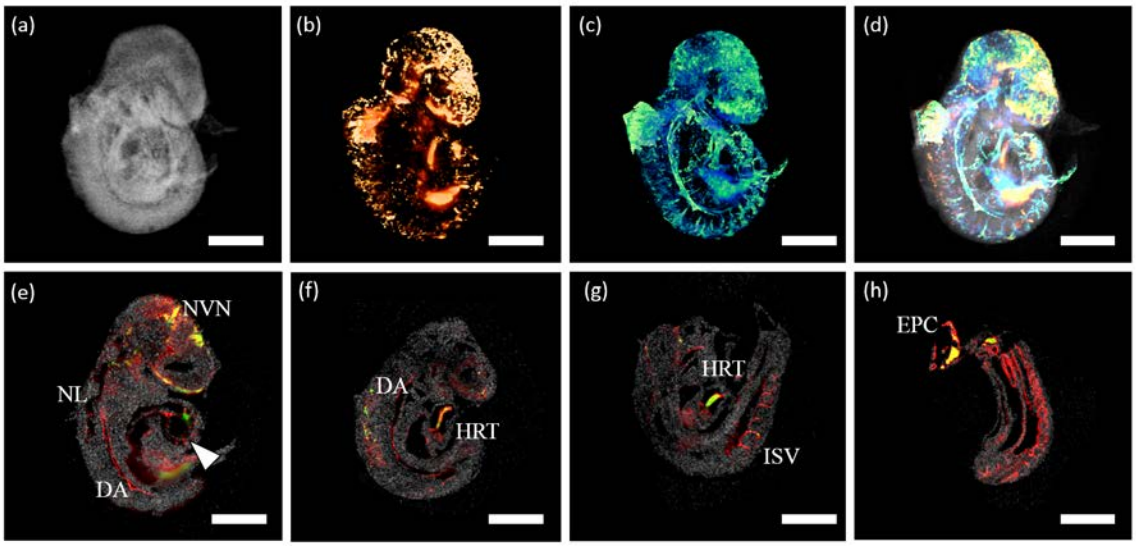


**Figure 3-4**: (a) OCT image, (b) SPIM image at excitation wavelength of 488nm for the ϵ-globin-GFP cells, (c) at excitation wavelength of 561nm for PECAM1 labeled endothelial cells, (d) 3D registered image, (e-h) 2D OCT image registered with SPIM image.

## 3.4 Discussion

In this chapter, we imaged both the structure and the vasculature of an E9.5 mouse embryo. Major vasculogenesis and angiogenesis occur in the mouse embryo between E8.0 and E10.0, during which time the vasculature develops from a simple circulatory loop into a complex and fine structured system. Therefore, E9.5 is a suitable stage to study vasculature development. As discussed previously, optical clearing is usually necessary for SPIM imaging for large and highly scattering tissues but is not suitable for *in vivo* applications. As shown in this study, tissue scattering is not completely prohibitive for SPIM imaging of E9.5 embryos, and RI-OCT enables whole-body imaging of E9.5 murine embryos. Thus, the combination of these techniques is suitable for embryos at this stage. However, imaging whole, unmodified embryos at later developmental stages is still a challenge for both SPIM and RI-OCT.

Although OCT is also able visualize blood vessels in biological tissue with various angiography techniques [128-130], it requires blood flow of a sufficient velocity to provide contrast between surrounding tissues. In this preliminary study, the embryo was fixed in agar, and thus was not suitable for angiographic imaging. The erythroblasts were labelled with GFP for fluorescence imaging by SPIM and OCT-based angiographic techniques may not be able to provide the spatial resolution of SPIM, with which each cell could be visualized and tracked. However, OCT-based angiography is label-free, and we have shown a technique capable of 3D video-rate volumetric speckle variance-based angiography *in vivo* in cultured mouse embryos. The high temporal resolution of OCT is well-suited for studying the dynamics in the embryo cardiovascular system, such as blood flow and heart function [131]. On the other hand, SPIM has the advantage of labelling

multiple cell types of interest, which is useful for studying the dynamics of cell migration and cell proliferation during embryo development [132-134]. In SPIM, the imaging depth limits spatial resolution when imaging thicker samples, as the signal gets weaker and scatters when imaging deep within the tissue. Multiple methods have been developed to overcome depth limits, including double-sided illumination, multiview acquisition, and clearing. However, multiview acquisition increasing acquisition and processing time. Another method to improve the penetration depth of SPIM imaging is to utilize two-photon excitation. Truong et al. have demonstrated that two-photon SPIM could achieve a penetration depth two times better than one-photon SPIM for imaging of fly embryos [135]. Clearing is not suitable for live imaging, can quench fluorescence signals, and only inorganic clearing solutions are compatible with the light sheet system. Also, there is a trade-off between high spatial resolution and field of view. In this study, we chose a large imaging field to capture the whole embryo at the cost of spatial resolution. A larger field of view could be accomplished at a higher resolution by performing mosaic imaging, but the trade-off would be an increase in the imaging and co-registration time. In contrast, the spatial resolution of OCT is defined in the axial direction by the bandwidth of the broadband source, and the transverse resolution and axial depth of field are defined by the NA of the objective or scan lens. However, multi-focus scanning techniques such as Gabor domain OCT or numerical re-focusing can overcome the limited depth of field from high NA applications. Another solution is the use of non-diffracting beams, such as Airy beams [136]. Nevertheless, for early stage embryos (e.g., E9.5), a depth of field of a few millimeters is sufficient for whole-body embryo imaging [20].

In addition to OCT, OPT is another powerful technique to study the embryo morphology. OPT and SPIM have been combined for complementary imaging of murine embryos and zebrafish [137, 138]. OPT was able to image entire later stage embryos (up to E13.5) but requires a lengthy clearing and fixation procedure, while OCT can perform live imaging. Although live OPT imaging of murine embryos has been demonstrated, only a limb bud was successfully imaged [139].

In this study, the mouse embryo was fixed in agar to avoid any movement while moving the sample between the two imaging systems. Embedding the sample in agar may be suitable for samples such as zebrafish, but it is not applicable for murine embryos due to their rapid growth and need for a controlled environment for *ex utero* culturing. The next step is to combine the systems into a single instrument with synchronized acquisition to eliminate the need for immobilizing the embryos and enable *in vivo* imaging. In the current work, a commercial SPIM system was utilized, which is not convenient for integrating OCT. This study has shown the feasibility of combining OCT and SPIM imaging of the same embryo for the first time and lays the foundation for the development of a dual-modality OCT/SPIM system. The same registration method could be directly applied to the dual modality system. The future work will focus on developing a customized SPIM system, similar to the Open-SPIM, which will combine SPIM and OCT into a single multimodal embryonic imaging system. The main advantage of a dual modality instrument is the elimination of transferring the sample, ensuring that the embryo is imaged in the same conditions. Moreover, a dual modality setup would enable easier live imaging by imaging the embryo in a culture medium, which could provide a more robust growth environment. In addition, various parameters can be analysed with SPIM imaging such as

cell proliferation, cell death, cell type identification, and cell signalling, while OCT would provide complementary structural information. It will be more beneficial for mouse embryonic developmental study.

## 3.5 Conclusion

In this chapter, we compared and combined images of *GFP*-expressing mouse embryos obtained by RI-OCT and SPIM. Fluorescent microbeads and an E9.5 mouse embryo were imaged with both imaging techniques, and the images were co-registered. The results show that the images from both methods can be registered well after rescaling to physical dimensions. RI-OCT provided high-resolution whole-body structural imaging of an E9.5 mouse embryo, and SPIM imaged the embryo vasculature with high resolution as well.

# Chapter 4 - Assessing age-related changes in the biomechanical properties of crystalline lens using a co-aligned ultrasound and OCE system

In this chapter, a confocal ultrasound and phase-sensitive OCE (US-OCE) system is utilized to investigate age-related changes in the biomechanical properties of the crystalline lens in rabbit eyes. An elastic deformation is induced onto the surface of the lens by localized acoustic radiation force (ARF), and is then measured by phase-sensitive OCT. The OCE results have demonstrated significant difference between young and old lenses, suggesting that the stiffness of the lens increases with the age. These results demonstrate the possibility of OCE for completely noninvasive analysis and quantification of lens biomechanical properties.

## 4.1 Introduction

The crystalline lens is a natural lens which contributes to one third of the eye's refractive power. It's extremely important for the eye to focus light. Presbyopia is the progressive loss of the eye's ability to accommodate which prevents farsighted individuals from reading or viewing nearby objects clearly [140-144]. The age-related change of biomechanical properties in the crystalline lens is intrinsically linked to the development of presbyopia. Many studies have demonstrated an age-related stiffness change of crystalline lenses for animals and humans [145-148]. However, the mechanism of how lens biomechanics affects the progression of presbyopia is not fully understood. The location of the crystalline lens makes it challenging to find suitable techniques to perform measurement of its mechanical properties without destruction of the eyeball. The ability to noninvasively measure mechanical properties of the lens *in vivo* is beneficial for direct objective evaluation of the outcomes of surgical techniques that aim to restore

accommodation via lens softening, including femtosecond lasers, pharmaceutical agents, and lens replacement with a flexible material [149-152].

USE and MRE have been employed in clinics as diagnostic tools during the past few years. In previous studies, the viscoelastic properties of porcine lenses have been examined by combining microbubbles created by laser-induced optical breakdown and ARF [153]. The laser induced microbubbles are displaced by an acoustic pulse and elastic properties are estimated by analyzing the time characteristics of microbubble motion. However, this method is required to produce microbubbles within the lens, which is an invasive procedure. Also, this approach may be limited for *in vivo* applications due to the relatively low sensitivity of ultrasound imaging. MRE also suffers from same problems of low spatial resolution when applied to ocular tissue measurements.

Various optical elastography methods have been proposed based on several optical imaging techniques, such as laser speckle imaging, multiphoton microscopy, digital holography, Brillouin microscopy, and OCT [8, 61, 154-158]. Among them, OCE has been successfully demonstrated in different applications such as cornea elasticity measurements, tumor detection, and intravascular plaque detection [100, 101, 159-161]. Although OCE has been extensively developed for different applications, including for the elastic properties of isolated ocular tissues, it is still very challenging to investigate crystalline lenses *in situ* due to their unique location.

In this chapter, a co-focused US-OCE system is developed to investigate the age-related changes in the biomechanical properties of rabbit crystalline lenses *in situ*. This system combines a pulsed ultrasound system capable of producing an ARF on the lens surface and a phase-sensitive OCT system for measuring the induced lens displacement. Pilot

experiments were performed on the lens *in situ* in both young and mature rabbits. Both the maximum displacements (MD) and the undamped natural frequency of the displacement profile were analyzed for comparison study. For validation, uniaxial mechanical compression tests were conducted on the same young and mature rabbit lenses.

## 4.2 Methods and Materials

### **4.2.1** Experimental Setup

To assess the biomechanical properties of the rabbit lens, a co-focused US-OCE was developed by combining ultrasound excitation with SD-OCT, as schematically shown in Figure 4-1(a). A single element ultrasound transducer with a diameter of ~12.7 mm and a focal length of ~19 mm operating at 3.7 MHz central frequency was employed in the system. A sinusoidal wave with a frequency of 3.7 MHz generated by a function generator was gated by a 1.1ms pulse to produce a one-time burst. The driving signal for the ultrasound transducer was amplified using a 40 dB power amplifier. The ARF from the ultrasound wave was used to remotely perturb the anterior surface of the crystalline lens through the cornea and the aqueous humor of the eye.

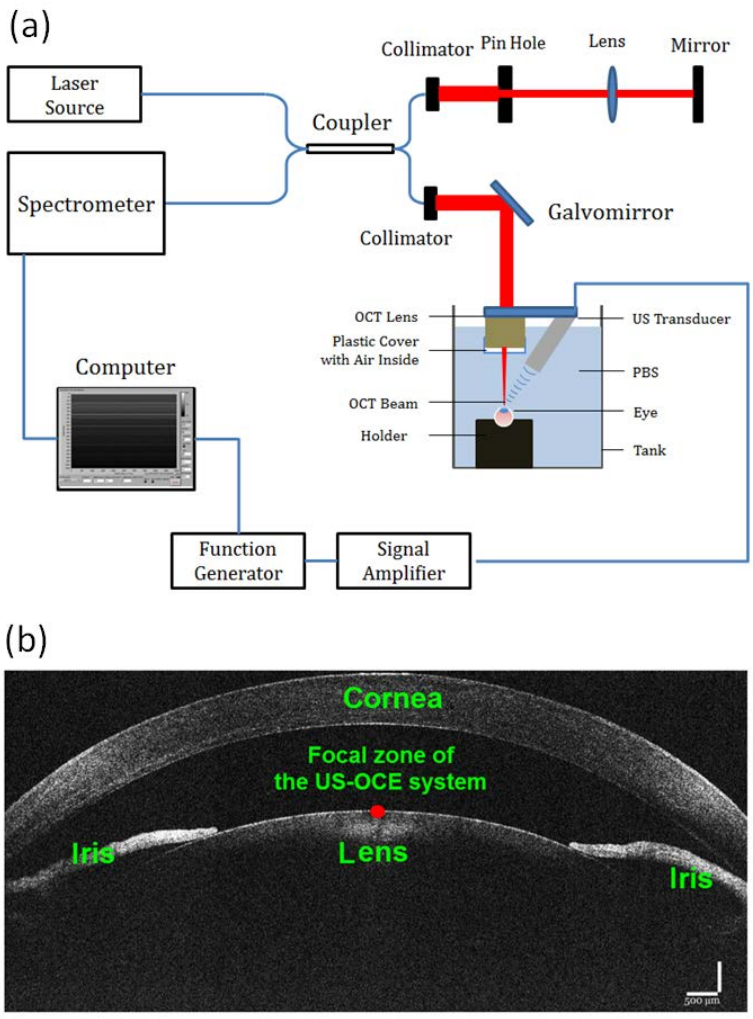


**Figure 4-1**: (a) Schematic of the co-aligned US-OCE system; (b) Typical OCT image of the rabbit lens.

The SD-OCT system utilizes a superluminescent laser diode with a central wavelength of ~840 nm and a bandwidth of ~49 nm was utilized as the light source. The laser beam was splitted and directed to the reference and the sample arms of a Michelson interferometer. The interference of the combined light from these two arms was detected using a high-resolution spectrometer comprised of a grating and a line-scanning CCD camera. The A-line acquisition rate of this system was set to be 25 kHz during the experiments. The FWHM of the transverse Gaussian profile of the OCT beam at the

imaging focal plane was ~8 μm. The system's phase stability measured by recording the interference from the reflection of the two surfaces of a glass slide placed in the sample arm was ~4 milliradians.

A custom-built transducer holder was used to securely attach the ultrasound transducer to the OCT objective lens. Co-alignment of the focal zone of the ultrasound beam and the OCT imaging beam was achieved by aligning the mounted ultrasound transducer with a needle tip. ARF excitation and OCT M-mode imaging (rapidly repeated A-scans at the same location) were synchronized by a computer-generated triggering signal.

The surface of the crystalline lens was placed at the co-aligned focal zone of the US-OCE system. Stimulation with the ARF produced a perturbation on the lens surface, resulting in a displacement of the lens surface. The displacement of the apex of the crystalline lens as shown in Figure 4-1(b) was measured by the phase-sensitive OCT system. Since the ultrasound pulses were delivered through one part of the cornea, outside of the optical path of the OCT beam, the displacement of the cornea did not contribute significantly to the measured signal from the lens surface.

### **4.2.2** Sample preparation

Eyes from young (2-3 months old) and mature (over 6 months old) rabbits were used in this study. During the experiments, the entire eye globes were kept in the saline solution at room temperature to minimize any change in the tissue properties. The lenses were carefully checked to verify that they are optically clear during experiments. The sample was positioned in a custom-designed eye holder to prevent motion during the experiment. For the US-OCE experiments, 3 young and 4 mature rabbit eyes were used.

### **4.2.3** Kinematic model of the relaxation process

The vertical movement of the tissue in the focal zone of the US-OCE, shown as a red dot in Figure 4-1(b), can be separated into forced motion in response to the acoustic radiation push, and relaxation motion that occurs after the ARF is removed and when the external forces are zero.

The following simplified kinematical differential equation can be used to describe the lens's relaxation process starting from the MD point:

$$m\frac{d^2y(t)}{dt^2} + c\frac{dy(t)}{dt} + ky(t) = 0, \tag{4.1}$$

where $m$ is the equivalent mass, $c$ is the viscosity coefficient and $k$ is the equivalent spring stiffness. To understand the basic characteristics of the equation, two parameters, $\xi$ and $\omega$, are introduced where $\xi = c/(2\sqrt{mk})$ is the damping ratio and $\omega = \sqrt{k/m}$ is the undamped natural frequency of the dynamic system. Equation (4.1) then becomes

$$\frac{d^2y(t)}{dt^2} + 2\xi\omega\frac{dy(t)}{dt} + \omega^2 y(t) = 0. \tag{4.2}$$

The analytical solution of equation (4.2) is related to the value of $\xi$ as:

(a) $y(t) = \mathrm{A}(1+\mathrm{b}t)\mathrm{e}^{-\omega t}$ when $\xi = 1$; (4.3)

(b) $y(t) = \mathrm{e}^{-\xi\omega t}(\mathrm{A}\cos\omega_D t + \mathrm{B}\sin\omega_D t)$ with $\omega_D = \omega\sqrt{1-\xi^2}$ when $0 < \xi < 1$; and

(c) $y(t) = \mathrm{e}^{-\xi\omega t}(\mathrm{A}\mathrm{e}^{-\omega_D t} + \mathrm{B}\mathrm{e}^{\omega_D t})$ with $\omega_D = \omega\sqrt{\xi^2-1}$ when $\xi > 1$.

Here *A*, *b*, and *B* are the parameters to be determined. According to the exponent forms of the solution of equation (4.2), ω can also be described as the relaxation rate, which corresponds to the rate of the exponential-type displacement recovery process.

### **4.2.4** Model for a viscoelastic layer

To quantitatively evaluate age-related changes in the viscoelastic properties of the rabbit lenses, we considered a model-based reconstructive approach based on the OCE-measured vertical displacement of a homogeneous viscoelastic layer in response to an ARF of short duration [162]. In this approach, tissue is modeled as an incompressible viscoelastic (Voigt body) layer. An acoustic impulse is considered to be an axisymmetric force applied to the upper surface of the medium in the direction of the z-axis of the cylindrical system of coordinates (r,θ,z). The mechanical parameters: Young's modulus (E), shear viscosity modulus (η), and density (ρ) are constant in the layer. An analytical solution of the spectral component of the vertical displacement in the frequency domain can be derived:

$$Y_z(r,z) = -\int_0^\infty \alpha^2 J_0(\alpha r)[A_1 e^{-\alpha z} - A_2 e^{\alpha z} + \alpha(B_1 e^{-\vartheta z} + B_2 e^{\vartheta z})]d\alpha, \tag{4.4}$$

$$\vartheta = \sqrt{\alpha^2 - k^2},\ k^2 = \rho\varpi^2/(E/3 + i\varpi\eta),$$

where $J_0$ and $J_1$ are Bessel functions of order 0 and 1, respectively, and $\varpi$ is the angular frequency. Four unknown constants $A_1$, $A_2$, $B_1$, and $B_2$ are defined using four boundary conditions at the layer boundaries. We consider fixed boundary conditions for the displacements on the bottom of the layer; no shear force on the top surface, and a normal force at the focal point of the transducer. The solution in the time domain was calculated using the inverse Fourier transform after taking into account the duration of the acoustic pulse.

Using the analytical solution of the forward problem (4.4), reconstruction of Young's modulus and shear viscosity was posed as a minimization problem, i.e. by minimizing the

error function defined as the difference between the OCE-measured vertical displacement $y^{exp}$ and theoretically calculated displacements $y^{theory}$ at the point (r=0, z=0):

$$\delta = \left\| y^{exp} - y^{theory}(E,\eta) \right\| . \quad (4.5)$$

The density of the lens was assumed to be around 1100 kg/m$^3$ [163, 164]. To minimize (4.5), a gradient-based iterative procedure was implemented. In the minimization procedure, normalized displacement profiles were used so that only the temporal characteristics of the vertical displacements were taken into account, not the amplitudes. This approach avoided the influence of the ultrasound beam attenuation and differences in acoustic impedance of the materials such as lens and aqueous humor.

### **4.2.5** Uniaxial mechanical compression tests

After the measurements by the US-OCE system, the eye globes were carefully dissected to extract crystalline lenses for testing with a uniaxial mechanical compression testing system (Model 5943, Instron Corp., MA). The lens was centrally positioned between the compression plates of the device. Prior to the mechanical testing on each lens, a 0.004N pre-loading force was applied. The compression speed was set to 2 mm/minute. The testing was stopped when the vertical displacement reached 30% the whole thickness.

## 4.3 Results

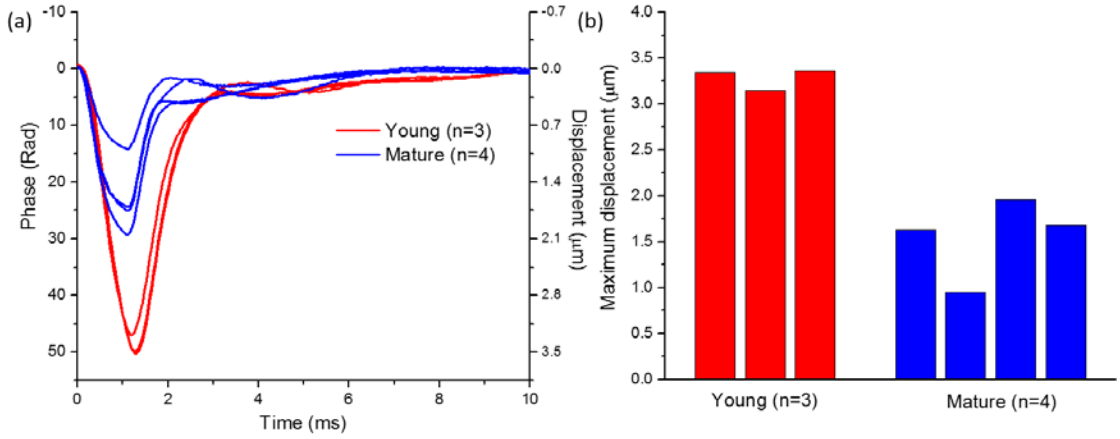


**Figure 4-2**: (a) Temporal vertical displacement profiles of young (n=3) and mature lenses (n=4) measured by the OCE; (b) MDs of the young (n=3) and mature (n=4) lenses.

The first parameter used to assess the age-related changes in biomechanical properties of the rabbit lens was the amplitude of the vertical displacements as measured by US-OCE. Figure 4-2(a) shows the temporal vertical displacement profiles of typical young and mature lenses. It is clear from either profile that the surface of the crystalline lens starts to deform upon application of the acoustic radiation force. After the removal of the acoustic radiation force, the surface of the lens begins to recover to its original position. Here, the vertical displacement is on the scale of micrometers, which helps ensure that the structural and functional properties of the crystalline lens are not affected. The data presented in Figure 4-2(b) clearly demonstrate a significant difference between the maximum vertical displacements of the young and the mature lenses, which are 3.3±0.1 µm and 1.6±0.4 µm, respectively. It can be clearly seen that under the same experimental conditions, the maximum vertical displacement of the young lenses is greater than that of the mature lenses, which indicates a higher stiffness of mature lenses than the young lenses.

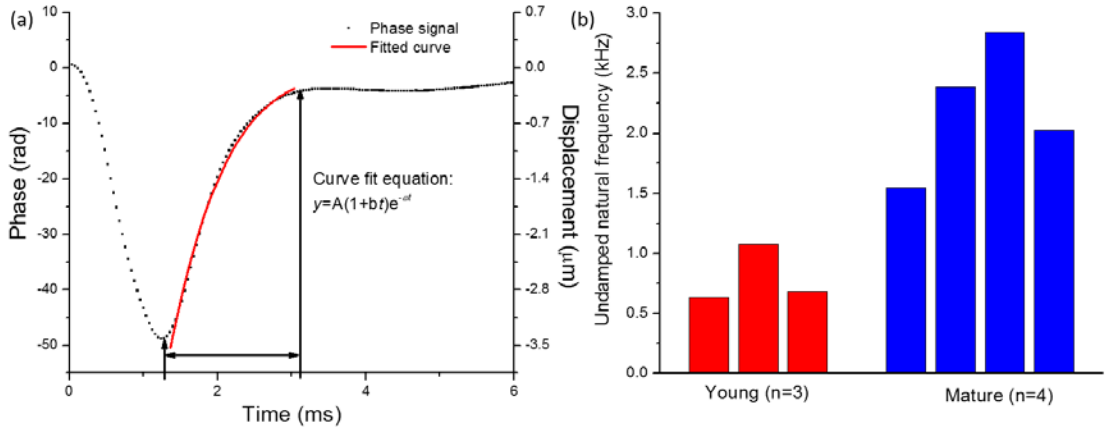


**Figure 4-3**: (a) Recovery process fitted by $y(t) = \mathrm{A}(1+\mathrm{b}t)\mathrm{e}^{-\omega t}$ in the OCE-measured vertical displacement; (b) The undamped natural frequencies $\omega$ for the young (n=3) and mature (n=4) lenses.

The undamped natural frequencies $\omega = \sqrt{k/m}$ of the lenses are shown in Figure 4-3. The recovery process in each of the phase profiles, which is defined as the range between the maximal displacement point and the starting point of equilibrium, was fitted with our model, as shown in Figure 4-3(a). During the curve fitting process, it was found that the damping ratio, $\xi$, was greater than 0.99. The damping ratio was therefore, approximated to be equal to 1 for all the lenses. Therefore, equation (4.3) was used to analyze the relaxation process. Figure 4-3(b) shows a comparison of, the undamped natural frequency, $\omega$, for the two age groups. The undamped natural frequency values of the young and the mature lenses are 0.8±0.2 kHz and 2.2±0.5 kHz, respectively. In addition to the maximum vertical displacements, the undamped natural frequencies indicate that the stiffness of the mature lenses is greater than that of the young lenses.

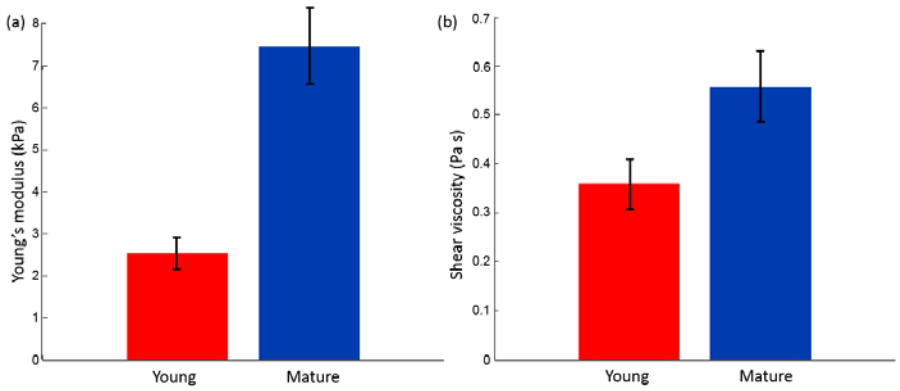


**Figure 4-4**: (a) Young's modulus and (b) shear viscosity modulus of young (n=3) and mature (n=4) lenses estimated based on the model of the viscoelastic layer.

The result of the reconstruction of Young's modulus and shear viscosity for young and mature lenses is shown in Figure 4-4. While there was a significant increase in the Young's modulus with age, the increase of shear viscosity was less pronounced. These results are in agreement with our previous results for bovine lenses, where age-related changes in elastic properties were more pronounced than changes in viscous properties.

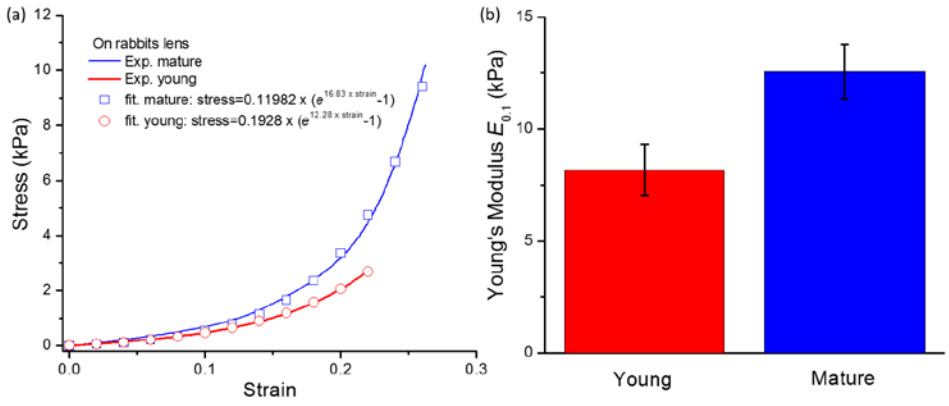


**Figure 4-5**: (a) Uniaxial mechanical tests and fitted stress-strain curves for typical young and mature rabbit lenses; (b) The distribution of the Young's modulus $E_{0.1}$ at strain $\varepsilon$=0.1 for the measured young and mature rabbit lenses.

The stress-strain curves and the Young's moduli of the young and the mature lenses are compared in Figure 4-5. Figure 4-5(a) shows typical examples of the stress-strain

curves measured on the young and mature rabbit lenses by uniaxial mechanical compression testing. The stress-strain curves for the young and mature lenses can be fitted as $stress = 0.1928(e^{12.28\times strain} - 1)$ and $stress = 0.11892(e^{16.83\times strain} - 1)$, respectively, where stress is in units of 'kPa'. At a strain of 0.1, Young's moduli of the young and mature lenses are 8.2±1.1 kPa and 12.6±1.2 kPa, respectively, as shown in Figure 4-5(b). This result clearly shows that the mature lenses are stiffer than the young lenses, confirming the US-OCE results.

## 4.4 Discussion

In this study, the biomechanical properties of young and mature rabbit crystalline lens were assessed noninvasively using an US-OCE system. The US-OCE system could detect the differences in elastic properties of young and mature rabbit lenses. The analysis of the MDs and undamped natural frequencies as well as the model-based reconstruction of the lens mechanical properties showed that the stiffness of the lens increases with age. Results from the model-based reconstruction indicated approximately a three-fold increase of Young's modulus in the mature lenses in comparison with the young lenses. This study demonstrates the effectiveness and feasibility of the noninvasive US-OCE method in assessing the biomechanical properties of the lens.

The axis of the OCT beam and, therefore, the direction of the measured displacements were orthogonal to the lens surface. However, the ultrasound transducer was placed at an angle of ~45$^{o}$ relative to the OCT sample beam, so that the ARF includes both an axial and a transverse component. In our experiment, only the axial displacement at the apical position of the lens surface was measured by the US-OCE system. In general, the measured axial displacements are related to the stiffness gradient inside the lens, including the cortex

and nucleus. Our measurements reflect the elastic properties of the whole lens where higher elasticity leads to smaller displacement.

During the experiment, the distance between the sample and the ultrasound transducer was held constant. Therefore, the ARF applied on the lens surface can be considered approximately the same for all the samples, which eliminates the influence of the magnitude of the ARF on the measured lens surface displacement-amplitude.

The undamped natural frequency was extracted from the relaxation process of the lens surface after the excitation by ARF was removed. The undamped natural frequency is associated with the elasticity of the sample. The results show that the young lenses had a lower undamped natural frequency than the mature lenses. The analysis of the undamped natural frequency, like the analysis of the maximum surface displacements, therefore shows that the mature lenses are stiffer than the young lenses. The relaxation process is mainly associated with the viscoelastic properties of the lens. Small oscillations during the recovery process were observed in both the young and mature lenses, as a result of dynamic processes in the lens after the rapidly applied force. Modeling these processes could result in more accurate quantification of lens biomechanical properties.

In this study, the undamped natural frequency for the mature rabbit lens was around 2-3 kHz, while for the young rabbit lens it was around 0.6-1 kHz. In previous work, it was determined that the undamped natural frequency of the human cornea is around 3 kHz, which is of the same order as the undamped natural frequencies of the mature lens measured in the present study [165]. More studies are underway to understand the influence of the lens gradient, viscoelasticity, and age on the relaxation rate and the amplitude of the displacement profile. It should be noted that there is a high variability in the mature samples

for both the elasticity measurements by US-OCE and uniaxial mechanical compression testing. This high variability implies that the effect of age on the lens elasticity varies between individuals.

Quantitative measurements of the mechanical properties of the crystalline lens based on US-OCE system require the development of an appropriate mechanical model and reconstructive procedure. Here we have presented a reconstruction approach based on the simplified model of an isotropic homogeneous viscoelastic layer, although in reality the lens has different density distributions and the central nucleus region is harder than the cortex region. In this work, we did not study the gradient density distribution within the lens, and we treated the whole lens as a homogenous object for simplification. This simplification could be one important reason for differences between the uniaxial compression and US-OCE-derived values. Results of the reconstruction demonstrated approximately a three-fold increase of Young's modulus and 50% increase in shear viscosity in the mature lenses in comparison with the young lenses. This trend agrees with previous findings [145], in which a bubble-based ARF was applied to measure the elasticity change in porcine and bovine lenses of different ages. Furthermore, our quantification of Young's moduli of the rabbit lens using OCE falls in the elasticity range reported for crystalline lens [166, 167]. The US-OCE method presented in this study, which combines ARF excitation and phase-sensitive OCT measurement has the advantage of noninvasive detection. Only a minimal ARF is required to induce a detectable deformation due to the high displacement sensitivity of phase-resolved OCT detection. This small acoustic radiation helps to preserve the structural and functional properties of the ocular tissues. Ziebarth et al. investigated the elasticity of the monkey lens by atomic force microscopy

[168]. They produced a small indentation around 0.5 to 1 micron on the whole *in vitro* lens and obtained an average Young's modulus of 1.7 kPa, which was close to the 2.5 kPa obtained by OCE and the viscoelastic layer model. The slight disagreement may be due to the source of the lenses, animal species, and method of indentation.

The reconstructed Young's modulus values are lower than we expected based on the results of uniaxial mechanical compression tests. The underestimation in the elastic modulus could be a result of several limitations in the current model. The OCE results were determined and influenced by the combined effect of the cortex and nucleus inside the lens. The extent of influence of the nucleus on the results may be different between OCE and uniaxial compression measurement. Even though the crystalline lens is an inhomogeneous object, we have modeled the lens as a homogeneous layer. Therefore, the reconstruction results may correspond to the cortex of the lens, which is softer than the nucleus. In addition, the effect of the aqueous humor on the displacement of the lens surface was not taken into account. A free boundary condition was assumed for the lens surface. The presence of the aqueous may result in a loss of acoustic energy and underestimation of Young's modulus. Several other factors, such as motion of the lens as a whole, influence of the lens capsule, and spatial distribution of acoustic pressure at the focal zone were not considered in the model, but may be critical for elasticity reconstruction. The impact of these factors on the estimation of lens elasticity can evaluated by further development of a more sophisticated model of the lens and surrounding tissue that takes into account these effects, together with the use of inverse solution methods.

## 4.5 Conclusion

In summary, the US-OCE system, which combines ARF excitation and phase-sensitive OCT, was demonstrated as a promising tool for noninvasive assessment of the age-related changes in the biomechanical properties of the crystalline lens *in situ*. The maximal displacements, undamped natural frequencies, model-based reconstruction, and uniaxial mechanical compression tests all clearly indicate that the stiffness of the rabbit crystalline lens increases with age. The high displacement sensitivity of phase-resolved OCT detection enables the measurement of sub-micron displacements on the lens surface, which is critical for future *in vivo* study as it allows for the application of a minimal ARF to induce a detectable displacement and minimizes the potential ultrasound damage to the eye [169]. In addition, the high spatial resolution of OCT allows highly-localized investigation of the mechanical properties of the lens. These features may result in future translation of this technique in clinical applications.

# Chapter 5 - Assessing biomechanical properties of crystalline lens as a function of intraocular pressure with US-OCE

In Chapter 4, we investigated the age-related changes in the biomechanical properties of crystalline lenses using the proposed confocal US-OCE system [3]. Besides aging, many other factors can influence the biomechanical property measurements of the crystalline lens. In this Chapter, the link between intraocular pressure (IOP) and lenticular elasticity is further investigated. The OCE results demonstrated that the stiffness of the crystalline lens increased as IOP increased. However, compared to cornea and sclera, the effect of stiffening with IOP for lens was significantly less pronounced. Same OCE measurements were then repeated for decreasing IOPs, and we discovered that the changes in stiffness could be reversed and a small amount of hysteresis was observed while the IOP was cycled back.

## 5.1 Introduction

Many ocular diseases can affect the normal optical function of the eye. For example, glaucoma or uveitis can cause ocular hypertension, which is an elevation of the IOP [170, 171]. A normal IOP is necessary to maintain eye-globe geometry and healthy function of ocular tissues. Previous studies have mainly focused on the influence of IOP changes on the cornea and sclera [13, 172-175]. The influence of IOP on the biomechanical properties of the crystalline lens has rarely been investigated, and their relationship has yet to be established.

Various techniques have been proposed to measure the viscoelasticity of the crystalline lens [176-178]. Most of these works are based on compressive mechanical testing, and the

crystalline lens needs to be dissected out of the eye-globe to perform such measurements. This does not truly replicate the environment within the eye-globe. Since the aim of this study is to investigate the influence of IOP changes on the biomechanical properties of the crystalline lens, these techniques are not suitable for such a study. Due to the location of the lens inside the eye-globe, ARF is the obvious noninvasive excitation method that can be combined with OCE to study the biomechanical properties of the lens. In Chapter 4, we proposed a co-focused US-OCE technique to study the age-related biomechanical properties of the lens, and this technique is well-suited to perform the proposed IOP influence study.

In this chapter, the changes in the biomechanical properties of porcine lenses as a function of IOP is investigated using this US-OCE system. The IOP was cycled from 5 to 30 mmHg with 5 mmHg steps, and the OCE measurements were performed at each step. The ARF remotely induced small amplitude (< 10 μm) localized displacements at the apex of the porcine lenses. The maximum displacement and relaxation rate (RR) of induced deformation at the lenticular apex were quantified to evaluate the change in stiffness of the lens as IOP was cycled. The model-based reconstructive approach was further modified to quantify the Young's moduli of the lens. For all three considered parameters, the results demonstrated that the stiffness of the crystalline lens increases along with IOP.

## 5.2 Methods and Materials

### 5.2.1 Experimental setup

The hardware setup of US-OCE has been introduced in Chapter 4 in details. A homemade closed-loop IOP control system was used to set the pressure inside the eye-globe. The IOP control system was composed of a pressure transducer and micro-infusion

syringe pump. The eye-globe was place in a custom holder, and two needles were used to cannulate the eye-globe through the holes in the holder. One needle was connected via tubing to a saline-filled syringe placed in the micro-infusion pump. The other needle was connected via tubing to the pressure transducer. A Matlab GUI program was developed to control the closed-loop IOP system. The IOP was changed by infusion or extraction of saline from the syringe.

### **5.2.2** Phantoms and Tissue Samples

Initial measurements were performed on tissue-mimicking agar phantoms of various concentrations (1%, 1.5%, and 2%). The phantom fabrication process has been covered in our previous work. Uniaxial mechanical testing was performed on the agar phantoms for validation purposes. Porcine eyes (n=8) were obtained fresh and shipped overnight on ice. The experiments were conducted when the samples were received, which was within 24 hours of enucleation. To measure the dependence of lenticular mechanical properties on IOP, the IOP was increased from 5 to 30 mmHg in 5 mmHg steps, and then decreased back to 5 mmHg using the same steps to investigate biomechanical hysteresis. Before the OCE measurements were taken, each eye was preconditioned by cycling the IOP between 5 and 30 mmHg twice. The parameters of acoustic excitation were the same for all IOPs, and 40 measurements were taken at each IOP level. M-mode imaging was performed with the ARF and OCT probe beams co-focused at the apex of the lens [3].

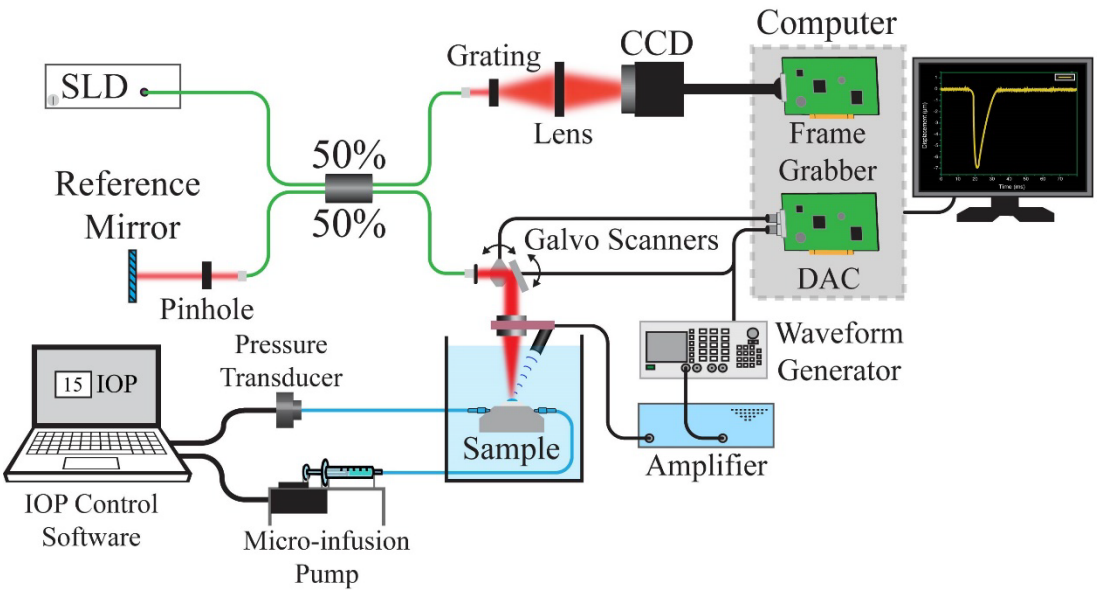


**Figure 5-1**: Schematic of experimental setup.

### 5.2.3 Mechanical characterization

The temporal phase profiles were unwrapped and then converted to the displacement profiles as

$$d(t) = \frac{\lambda_0}{4\pi n}\varphi(t)\,. \tag{5.1}$$

To estimate the relaxation rate of the deformation, the recovery process of displacement was fitted by an exponential function:

$$d(t) = Ae^{-bt}\,, \tag{5.2}$$

where $A$ was the maximum displacement, and $b$ was the relaxation rate as determined by fitting with the Matlab curve fitting toolbox. Figure 5-2(a) shows a typical displacement temporal profile and the fitting process for the relaxation range. In our previous studies we have shown that both these parameters can be used as a measure of the sample stiffness, such that the MD is inversely and the relaxation rate directly proportional to the stiffness.

### **5.2.4** Model-based estimation of Young's modulus

To quantitatively evaluate Young's modulus of the porcine lenses, we considered a model based reconstructive approach similar with the approach described in Chapter 4, where we investigated age-dependent changes in the biomechanical properties of the rabbit lenses. In this work, additional liquid-tissue interaction has been added to the model for describing the presence of the aqueous humor between the cornea and the lens. The lens is modeled as a viscoelastic (Voigt body) half-space, while liquid-solid interaction boundary conditions are assumed on the surface of the half-space. The solution of this problem is obtained in the frequency domain, assuming harmonically applied force with angular frequency $\omega$, such that the inverse Fourier transform should be used to find displacement profiles in the time domain. An acoustic impulse is considered as an axisymmetric force applied to the surface of the medium $z = 0$ in the direction of the z-axis of the cylindrical system of coordinates ($r$, $\theta$, $z$). The problem is axisymmetric, therefore no dependences on the angle $\theta$ are considered, and the $\theta$-component of the displacement vector is zero.

Spectrum component of the vertical displacement $u_z$ in a half-space $z \geq 0$ can be obtained using Hankel transform, as:

$$u_z = -\int_0^\infty \alpha J_0(\alpha r)(\nu_1 B_1 e^{-\nu_1 z} + \alpha^2 B_2 e^{-\nu_2 z}) d\alpha, \tag{5.3}$$

$$\nu_1 = \sqrt{\alpha^2 - k_1^2},\ k_1^2 = \frac{\omega^2}{c^2}, \nu_2 = \sqrt{\alpha^2 - k_2^2},\ k_2^2 = \rho\omega^2/(\mu_1 + i\omega\mu_2).$$

Here, $J_0$ is $0^{th}$ order of the Bessel function; $\mu_1$ and $\mu_2$ are shear elastic and viscous moduli; $c$ is the speed of sound; and $\rho$ is the density of medium. Two unknown constants $B_1$, and $B_2$ are defined using the solid-liquid boundary conditions at the half-space surface $z = 0$. On the boundary we require the continuity of the vertical displacements in solid and in

liquid, as well as zero shear stress. Also, we assume a Gaussian distribution of acoustic pressure *p(r)* with a width *R* on the half-space surface:

$$p(r) = P_0 e^{-r^2/R^2}, \tag{5.4}$$

where $P_0$ is the pressure amplitude. The ultrasound field in the focal point of the transducer was measured using a needle hydrophone with a sensor diameter of 0.2 mm (Precision Acoustics Ltd, Dorchester, UK). The normalized distribution of the time-averaged pressure in the focal zone of the 3.5 MHz transducer was fitted by the Gaussian profile (Equation 5.4). The best obtained value of $R$ = 0.37 mm was corrected to take into account the angle of 45 degree between the transducer and the lens surface in the experiment. We used "effective" value of *R*, such that the area of excitation was equal to the elliptical area of the ultrasound field in the experiment, such that $R = 0.37\sqrt[4]{2} \approx 0.44$ mm.

The inverse Fourier transform was applied to equation 5.3 to obtain displacement profile in the time domain and to evaluate the values of Young's modulus *E* of the lens for different IOPs. Estimation of Young's modulus was posed as a minimization problem, that is by minimizing the error function defined as the difference between the measured vertical displacement and theoretically calculated displacement (Equation 5.3) at the focal point of the ultrasound transducer *z=0, r=0*. Because it is difficult to evaluate the magnitude of the acoustic radiation pressure $P_0$ on the lens surface, normalized experimental displacement profiles were used, such that the amplitude of the displacement was not taken into consideration during minimization procedure. As a result, obtained values of Young's modulus were independent on MD values. We assume incompressibility of the lens tissue, such that $k_1^2 = 0$ and $E = 3\mu_1$. For all IOPs we assume a constant shear viscosity $\mu_2$ = 1 Pa·s based on the results of previous studies on porcine lenses [145], while no viscosity

was assumed for agar phantoms. Also, we consider the speed of sound in liquid as 1500 m/s, the lens density as 1185 kg/m$^3$, and density of liquid and agar phantoms as 1000 kg/m$^3$ [179].

## 5.3 Results

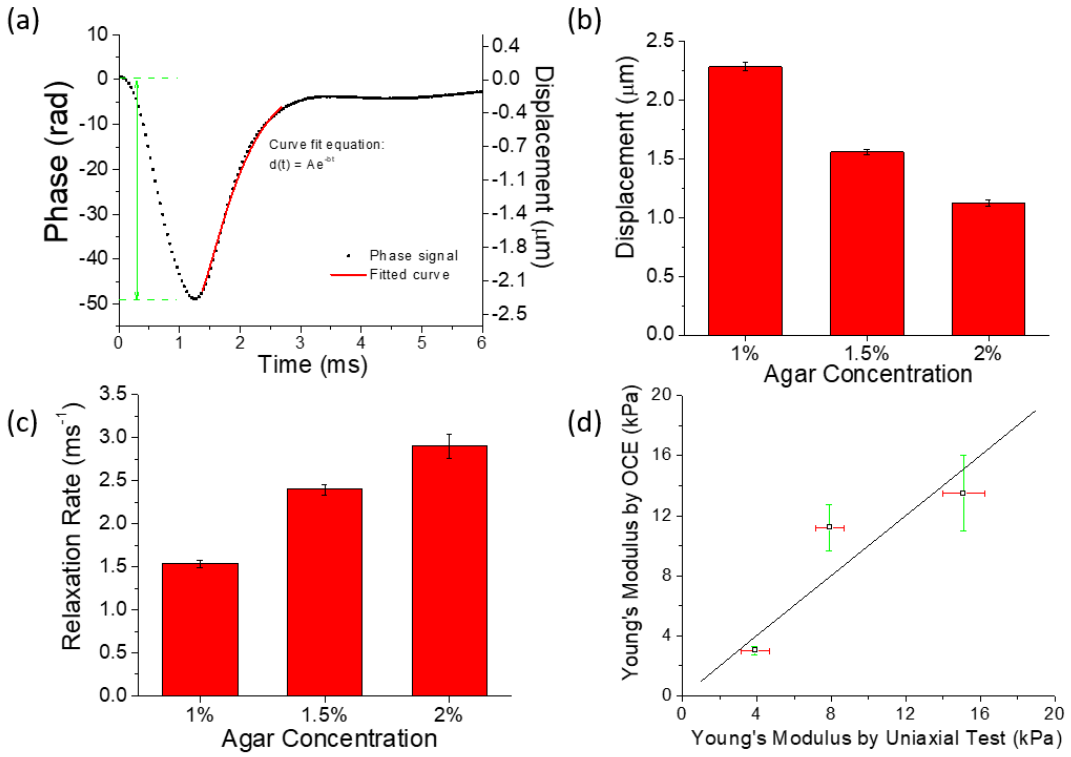


**Figure 5-2**: (a) The displacement at lens apex, (b) maximum displacement and (c) relaxation rate for agar phantoms at various concentrations, (d) comparison of the Young's moduli from mechanical compression testing and model-based reconstruction.

Figure 5-2(a) shows a typical temporal displacement profile. The MD from the initial steady-state is indicated in green, and the fitted exponential curve to quantify the RR is plotted in red. Figures 5-2(b-c) show the results of MD and RR for the agar phantoms at various concentrations. The MDs were 2.28±0.04 μm, 1.56±0.02 μm, and 1.12±0.03 μm in the 1%, 1.5%, and 2% phantoms. For the 1%, 1.5% and 2% agar phantoms, the RRs were 1.53±0.04 ms$^{-1}$, 2.40±0.06 ms$^{-1}$ and 2.90±0.14 ms$^{-1}$, respectively. As expected, while

the MD decreased as the agar phantom concentration and stiffness increased, the RR increased as the concentration and stiffness of the agar phantoms increased. Figure 5-2(d) presents the Young's modulus of phantoms calculated from the model-based elastic reconstruction method as compared to the Young's modulus measured by uniaxial mechanical compression testing. For the 1%, 1.5% and 2% agar phantoms, the results of the uniaxial mechanical test were 3.9±0.76 kPa, 7.9±0.77 kPa, and 15.1±1.1 kPa, respectively, while the results of the model-based estimation based on OCE measurements were 3.0±0.27 kPa, 11.2±1.54, and 13.5±2.51 kPa, respectively.

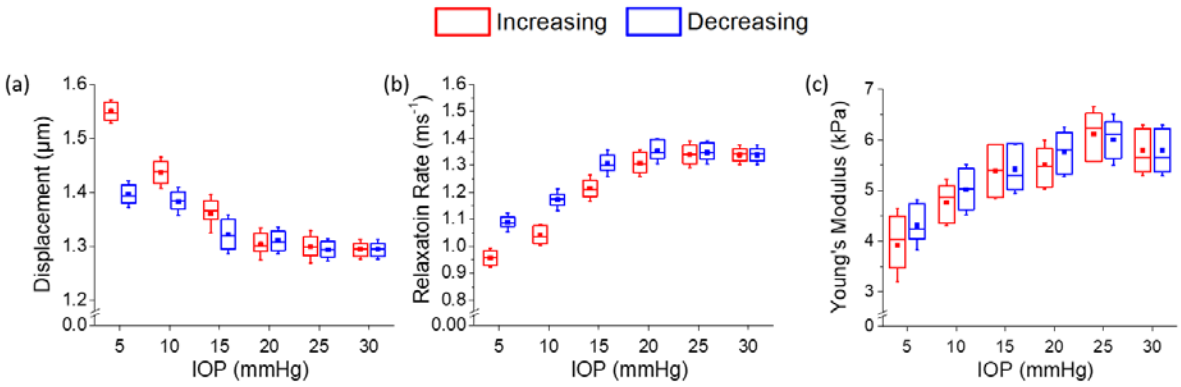


**Figure 5-3**: (a) The maximum displacement and (b) relaxation rate of the ARF-induced displacement at the apex of one typical porcine lens while IOP was cycled, (c) Young's modus of the lens as a function of IOP.

Figure 5-3 plot the results of MDs, RRs and Young's moduli of the porcine lenses from one representative sample while cycling IOP. The MD at 5 mmHg IOP (1.55±0.02 µm) decreased to 1.30±0.03 µm at 20 mmHg, and then gradually to 1.29±0.02 µm at 30 mmHg. The RR at 5 mmHg IOP (0.95±0.03 $ms^{-1}$) rapidly increased as the IOP increased up to 20 mmHg (1.31±0.05 $ms^{-1}$), and then stabilized to 1.34±0.03 $ms^{-1}$ at 30 mmHg. The model-based estimated Young's modulus increased from 3.92±0.52 kPa at 5 mmHg, to 5.51±0.48 kPa at 20 mmHg, and 5.79±0.50 kPa at 30 mmHg. It is worth noting that hysteresis effect is observed for all the three parameters when IOP was cycled back.

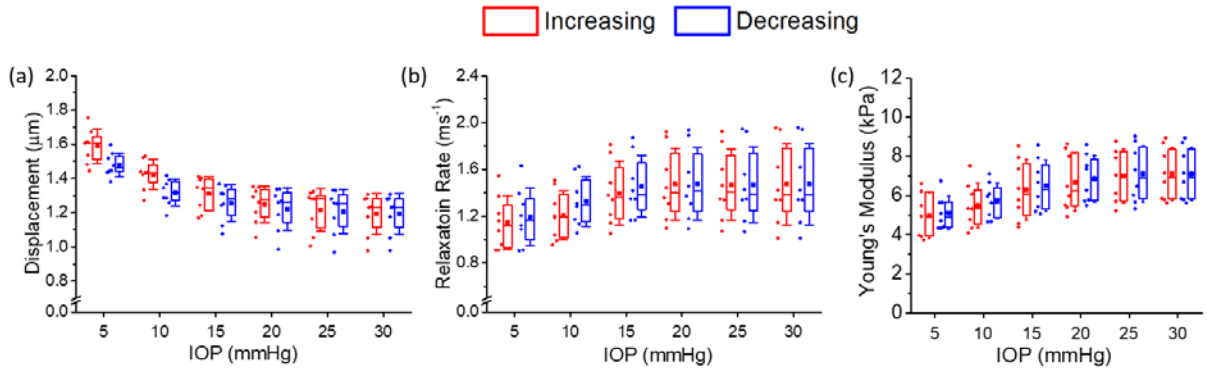


**Figure 5-4**: (a) Summary of maximum displacement, (b) relaxation rate of ARF-induced displacement, (c) Young's modulus of the lens as a function of IOP (n=8). Error bars represent one standard deviation calculated for different samples.

Figure 5-4 includes the summarized results of MDs, RRs and Young's moduli for all eight samples. Figure 5-4(a) shows that the MD decreased rapidly from an IOP of 5 mmHg (1.61±0.10 µm) until the IOP was 20 mmHg (1.26±0.11 µm), and then the MD slowly decreased until the IOP was 30 mmHg (1.20±0.12 µm). A noticeable hysteresis was observed while decreasing IOP, where the MD at 5 mmHg was 1.49±0.07 µm compared to 1.61±0.10 µm while increasing IOP. A similar, but opposite, trend was seen in the RRs as plotted in Figure 5-4(b). The RR at 5 mmHg IOP (1.14±0.23 $ms^{-1}$) rapidly increased as

the IOP increased up to 20 mmHg (1.47±0.31 $ms^{-1}$). However, once the IOP was further increased to 30 mmHg, there was no noticeable change in the RR (1.47±0.34 $ms^{-1}$). Similar to the MD, we measured a hysteresis, where the RR at 5 mmHg IOP while decreasing IOP (1.20±0.25 $ms^{-1}$) was different than when increasing IOP (1.14±0.23 $ms^{-1}$). The dependence of the Young's modulus on IOP ranging from 5 mmHg to 30 mmHg are summarized in Figure 4(c), where the means and standard deviations of the Young's moduli averaged for all samples are presented. Young's modulus increased from 4.98 kPa to 6.67 kPa for IOP changed from 5 mmHg to 20 mmHg, and up to 7.09 kPa for 30 mmHg. Similarly for MD and RR, the hysteresis was observed when IOP was decreased from 30 mmHg to 5 mmHg. In Table 5-1, the results for relaxation rates, displacement amplitudes, and Young's moduli are summarized for all samples.

**Table 5-1**: Summary of the maximum displacements (MD), relaxation rates (RR), and Young's moduli (E) from all samples (N=8). The data are presented as the inter-sample mean ± standard deviation.

| IOP (mmHg) | Increasing IOP | | | Decreasing IOP | | |
|---|---|---|---|---|---|---|
| | MD (μm) | RR ($ms^{-1}$) | E (kPa) | MD (μm) | RR ($ms^{-1}$) | E (kPa) |
| 5 | 1.61±0.10 | 1.14±0.23 | 4.98±1.16 | 1.49±0.07 | 1.20±0.25 | 5.11±0.86 |
| 10 | 1.44±0.09 | 1.21±0.21 | 5.49±1.15 | 1.33±0.08 | 1.32±0.21 | 5.72±0.91 |
| 15 | 1.32±0.10 | 1.39±0.27 | 6.29±1.54 | 1.27±0.11 | 1.45±0.26 | 6.50±1.32 |
| 20 | 1.26±0.11 | 1.47±0.31 | 6.67±1.48 | 1.23±0.12 | 1.48±0.31 | 6.85±1.20 |
| 25 | 1.23±0.13 | 1.47±0.30 | 7.00±1.37 | 1.22±0.13 | 1.47±0.32 | 7.12±1.44 |
| 30 | 1.20±0.12 | 1.47±0.34 | 7.09±1.33 | 1.20±0.12 | 1.47±0.34 | 7.09±1.33 |

## 5.4 Discussion

The phantom experiments confirmed that the RR, MD, and estimated Young's modulus correlate well with Young's modulus as measured by the gold standard of uniaxial mechanical testing. The results in this study demonstrate that the stiffness of the lens increases as the IOP increases, and this trend was observed in all eight samples and for all used mechanical characteristics. While increasing IOP, the RR of the ARF-induced displacement increased 28.9% from 5 mmHg to 20 mmHg, and then gradually stabilized after 20 mmHg up to 30 mmHg. The MD decreased 21.7% while increasing IOP from 5 mmHg to 20 mmHg but only decreased 4.7% when the IOP was further increased from 20 mmHg to 30 mmHg. While decreasing IOP, the RR decreased to $1.20\pm0.25\ s^{-1}$ at 5 mmHg IOP which is 5% higher than the initial RR at 5 mmHg IOP. Similarly, we also measured a hysteresis in the MD, which was 7% greater at 5 mmHg IOP while decreasing IOP as compared to increasing IOP. Young's modulus values demonstrated similar to RR trend increasing by 33.9% for IOP 20 mmHg, stabilizing up to 30 mmHg, and having hysteresis during decreasing IOP. All our OCE measurements were made immediately after the target IOP was reached, and our future work will investigate whether more time is required to reduce the observed biomechanical hysteresis and if a prolonged elevated IOP affects the degree of changes in the biomechanical properties of the lens. Nevertheless, the hysteresis was small and the overall changes in lenticular biomechanical properties due to an elevated IOP were reversed by lowering the IOP.

It is worthwhile to note that standard deviations of the MD and RR, and Young's modulus were relatively large. The ages of the samples were not controlled, and our previous work has shown that age has a drastic influence on the biomechanical properties

of the crystalline lens, albeit in rabbits. Such a significant inter-subject variability would most likely results from age differences. Nevertheless, the trend is clear that, regardless of age, the IOP has a significant influence on the lens stiffness.

We have shown that the stiffness of the lens generally increases as IOP increases, what is a result that the IOP change likely causes deformation of the crystalline lens, and consequent exhibition of the nonlinear elastic properties of the lens. The mechanical compression tests have confirmed such elastic nonlinearity of the crystalline lens, when the slope of the strain-stress relation grows with the strain level resulting to stiffening of the lens.

The relationship between IOP and biomechanical properties of crystalline lens has rarely been investigated previously due to the location of the lens within the eye-globe. Hence, the vast majority of research has focused on the influence of IOP on corneal biomechanical properties. However, many ocular diseases are correlated with an elevation IOP such as glaucoma. The present study shows that the biomechanical properties of the lens were also affected by IOP, but the changes were reversible in the short term. Recently, Park et al. studied the impact of IOP on elastic wave propagation in the bovine crystalline lens and cornea using ultrasound elastography, and demonstrated relatively insignificant increase in the elastic wave velocity in the lens compared to cornea, and our results show good agreement with their findings. Our results, and those presented in the work by Park et al., show a significantly less pronounced increase in lenticular stiffness when the IOP is increased, which is in contrast to the very large increases in the stiffness of cornea and sclera due to elevated IOPs that have been reported in the literatures. We observed more than five-fold increase in Young's modulus of the cornea, when IOP increases from 15 to

30 mmHg, while in the presented results for Young's modulus of the lens increased less than 15% for the same IOP increasing range. The effect of stiffening with IOP for lens is significantly less noticeable than for cornea. One of the possible explanations of the difference in the mechanical behavior between lens and cornea is that the lens is undergone less significant deformation during IOP elevation, such that nonlinear elastic properties of the lens do not play a significant role in the response to acoustic excitation.

One of the limitations of the used model-based approach includes an assumption that the lens is considered as a homogeneous half-space, while it is known that the porcine crystalline lens is an inhomogeneous object with a stiffness gradient inside. The estimated Young's moduli may mostly correspond to the superficial tissues located on the anterior side of the lens, which is softer than the central part. Therefore, this limitation of the model could result to the underestimation in the Young's modulus.

The biomechanical properties of the lens were quantified at each IOP. OCE measurements were made at the apex of the lens. However, the lens has a drastic stiffness gradient inside, which was not investigated in this study. Shear wave based OCE could be utilized to study the internal structure of lens since this method has demonstrated the capability of depth-resolved analysis of corneal stiffness. In addition, Brillouin microscopy could be also combined with OCE to investigate the spatial distribution of changes in lenticular biomechanical properties as a function of IOP.

## 5.5 Conclusion

In this chapter, we investigated the influence of IOP on the biomechanical properties of *in situ* porcine crystalline lenses with OCE, and the results showed that the stiffness of the lenses increased when the IOP was elevated. However, the effect of stiffening with IOP

for lens was significantly less pronounced than for cornea and sclera. The measurements were then repeated while the IOP was decreased, and the increase in lenticular stiffness was generally reversed once the IOP was decreased. Even though there was a small hysteresis while cycling IOP, the results demonstrate that the changes in lens elasticity is a reversible process in short term.

# Chapter 6 - Lorentz force OCE

In Chapter 4 and 5, an ARF-based excitation method combined with OCE is proposed to investigate the change in biomechanical properties of the crystalline lens. Like other elastography techniques, OCE is based on the principle of correlating the tissue deformation caused by external excitation to elasticity. Due to the various application environments of tissues of interest, it is important to select suitable stimulation techniques for OCE investigation. Therefore, there is a need for the development of new excitation method to extend the application fields of OCE techniques. In this chapter, a novel stimulation technique utilizing the Lorentz force is reported to induce an elastic wave in tissue and is further combined with an ultra-fast OCE system for elastography study. The results show that Lorentz force OCE was able to accurately assess the elasticity of tissue when compared with mechanical testing.

## 6.1 Introduction

The mechanical properties of tissue can provide critical information for detecting and monitoring the progression of disease [180, 181]. OCE has proved to be promising for biomechanical characterization of tissues with high spatial resolution and sensitivity. Currently, several excitation approaches have been developed as the mechanical loadings to combine with OCE for different applications. For example, air-pulse OCE has been used to investigate the elasticity of the cornea under various physiological conditions [1, 182]; US-OCE has demonstrated its capability in the study of viscoelasticity of crystalline lens [3, 183]; mechanical actuator excitation-based OCE has been utilized for tumor detection [159]; and the method of magnetic nanoparticles (MNPs) modulated by external magnetic

field has been demonstrated for quantitative assessment of stiffness in rabbit lung and muscle [184, 185]. When combined with OCE technique, each of these excitation methods could find its most suitable application of tissue characterization. Developing new excitation techniques for OCE will be beneficial for extending its clinical application area.

The ability of living tissue to conduct current has aroused great interest for researchers for decades. The induction of current in tissue has been used for various treatment in clinical practice [186, 187]. The electrical properties of tissue such as conductivity and permittivity are associated with physiological and pathological conditions. For example, previous studies have shown that malignant tumor tissue has significantly higher permittivity as compared to normal tissue. Therefore, conductivity and permittivity of tissues could be used as one of the effective markers for tissue diagnostics.

Due to the electrical conductivity properties of biological tissues, it is possible to generate electrical current within them. When the current flows through the tissue, Lorentz force is generated by the presence of the magnetic field. Lorentz force has been studied for biomedical imaging in magneto-acoustic tomography and Lorentz Force Electrical Impedance Tomography [188-190]. The production of Lorentz force causes localized tissue deformation and subsequent elastic wave propagation [191], which can be utilized as another method to perform dynamic elastography.

Conventional OCE techniques record the wave propagation by taking multiple M-mode images. These techniques require multiple excitations for each measurement, which results in long acquisition time that make them unfeasible for clinical use. For an ultra-fast OCE system with a ~1.5 MHz A-line scanning rate, shear wave propagation by conventional B-M mode imaging was able to be recorded with only a single excitation for each

measurement [6], which greatly reduces the acquisition time and minimizes potential tissue damage.

In this chapter, we demonstrate the feasibility of using the Lorentz force to induce an elastic wave inside tissue to study elasticity in combination with an ultra-fast OCE system. Validation experiments were performed on agar phantoms of different concentrations. The Young's moduli of porcine liver as estimated by OCE and mechanical testing were also compared. The results demonstrate that magnetic force OCE is an effective technique for assessing the elasticity of tissue.

## 6.2 Methods

The schematic of the experimental setup is shown in Figure 6-1. The Lorentz force OCE system was composed of a home-built ultra-fast OCT system and a magnetic field generator, which was used for the Lorentz force excitation. The OCT acquisition and Lorentz excitation were synchronized by a TTL trigger signal generated by the computer. The ultra-fast OCT system was based on a 4X buffered FDML swept source laser (OptoRes GmbH) with a scan rate of ~1.5 MHz, central wavelength of 1316 nm, scan range of 100 nm, and output power up to 160 mW. The axial resolution and phase stability of the system in air were ~16 μm and ~9.5 mrad, respectively. Scanning was performed by a resonant scanner over ~7.9 mm, resulting in a frame-rate of ~7.3 kHz. Due to scanning hysteresis, only the forward scan data was captured. For each measurement, 150 frames, corresponding to ~20 ms, were recorded for post processing.

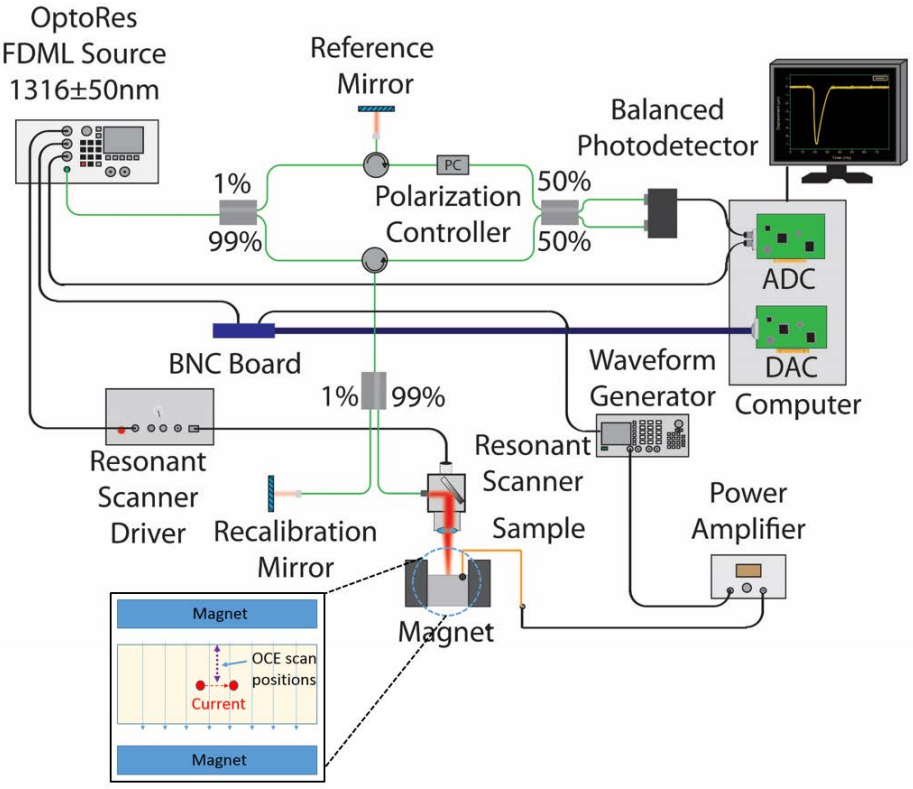


**Figure 6-1**: Schematic of the Lorentz OCE setup;

The Lorentz force excitation system consisted of two NdFeB magnets, two copper wire electrodes, an arbitrary waveform generator, and a power amplifier. The two magnets were separated by a mounting base to create a sample space of 5.0 cm x 2.5 cm x 1.5 cm. The small area of Lorentz force excitation was approximately located at the center of the sample space which has a magnetic field strength of ~3600 gauss. The arbitrary waveform generator output a 1.5 ms square pulse, which was then amplified up to a voltage of 20 to 60 V, depending on the conductivity of the sample. The amplified signal was fed into the sample by two electrodes, which were orthogonal to the magnetic field direction. The two electrodes were separated ~4 mm in a plastic bracket and connected to the sample. This ensured that the Lorentz force was parallel to the OCT scan direction. The current flowing

through the sample was measured by a digital multimeter connected in the excitation circuit.

In order to simulate soft tissue samples of controlled stiffness, agar phantoms of three different concentrations (1%, 1.5%, and 2% w/w) were cast by mixing agar powder, 5% salt, and distilled water. A small amount of milk was added to increase scattering. Porcine liver was collected fresh from a local butcher shop, and all experiments were performed within 24 hours after obtaining the liver. The Lorentz force driving signal was 20V in the phantoms and 60V in the porcine liver.

The phase data was converted to displacement and corrected for sample surface motion. The Young's modulus, *E*, was calculated from the elastic wave group velocity, $c_g$, by the surface wave equation for simplicity [192]:

$$E = \frac{2\rho(1+\upsilon)^3}{(0.87+1.12\upsilon)^2} c_g^2 \,, \tag{6.1}$$

where $\rho$=1070 kg/m$^3$ was the measured density of the agar phantoms, $\rho$=1045 kg/m$^3$ was the density of the porcine liver [193], and $\upsilon$=0.499 was the Poisson's ratio to account for the incompressible nature of the phantoms and liver [194]. All the samples were tested with a uniaxial mechanical compression testing system after OCE measurements.

## 6.3 Results

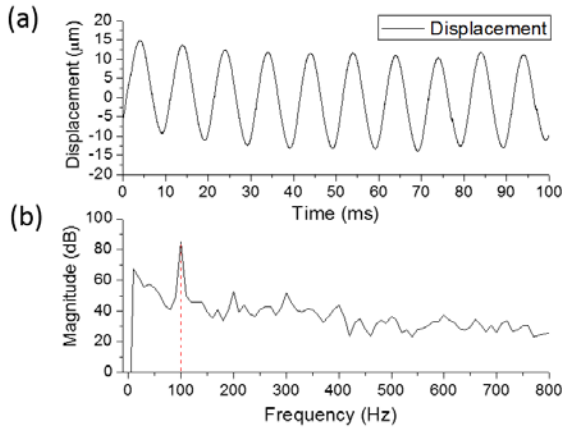


**Figure 6-2**: (a) Vertical temporal displacement profile of the agar sample when excited with a sinusoidal signal; (b) Spectrum of the displacement in (a) obtained by FFT.

Figure 6-2(a) shows the vertical temporal displacement profile from the surface of the sample when a 100 Hz sinusoidal voltage was used to power the Lorentz force driving current. As confirmed by the spectrum obtained by an FFT plotted in Figure 6-2(b), each cycle was 10 ms, which corresponded to the period of input signal.

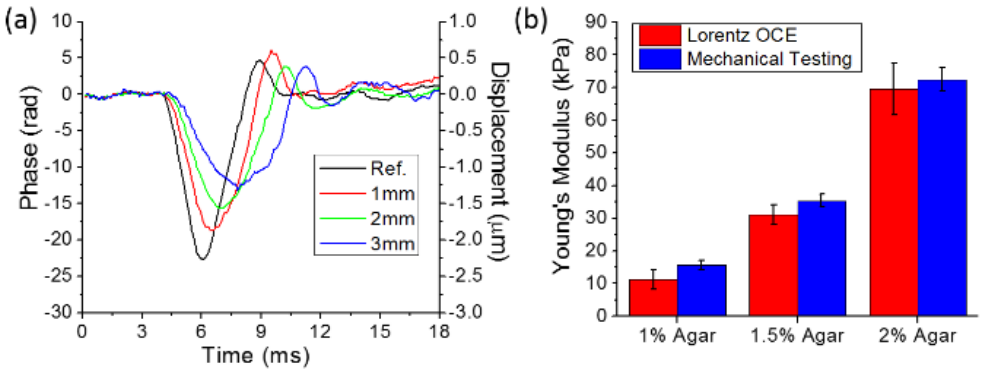


**Figure 6-3**: (a) Vertical temporal displacement profiles at the indicated distances from the reference OCE measurement position of a 2% agar sample; (b) Comparison of Young's modulus of agar phantoms as assessed by Lorentz OCE and uniaxial mechanical testing.

The elastic wave velocity for each sample was calculated by linearly fitting the propagation delays to the corresponding distances. The OCE measurement was taken aside

of the Lorentz excitation area. Within the excitation region no time delay was observed from the OCE because the whole excitation region experienced a similar displacement. The reference position was chosen where wave propagation delays started to be observed. Displacement profiles from the surface of a 2% agar sample at 1, 2 and 3 mm away from the reference position along the wave propagation direction are presented in Figure 6-3(a). The group velocities of the elastic wave in the 1%, 1.5%, and 2% phantoms were 1.86±0.24, 3.11±0.15, and 4.65±0.27 m/s, respectively. Figure 6-3(b) shows the comparison of Young's moduli of the agar phantoms as assessed by Lorentz force OCE and as measured by uniaxial mechanical testing. The Young's moduli of 1%, 1.5%, and 2% agar phantoms as estimated by Lorentz force OCE were 12.4±3.3, 34.3±3.2, and 76.6±8.8 kPa, respectively. Uniaxial mechanical testing showed that the elasticities of the 1%, 1.5%, and 2% agar phantoms were 15.6±1.4, 35.4±2.0, and 72.5±3.7 kPa, respectively. Figure 6-4 demonstrates the wave propagation in a spatially heterogeneous phantom made up of 1% agar on the left and 2% agar on the right. The elastic wave velocities were calculated as 1.81±0.13 m/s and 4.74±0.21 m/s on the 1% and 2% components respectively, showing the capability of using Lorentz force OCE to detect spatial variations in stiffness.

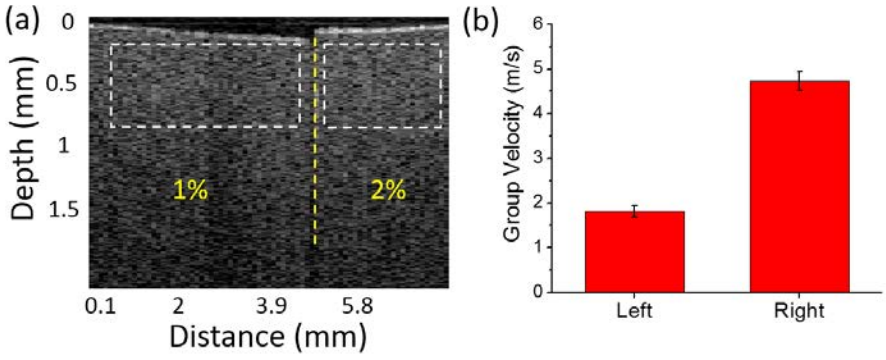


**Figure 6-4**: (a) The OCT structural image of the heterogeneous phantom; (b) Group velocity calculated from the selected windows.

Porcine liver was utilized to test the feasibility of Lorentz force OCE to quantify the stiffness of tissue. Figure 6-5(a) shows the elastic wave propagation at different time points after excitation overlaid on the OCT structural image of a porcine liver sample. The displacement is color mapped with blue as downwards and red as upwards displacement to better illustrate the wave propagation, and the Lorentz force excitation location lies at the left edge of the image. The elastic wave group velocity in the porcine liver was 1.83±0.05 m/s, which translated to a Young's modulus of 11.5±0.6 kPa by Equation (6.1). The stiffness of the porcine liver as measured by mechanical testing was 9.6±2.3 kPa. The OCE-measured elastic wave velocity corroborates with previous investigations [195].

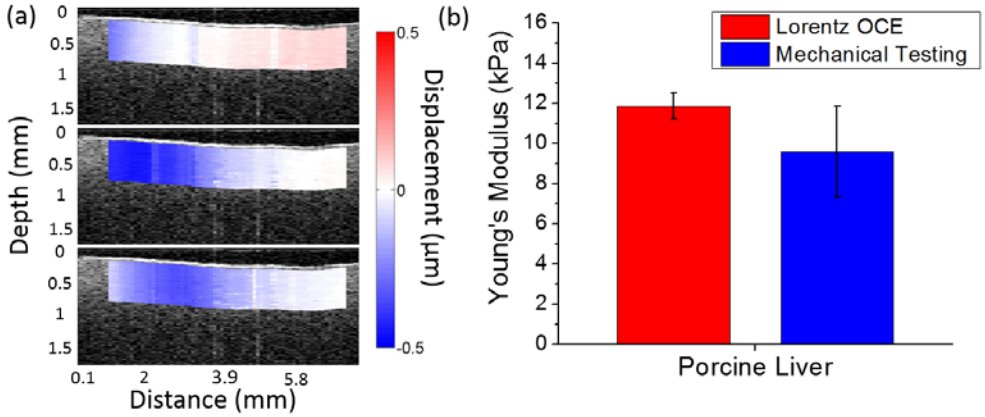


**Figure 6-5**: (a) The OCT structural image of a porcine liver sample and elastic wave propagation overlay; (b) Comparison of elasticity as assessed by Lorentz force OCE and as measured by uniaxial mechanical testing.

## 6.4 Discussion

The Lorentz force is a very new technique for elastographic excitation. Similar to MM-OCE, Lorentz force OCE needs an external magnetic field to induce a deformation. Lorentz excitation only relies on the internal conductive properties of tissue and the bioelectric current flow, so it is possible to be utilized in air and liquid environments. One advantage of Lorentz excitation is that the excitation frequency can be customized by changing the

driving signal frequency as shown in Figure 6-2(a), which makes it suitable for resonant spectroscopic study. The recent advances in techniques even make it possible to deliver the Lorentz excitation remotely without electrodes.

It should be noted that the OCE results shows better correlation with mechanical compression testing for agar samples compared to the porcine liver. This is primarily due to assumptions made about the sample in Equation 6.1. Since the viscosity of agar sample is usually very small and can be ignored, the Young's modulus obtained in agar by OCE and mechanical compression testing have a better match while the viscosity effect can be neglected. For liver tissue, there is viscosity which may affect the wave speed for OCE measurement. For compression testing, the viscosity has almost no influence on the elasticity measurement. Therefore, OCE-measured Young modulus and compression results for biological samples typically show greater variability.

The electrical current flow dictates where the Lorentz force will induce the deformation in the tissue. Since the current is generated between two electrodes, the excitation spot size depends on the distance between the two electrodes. Hence, the larger the distance between the electrodes, the greater the deformation area is. In order to ensure that the excitation was restricted to a small area, the electrodes were separated ~4 mm. The OCE scan region was proximal to the excitation to ensure that the elastic wave was properly imaged. By utilizing microelectrodes, the excitation spot size can further be reduced, and we are currently investigating their use for Lorentz force OCE.

The elastic wave time delay at different measurement locations was obtained by cross correlation of the displacement profiles between the starting reference position and other measurement positions. The strength of Lorentz force should only influence the amplitude

of the elastic wave instead of the elastic wave speed, however, low SNR will influence the accuracy of the cross correlation results, which further affects the OCE results. There are several methods to increase the displacement amplitude and improve SNR. Since the electric field, magnetic field and ion concentration of the tissue together dictate the amplitude of generated Lorentz force, the change of any of these parameters will help improve the signal. The most obvious method would be to increase the driving signal current or excitation duration. Another approach would be to increase the magnetic field strength. Clinical MRI systems generate magnetic fields at least 10 times stronger than what was used in this study, and a stronger magnetic field would increase the displacement amplitude without increasing the risk for tissue damage from a higher driving current. Increasing the conductivity of the tissue would also increase the elastic wave amplitude, and previous work has shown that a simple saline solution can accomplish this safely [196]. Future work will investigate the effects of the aforementioned techniques on the elastic wave amplitude and sensitivity of the Lorentz force OCE measurements.

The induction of current in tissue has been used for various treatment in clinical practice. One important issue for Lorentz force excitation is the potential tissue damage by pulsed electrical stimulation. The electrical current during excitation in liver was estimated to be 15 mA in this work, and it was still larger than suggested maximum in transcranial direct current stimulation -- up to 2 mA [197]. The maximum current an average man can bear is 16 mA based a 60 Hz AC current. Nevertheless, the excitation current needs to be reduced for *in vivo* use by aforementioned methods. In addition to electrical damage, resistive heating can also burn tissue. Since the pulse duration was only 1.5 ms, Joule heating should be negligible. However, the interaction between an electric field and tissue

is a complicated process which has been previously investigated using OCT [198, 199]. The electrical field change may cause various electro-kinetic responses such as electric field induced mechanical changes, especially *in vivo*. Due the relatively weak and short duration of the electric field, these changes are typically confined locally to the excitation position, but this deserves further investigation.

## 6.5 Conclusion

In this chapter, we have demonstrated a new Lorentz force stimulation based ultra-fast OCE technique for characterization of tissue mechanical properties. The results show that Lorentz force OCE was able to accurately assess the elasticity of tissue as compared to mechanical testing.

# Chapter 7 - Conclusion

This dissertation focuses on the improvement of OCT techniques to extend its applications in the biological tissue imaging and biomechanical characterization. Specifically, the work can be summarized in the following five aspects:

1) The development of a new OCT imaging methodology, named rotational imaging OCT (RI-OCT), to overcome the challenge of imaging depth and extend the applicability of OCT for imaging of mouse embryos at later stages like E9.5 and E10.5;
2) The comparison and combination of RI-OCT and SPIM for whole body morphological assessment of mouse embryos, which could provide more comprehensive tissue characterization for mouse embryonic research;
3) The demonstration of ultrasound excitation based OCE technique to investigate the age-related changes in the biomechanical properties of the crystalline lens;
4) The investigation of effects of intraocular pressure elevation on the biomechanical properties of crystalline lens with the US-OCE system;
5) The development and demonstration of Lorentz force method to induce elastic wave in biological tissue and combining with ultra-fast OCE technique to perform elastographic study.

With the advantages of high-resolution cross sectional-imaging capability, OCT has been used in various biomedical and clinical applications. However, due to the inherent limitations of OCT, its application is sometimes limited in certain biomedical settings. This dissertation aims to improve current OCT technique to adapt it in broader scenarios of biomedical science. The proposed RI-OCT technique and the effort to combine with SPIM contributes to better functional, morphological and biomolecular assessment of the targeted

biological samples, which is not limited in mouse embryonic research. Moreover, this dissertation also presents novel OCE techniques for tissue biomechanical characterization, particularly for crystalline lens, which has the potential for broad impact and adoption in pre-clinical and clinical applications.

## References


1. C. Wu, N. Sudheendran, M. Singh, I. V. Larina, M. E. Dickinson, and K. V. Larin, "Rotational imaging optical coherence tomography for full-body mouse embryonic imaging," *J Biomed Opt.* 21(2), 26002 (2016).
2. C. Wu, H. Le, S. Ran, M. Singh, I. V. Larina, D. Mayerich, M. E. Dickinson, and K. V. Larin, "Comparison and combination of rotational imaging optical coherence tomography and selective plane illumination microscopy for embryonic study," *Biomed Opt Express.* 8(10), 4629-4639 (2017).
3. C. Wu, Z. Han, S. Wang, J. Li, M. Singh, C. H. Liu, S. Aglyamov, S. Emelianov, F. Manns, and K. V. Larin, "Assessing age-related changes in the biomechanical properties of rabbit lens using a coaligned ultrasound and optical coherence elastography system," *Invest Ophthalmol Vis Sci.* 56(2), 1292-1300 (2015).
4. C. Wu, M. Singh, Z. Han, R. Raghunathan, C. H. Liu, J. Li, A. Schill, and K. V. Larin, "Lorentz force optical coherence elastography," *J Biomed Opt.* 21(9), 90502 (2016).
5. R. Raghunathan, C. Wu, M. Singh, C. H. Liu, R. C. Miranda, and K. V. Larin, "Evaluating the effects of maternal alcohol consumption on murine fetal brain vasculature using optical coherence tomography," *J Biophotonics.* 11(5), e201700238 (2018).
6. M. Singh, C. Wu, C.-H. Liu, J. Li, A. Schill, A. Nair, and K. V. Larin, "Phase-sensitive optical coherence elastography at 1.5 million A-Lines per second," *Opt Lett.* 40(11), 2588-2591 (2015).

7. R. Raghunathan, J. Zhang, C. Wu, J. Rippy, M. Singh, K. V. Larin, and G. Scarcelli, "Evaluating biomechanical properties of murine embryos using Brillouin microscopy and optical coherence tomography," *J Biomed Opt.* 22(8), 1-6 (2017).

8. C. H. Liu, A. Schill, C. Wu, M. Singh, and K. V. Larin, "Non-contact single shot elastography using line field low coherence holography," *Biomed Opt Express.* 7(8), 3021-3031 (2016).

9. Z. Han, J. Li, M. Singh, C. Wu, C. H. Liu, S. Wang, R. Idugboe, R. Raghunathan, N. Sudheendran, S. R. Aglyamov, M. D. Twa, and K. V. Larin, "Quantitative methods for reconstructing tissue biomechanical properties in optical coherence elastography: a comparison study," *Phys Med Biol.* 60(9), 3531-3547 (2015).

10. S. Wang, M. Singh, A. L. Lopez, 3rd, C. Wu, R. Raghunathan, A. Schill, J. Li, K. V. Larin, and I. V. Larina, "Direct four-dimensional structural and functional imaging of cardiovascular dynamics in mouse embryos with 1.5 MHz optical coherence tomography," *Opt Lett.* 40(20), 4791-4794 (2015).

11. Z. Han, J. Li, M. Singh, C. Wu, C. H. Liu, R. Raghunathan, S. R. Aglyamov, S. Vantipalli, M. D. Twa, and K. V. Larin, "Optical coherence elastography assessment of corneal viscoelasticity with a modified Rayleigh-Lamb wave model," *J Mech Behav Biomed Mater.* 66(87-94 (2017).

12. C. H. Liu, Y. Du, M. Singh, C. Wu, Z. Han, J. Li, A. Chang, C. Mohan, and K. V. Larin, "Classifying murine glomerulonephritis using optical coherence tomography and optical coherence elastography," *J Biophotonics.* 9(8), 781-791 (2016).

13. M. Singh, J. Li, Z. Han, C. Wu, S. R. Aglyamov, M. D. Twa, and K. V. Larin, "Investigating Elastic Anisotropy of the Porcine Cornea as a Function of Intraocular

Pressure With Optical Coherence Elastography," *J Refract Surg.* 32(8), 562-567 (2016).

14. C. H. Liu, A. Schill, R. Raghunathan, C. Wu, M. Singh, Z. Han, A. Nair, and K. V. Larin, "Ultra-fast line-field low coherence holographic elastography using spatial phase shifting," *Biomed Opt Express.* 8(2), 993-1004 (2017).
15. Z. Han, J. Li, M. Singh, S. R. Aglyamov, C. Wu, C. H. Liu, and K. V. Larin, "Analysis of the effects of curvature and thickness on elastic wave velocity in cornea-like structures by finite element modeling and optical coherence elastography," *Appl Phys Lett.* 106(23), 233702 (2015).
16. C.-H. Liu, J. Qi, J. Lu, S. Wang, C. Wu, W.-C. Shih, and K. V. Larin, "Improvement of tissue analysis and classification using optical coherence tomography combined with Raman spectroscopy," *J Innov Opt Health Sci.* 8(04), 1550006 (2015).
17. M. Singh, J. Li, Z. Han, S. Vantipalli, C. H. Liu, C. Wu, R. Raghunathan, S. R. Aglyamov, M. D. Twa, and K. V. Larin, "Evaluating the Effects of Riboflavin/UV-A and Rose-Bengal/Green Light Cross-Linking of the Rabbit Cornea by Noncontact Optical Coherence Elastography," *Invest Ophthalmol Vis Sci.* 57(9), Oct112-120 (2016).
18. Z. Han, J. Li, M. Singh, S. Vantipalli, S. R. Aglyamov, C. Wu, C.-H. Liu, R. Raghunathan, M. D. Twa, and K. V. Larin, "Analysis of the effect of the fluid-structure interface on elastic wave velocity in cornea-like structures by OCE and FEM," *Laser Phys Lett.* 13(3), 035602 (2016).
19. Z. Han, S. R. Aglyamov, J. Li, M. Singh, S. Wang, S. Vantipalli, C. Wu, C. H. Liu, M. D. Twa, and K. V. Larin, "Quantitative assessment of corneal viscoelasticity

using optical coherence elastography and a modified Rayleigh-Lamb equation," *J Biomed Opt.* 20(2), 20501 (2015).

20. M. Singh, R. Raghunathan, V. Piazza, A. M. Davis-Loiacono, A. Cable, T. J. Vedakkan, T. Janecek, M. V. Frazier, A. Nair, C. Wu, I. V. Larina, M. E. Dickinson, and K. V. Larin, "Applicability, usability, and limitations of murine embryonic imaging with optical coherence tomography and optical projection tomography," *Biomed Opt Express.* 7(6), 2295-2310 (2016).
21. M. Singh, J. Li, Z. Han, R. Raghunathan, A. Nair, C. Wu, C. H. Liu, S. Aglyamov, M. D. Twa, and K. V. Larin, "Assessing the effects of riboflavin/UV-A crosslinking on porcine corneal mechanical anisotropy with optical coherence elastography," *Biomed Opt Express.* 8(1), 349-366 (2017).
22. J. Zhang, R. Raghunathan, J. Rippy, C. Wu, R. Finnell, K. Larin, and G. Scarcelli, "Tissue Biomechanics during Cranial Neural Tube Closure Measured by Brillouin Microscopy and Optical Coherence Tomography," *Birth Defects Research.* (2018).
23. J. Fujimoto, and E. Swanson, "The Development, Commercialization, and Impact of Optical Coherence Tomography," *Invest Ophthalmol Vis Sci.* 57(9), Oct1-oct13 (2016).
24. D. Huang, E. A. Swanson, C. P. Lin, J. S. Schuman, W. G. Stinson, W. Chang, M. R. Hee, T. Flotte, K. Gregory, and C. A. Puliafito, "Optical coherence tomography," *Science.* 254(5035), 1178-1181 (1991).
25. J. M. Schmitt, "Optical coherence tomography (OCT): a review," *IEEE J. Sel. Top. Quantum Electron.* 5(4), 1205-1215 (1999).

26. A. M. Zysk, F. T. Nguyen, A. L. Oldenburg, D. L. Marks, and S. A. Boppart, "Optical coherence tomography: a review of clinical development from bench to bedside," *J Biomed Opt.* 12(5), 051403 (2007).

27. E. Sattler, R. Kastle, and J. Welzel, "Optical coherence tomography in dermatology," *J Biomed Opt.* 18(6), 061224 (2013).

28. R. Raghunathan, M. Singh, M. E. Dickinson, and K. V. Larin, "Optical coherence tomography for embryonic imaging: a review," *J Biomed Opt.* 21(5), 50902 (2016).

29. T. L. Szabo, "Diagnostic ultrasound imaging: inside out", Academic Press (2004).

30. F. S. Foster, C. J. Pavlin, K. A. Harasiewicz, D. A. Christopher, and D. H. Turnbull, "Advances in ultrasound biomicroscopy," *Ultrasound Med Biol.* 26(1), 1-27 (2000).

31. V. Ntziachristos, "Going deeper than microscopy: the optical imaging frontier in biology," *Nat Methods.* 7(8), 603-614 (2010).

32. K. Takada, I. Yokohama, K. Chida, and J. Noda, "New measurement system for fault location in optical waveguide devices based on an interferometric technique," *Appl Opt.* 26(9), 1603-1606 (1987).

33. H. H. Gilgen, R. P. Novak, R. P. Salathe, W. Hodel, and P. Beaud, "Submillimeter optical reflectometry," *J Light Technol.* 7(8), 1225-1233 (1989).

34. A. Fercher, K. Mengedoht, and W. Werner, "Eye-length measurement by interferometry with partially coherent light," *Opt Lett.* 13(3), 186-188 (1988).

35. E. A. Swanson, J. A. Izatt, M. R. Hee, D. Huang, C. P. Lin, J. S. Schuman, C. A. Puliafito, and J. G. Fujimoto, "In vivo retinal imaging by optical coherence tomography," *Opt Lett.* 18(21), 1864-1866 (1993).

36. M. Choma, M. Sarunic, C. Yang, and J. Izatt, "Sensitivity advantage of swept source and Fourier domain optical coherence tomography," *Opt Express.* 11(18), 2183-2189 (2003).

37. J. F. de Boer, R. Leitgeb, and M. Wojtkowski, "Twenty-five years of optical coherence tomography: the paradigm shift in sensitivity and speed provided by Fourier domain OCT [Invited]," *Biomed Opt Express.* 8(7), 3248-3280 (2017).

38. A. F. Fercher, C. K. Hitzenberger, G. Kamp, and S. Y. El-Zaiat, "Measurement of intraocular distances by backscattering spectral interferometry," *Opt Commun.* 117(1), 43-48 (1995).

39. G. Ha Usler, and M. W. Lindner, ""Coherence radar" and "spectral radar"-new tools for dermatological diagnosis," *J Biomed Opt.* 3(1), 21-31 (1998).

40. S. R. Chinn, E. A. Swanson, and J. G. Fujimoto, "Optical coherence tomography using a frequency-tunable optical source," *Opt Lett.* 22(5), 340-342 (1997).

41. B. Golubovic, B. E. Bouma, G. J. Tearney, and J. G. Fujimoto, "Optical frequency-domain reflectometry using rapid wavelength tuning of a Cr4+:forsterite laser," *Opt Lett.* 22(22), 1704-1706 (1997).

42. F. Lexer, C. K. Hitzenberger, A. F. Fercher, and M. Kulhavy, "Wavelength-tuning interferometry of intraocular distances," *Appl Opt.* 36(25), 6548-6553 (1997).

43. V. J. Srinivasan, R. Huber, I. Gorczynska, J. G. Fujimoto, J. Y. Jiang, P. Reisen, and A. E. Cable, "High-speed, high-resolution optical coherence tomography retinal imaging with a frequency-swept laser at 850 nm," *Opt Lett.* 32(4), 361-363 (2007).

44. R. Huber, M. Wojtkowski, J. G. Fujimoto, J. Y. Jiang, and A. E. Cable, "Three-dimensional and C-mode OCT imaging with a compact, frequency swept laser source at 1300 nm," *Opt Express.* 13(26), 10523-10538 (2005).

45. R. Huber, M. Wojtkowski, K. Taira, J. Fujimoto, and K. Hsu, "Amplified, frequency swept lasers for frequency domain reflectometry and OCT imaging: design and scaling principles," *Opt Express.* 13(9), 3513-3528 (2005).

46. J. Zhang, J. S. Nelson, and Z. Chen, "Removal of a mirror image and enhancement of the signal-to-noise ratio in Fourier-domain optical coherence tomography using an electro-optic phase modulator," *Opt Lett.* 30(2), 147-149 (2005).

47. A. F. Fercher, W. Drexler, C. K. Hitzenberger, and T. Lasser, "Optical coherence tomography-principles and applications," *Rep Prog Phys.* 66(2), 239 (2003).

48. A. Fercher, C. Hitzenberger, M. Sticker, R. Zawadzki, B. Karamata, and T. Lasser, "Numerical dispersion compensation for Partial Coherence Interferometry and Optical Coherence Tomography," *Opt Express.* 9(12), 610-615 (2001).

49. N. Lippok, S. Coen, P. Nielsen, and F. Vanholsbeeck, "Dispersion compensation in Fourier domain optical coherence tomography using the fractional Fourier transform," *Opt Express.* 20(21), 23398-23413 (2012).

50. M. Wojtkowski, V. Srinivasan, T. Ko, J. Fujimoto, A. Kowalczyk, and J. Duker, "Ultrahigh-resolution, high-speed, Fourier domain optical coherence tomography and methods for dispersion compensation," *Opt Express.* 12(11), 2404-2422 (2004).

51. W. Drexler, and J. G. Fujimoto, "Optical coherence tomography: technology and applications", Springer Science & Business Media (2008).

52. V. V. Tuchin, and V. Tuchin, "Tissue optics: light scattering methods and instruments for medical diagnosis," (2007).

53. R. Leitgeb, C. Hitzenberger, and A. Fercher, "Performance of fourier domain vs. time domain optical coherence tomography," *Opt Express.* 11(8), 889-894 (2003).

54. J. F. de Boer, B. Cense, B. H. Park, M. C. Pierce, G. J. Tearney, and B. E. Bouma, "Improved signal-to-noise ratio in spectral-domain compared with time-domain optical coherence tomography," *Opt Lett.* 28(21), 2067-2069 (2003).

55. S. Yun, G. Tearney, B. Bouma, B. Park, and J. de Boer, "High-speed spectral-domain optical coherence tomography at 1.3 mum wavelength," *Opt Express.* 11(26), 3598-3604 (2003).

56. S. Moon, S.-W. Lee, and Z. Chen, "Reference spectrum extraction and fixed-pattern noise removal in optical coherence tomography," *Opt Express.* 18(24), 24395-24404 (2010).

57. S. Makita, T. Fabritius, and Y. Yasuno, "Full-range, high-speed, high-resolution 1-μm spectral-domain optical coherence tomography using BM-scan for volumetric imaging of the human posterior eye," *Opt Express.* 16(12), 8406-8420 (2008).

58. Z. Hu, and A. M. Rollins, "Fourier domain optical coherence tomography with a linear-in-wavenumber spectrometer," *Opt Lett.* 32(24), 3525-3527 (2007).

59. G. Lan, and G. Li, "Design of a k-space spectrometer for ultra-broad waveband spectral domain optical coherence tomography," *Sci Rep.* 7(42353 (2017).

60. S. S. Gao, Y. Jia, M. Zhang, J. P. Su, G. Liu, T. S. Hwang, S. T. Bailey, and D. Huang, "Optical Coherence Tomography Angiography," *Invest Ophthalmol Vis Sci.* 57(9), OCT27-OCT36 (2016).

61. K. V. Larin, and D. D. Sampson, "Optical coherence elastography - OCT at work in tissue biomechanics [Invited]," *Biomed Opt Express.* 8(2), 1172-1202 (2017).

62. J. Men, Y. Huang, J. Solanki, X. Zeng, A. Alex, J. Jerwick, Z. Zhang, R. E. Tanzi, A. Li, and C. Zhou, "Optical Coherence Tomography for Brain Imaging and Developmental Biology," *IEEE J Sel Top Quantum Electron.* 22(4), (2016).

63. J. J. Edwards, and B. D. Gelb, "Genetics of congenital heart disease," *Curr Opin Cardiol.* 31(3), 235-241 (2016).

64. R. D. Wilson, "Prenatal screening, diagnosis, and pregnancy management of fetal neural tube defects," *J Obstet Gynaecol Can.* 36(10), 927-939 (2014).

65. S. Bergstrom, H. Carr, G. Petersson, O. Stephansson, A. K. Bonamy, A. Dahlstrom, C. P. Halvorsen, and S. Johansson, "Trends in Congenital Heart Defects in Infants With Down Syndrome," *Pediatrics.* 138(1), (2016).

66. L. M. Almli, C. C. Alter, R. B. Russell, S. C. Tinker, P. P. Howards, J. Cragan, E. Petersen, G. E. Carrino, and J. Reefhuis, "Association Between Infant Mortality Attributable to Birth Defects and Payment Source for Delivery - United States, 2011-2013," *MMWR Morb Mortal Wkly Rep.* 66(3), 84-87 (2017).

67. U. B. Pandey, and C. D. Nichols, "Human disease models in Drosophila melanogaster and the role of the fly in therapeutic drug discovery," *Pharmacol Rev.* 63(2), 411-436 (2011).

68. K. Dooley, and L. I. Zon, "Zebrafish: a model system for the study of human disease," *Curr Opin Genet Dev.* 10(3), 252-256 (2000).

69. A. Ny, M. Koch, M. Schneider, E. Neven, R. T. Tong, S. Maity, C. Fischer, S. Plaisance, D. Lambrechts, C. Heligon, S. Terclavers, M. Ciesiolka, R. Kalin, W. Y.

Man, I. Senn, S. Wyns, F. Lupu, A. Brandli, K. Vleminckx, D. Collen, M. Dewerchin, E. M. Conway, L. Moons, R. K. Jain, and P. Carmeliet, "A genetic Xenopus laevis tadpole model to study lymphangiogenesis," *Nat Med.* 11(9), 998-1004 (2005).

70. S. Batzoglou, L. Pachter, J. P. Mesirov, B. Berger, and E. S. Lander, "Human and mouse gene structure: comparative analysis and application to exon prediction," *Genome Res.* 10(7), 950-958 (2000).

71. A. I. Su, T. Wiltshire, S. Batalov, H. Lapp, K. A. Ching, D. Block, J. Zhang, R. Soden, M. Hayakawa, G. Kreiman, M. P. Cooke, J. R. Walker, and J. B. Hogenesch, "A gene atlas of the mouse and human protein-encoding transcriptomes," *Proc Natl Acad Sci U S A.* 101(16), 6062-6067 (2004).

72. J. Graw, "Mouse models of congenital cataract," *Eye.* 13(438-444 (1999).

73. D. M. Juriloff, and M. J. Harris, "Mouse models for neural tube closure defects," *Hum Mol Genet.* 9(6), 993-1000 (2000).

74. S. D. Brown, W. Wurst, R. Kuhn, and J. M. Hancock, "The functional annotation of mammalian genomes: the challenge of phenotyping," *Annu Rev Genet.* 43(305-333 (2009).

75. M. A. Bogue, and S. C. Grubb, "The Mouse Phenome Project," *Genetica.* 122(1), 71-74 (2004).

76. A. L. Lopez, 3rd, M. D. Garcia, M. E. Dickinson, and I. V. Larina, "Live confocal microscopy of the developing mouse embryonic yolk sac vasculature," *Methods Mol Biol.* 1214(163-172 (2015).

77. J. Sharpe, U. Ahlgren, P. Perry, B. Hill, A. Ross, J. Hecksher-Sorensen, R. Baldock, and D. Davidson, "Optical projection tomography as a tool for 3D microscopy and gene expression studies," *Science.* 296(5567), 541-545 (2002).

78. F. S. Foster, M. Zhang, A. S. Duckett, V. Cucevic, and C. J. Pavlin, "In vivo imaging of embryonic development in the mouse eye by ultrasound biomicroscopy," *Invest Ophthalmol Vis Sci.* 44(6), 2361-2366 (2003).

79. B. Hogers, D. Gross, V. Lehmann, K. Zick, H. J. De Groot, A. C. Gittenberger-De Groot, and R. E. Poelmann, "Magnetic resonance microscopy of mouse embryos in utero," *Anat Rec.* 260(4), 373-377 (2000).

80. R. M. Zucker, E. S. Hunter, 3rd, and J. M. Rogers, "Apoptosis and morphology in mouse embryos by confocal laser scanning microscopy," *Methods.* 18(4), 473-480 (1999).

81. D. H. Turnbull, and S. Mori, "MRI in mouse developmental biology," *NMR Biomed.* 20(3), 265-274 (2007).

82. D. H. Turnbull, T. S. Bloomfield, H. S. Baldwin, F. S. Foster, and A. L. Joyner, "Ultrasound backscatter microscope analysis of early mouse embryonic brain development," *Proc Natl Acad Sci U S A.* 92(6), 2239-2243 (1995).

83. J. R. Walls, L. Coultas, J. Rossant, and R. M. Henkelman, "Three-dimensional analysis of vascular development in the mouse embryo," *PLoS One.* 3(8), e2853 (2008).

84. A. A. Lindenmaier, L. Conroy, G. Farhat, R. S. DaCosta, C. Flueraru, and I. A. Vitkin, "Texture analysis of optical coherence tomography speckle for characterizing biological tissues in vivo," *Opt Lett.* 38(8), 1280-1282 (2013).

85. M. J. Paszek, N. Zahir, K. R. Johnson, J. N. Lakins, G. I. Rozenberg, A. Gefen, C. A. Reinhart-King, S. S. Margulies, M. Dembo, D. Boettiger, D. A. Hammer, and V. M. Weaver, "Tensional homeostasis and the malignant phenotype," *Cancer Cell.* 8(3), 241-254 (2005).

86. A. Sarvazyan, T. J. Hall, M. W. Urban, M. Fatemi, S. R. Aglyamov, and B. S. Garra, "An Overview of Elastography-An Emerging Branch of Medical Imaging," *Curr Med Imaging Rev.* 7(4), 255-282 (2011).

87. R. Sinkus, J. L. Daire, V. Vilgrain, and B. E. Van Beers, "Elasticity Imaging via MRI: Basics, Overcoming the Waveguide Limit, and Clinical Liver Results," *Curr Med Imaging Rev.* 8(1), 56-63 (2012).

88. R. Muthupillai, D. J. Lomas, P. J. Rossman, J. F. Greenleaf, A. Manduca, and R. L. Ehman, "Magnetic-Resonance Elastography by Direct Visualization of Propagating Acoustic Strain Waves," *Science.* 269(5232), 1854-1857 (1995).

89. J. Schmitt, "OCT elastography: imaging microscopic deformation and strain of tissue," *Opt Express.* 3(6), 199-211 (1998).

90. R. M. S. Sigrist, J. Liau, A. E. Kaffas, M. C. Chammas, and J. K. Willmann, "Ultrasound Elastography: Review of Techniques and Clinical Applications," *Theranostics.* 7(5), 1303-1329 (2017).

91. Y. K. Mariappan, K. J. Glaser, and R. L. Ehman, "Magnetic resonance elastography: a review," *Clin Anat.* 23(5), 497-511 (2010).

92. B. F. Kennedy, P. Wijesinghe, and D. D. Sampson, "The emergence of optical elastography in biomedicine," *Nat Photonics.* 11(215 (2017).

93. C. Sun, B. Standish, B. Vuong, X. Y. Wen, and V. Yang, "Digital image correlation-based optical coherence elastography," *J Biomed Opt.* 18(12), 121515 (2013).

94. B. F. Kennedy, X. Liang, S. G. Adie, D. K. Gerstmann, B. C. Quirk, S. A. Boppart, and D. D. Sampson, "In vivo three-dimensional optical coherence elastography," *Opt Express.* 19(7), 6623-6634 (2011).

95. B. F. Kennedy, K. M. Kennedy, and D. D. Sampson, "A Review of Optical Coherence Elastography: Fundamentals, Techniques and Prospects," *Ieee J Sel Top Quant.* 20(2), (2014).

96. W. J. Qi, R. M. Chen, L. Chou, G. J. Liu, J. Zhang, Q. F. Zhou, and Z. P. Chen, "Phase-resolved acoustic radiation force optical coherence elastography," *J Biomed Opt.* 17(11), (2012).

97. B. F. Kennedy, T. R. Hillman, R. A. McLaughlin, B. C. Quirk, and D. D. Sampson, "In vivo dynamic optical coherence elastography using a ring actuator," *Opt Express.* 17(24), 21762-21772 (2009).

98. T. M. Nguyen, S. Song, B. Arnal, E. Y. Wong, Z. Huang, R. K. Wang, and M. O'Donnell, "Shear wave pulse compression for dynamic elastography using phase-sensitive optical coherence tomography," *J Biomed Opt.* 19(1), 16013 (2014).

99. S. Wang, K. Larin, J. Li, S. Vantipalli, R. Manapuram, S. Aglyamov, S. Emelianov, and M. Twa, "A focused air-pulse system for optical-coherence-tomography-based measurements of tissue elasticity," *Laser Phys Lett.* 10(7), 075605 (2013).

100. J. Li, S. Wang, M. Singh, S. Aglyamov, S. Emelianov, M. Twa, and K. Larin, "Air-pulse OCE for assessment of age-related changes in mouse cornea in vivo," *Laser Phys Lett.* 11(6), 065601 (2014).

101. W. J. Qi, R. Li, T. Ma, K. K. Shung, Q. F. Zhou, and Z. P. Chen, "Confocal acoustic radiation force optical coherence elastography using a ring ultrasonic transducer," *Appl Phys Lett.* 104(12), (2014).

102. J. G. Fujimoto, C. Pitris, S. A. Boppart, and M. E. Brezinski, "Optical coherence tomography: an emerging technology for biomedical imaging and optical biopsy," *Neoplasia.* 2(1-2), 9-25 (2000).

103. I. V. Larina, S. H. Syed, N. Sudheendran, P. A. Overbeek, M. E. Dickinson, and K. V. Larin, "Optical coherence tomography for live phenotypic analysis of embryonic ocular structures in mouse models," *J Biomed Opt.* 17(8), 081410-081411 (2012).

104. W. Wieser, W. Draxinger, T. Klein, S. Karpf, T. Pfeiffer, and R. Huber, "High definition live 3D-OCT in vivo: design and evaluation of a 4D OCT engine with 1 GVoxel/s," *Biomed Opt Express.* 5(9), 2963-2977 (2014).

105. D. Zhu, K. V. Larin, Q. Luo, and V. V. Tuchin, "Recent progress in tissue optical clearing," *Laser Photon Rev.* 7(5), 732-757 (2013).

106. V. Rankov, R. J. Locke, R. J. Edens, P. R. Barber, and B. Vojnovic, "An Algorithm for image stitching and blending," *Proc SPIE* 190-199 (2005).

107. B. B. Keller, M. J. MacLennan, J. P. Tinney, and M. Yoshigi, "In vivo assessment of embryonic cardiovascular dimensions and function in day-10.5 to -14.5 mouse embryos," *Circ Res.* 79(2), 247-255 (1996).

108. M. Cua, E. Lin, L. Lee, X. Sheng, K. S. Wong, G. F. Tibbits, M. F. Beg, and M. V. Sarunic, "Morphological phenotyping of mouse hearts using optical coherence tomography," *J Biomed Opt.* 19(11), 116007 (2014).

109. P. P. Tam, "Postimplantation mouse development: whole embryo culture and micro-manipulation," *Int J Dev Biol.* 42(7), 895-902 (1998).

110. A. Kasarskis, K. Manova, and K. V. Anderson, "A phenotype-based screen for embryonic lethal mutations in the mouse," *Proc Natl Acad Sci U S A.* 95(13), 7485-7490 (1998).

111. T. E. Willnow, J. Hilpert, S. A. Armstrong, A. Rohlmann, R. E. Hammer, D. K. Burns, and J. Herz, "Defective forebrain development in mice lacking gp330/megalin," *Proc Natl Acad Sci U S A.* 93(16), 8460-8464 (1996).

112. M. W. Jenkins, P. Patel, H. Deng, M. M. Montano, M. Watanabe, and A. M. Rollins, "Phenotyping transgenic embryonic murine hearts using optical coherence tomography," *Appl Opt.* 46(10), 1776-1781 (2007).

113. X. Liu, K. Tobita, R. J. Francis, and C. W. Lo, "Imaging techniques for visualizing and phenotyping congenital heart defects in murine models," *Birth Defects Res C Embryo Today*. 99(2), 93-105 (2013).

114. G. Karunamuni, S. Gu, Y. Q. Doughman, A. I. Noonan, A. M. Rollins, M. W. Jenkins, and M. Watanabe, "Using optical coherence tomography to rapidly phenotype and quantify congenital heart defects associated with prenatal alcohol exposure," *Dev Dyn.* 244(4), 607-618 (2015).

115. M. W. Jenkins, M. Watanabe, and A. M. Rollins, "Longitudinal Imaging of Heart Development With Optical Coherence Tomography," *IEEE J Sel Top Quantum Electron.* 18(3), 1166-1175 (2012).

116. B. A. Filas, I. R. Efimov, and L. A. Taber, "Optical coherence tomography as a tool for measuring morphogenetic deformation of the looping heart," *Anat Rec.* 290(9), 1057-1068 (2007).

117. S. Wang, M. D. Garcia, A. L. Lopez, P. A. Overbeek, K. V. Larin, and I. V. Larina, "Dynamic imaging and quantitative analysis of cranial neural tube closure in the mouse embryo using optical coherence tomography," *Biomed Opt Express.* 8(1), 407-419 (2017).

118. J. Huisken, J. Swoger, F. Del Bene, J. Wittbrodt, and E. H. Stelzer, "Optical sectioning deep inside live embryos by selective plane illumination microscopy," *Science.* 305(5686), 1007-1009 (2004).

119. P. J. Keller, and E. H. Stelzer, "Quantitative in vivo imaging of entire embryos with Digital Scanned Laser Light Sheet Fluorescence Microscopy," *Curr Opin Neurobiol.* 18(6), 624-632 (2008).

120. J. Huisken, and D. Y. Stainier, "Selective plane illumination microscopy techniques in developmental biology," *Development.* 136(12), 1963-1975 (2009).

121. R. K. Ejsmont, M. Sarov, S. Winkler, K. A. Lipinski, and P. Tomancak, "A toolkit for high-throughput, cross-species gene engineering in Drosophila," *Nat Methods.* 6(6), 435-437 (2009).

122. P. J. Keller, A. D. Schmidt, J. Wittbrodt, and E. H. Stelzer, "Reconstruction of zebrafish early embryonic development by scanned light sheet microscopy," *Science.* 322(5904), 1065-1069 (2008).

123. H. U. Dodt, U. Leischner, A. Schierloh, N. Jahrling, C. P. Mauch, K. Deininger, J. M. Deussing, M. Eder, W. Zieglgansberger, and K. Becker, "Ultramicroscopy: three-dimensional visualization of neuronal networks in the whole mouse brain," *Nat Methods.* 4(4), 331-336 (2007).

124. J. L. Lucitti, E. A. V. Jones, C. Huang, J. Chen, S. E. Fraser, and M. E. Dickinson, "Vascular remodeling of the mouse yolk sac requires hemodynamic force," *Development.* 134(18), 3317-3326 (2007).

125. D. Zhu, K. V. Larin, Q. Luo, and V. V. Tuchin, "Recent progress in tissue optical clearing," *Laser Photon Rev.* 7(5), 732-757 (2013).

126. M. Mickoleit, B. Schmid, M. Weber, F. O. Fahrbach, S. Hombach, S. Reischauer, and J. Huisken, "High-resolution reconstruction of the beating zebrafish heart," *Nat Methods.* 11(9), 919-922 (2014).

127. J. Icha, C. Schmied, J. Sidhaye, P. Tomancak, S. Preibisch, and C. Norden, "Using Light Sheet Fluorescence Microscopy to Image Zebrafish Eye Development," *J Vis Exp.* 110), 53966 (2016).

128. N. Sudheendran, S. H. Syed, M. E. Dickinson, I. V. Larina, and K. V. Larin, "Speckle variance OCT imaging of the vasculature in live mammalian embryos," *Laser Phys Lett.* 8(3), 247 (2011).

129. G. Liu, W. Qi, L. Yu, and Z. Chen, "Real-time bulk-motion-correction free Doppler variance optical coherence tomography for choroidal capillary vasculature imaging," *Opt Express.* 19(4), 3657-3666 (2011).

130. R. K. Wang, and L. An, "Doppler optical micro-angiography for volumetric imaging of vascular perfusion in vivo," *Opt Express.* 17(11), 8926-8940 (2009).

131. I. V. Larina, S. Ivers, S. Syed, M. E. Dickinson, and K. V. Larin, "Hemodynamic measurements from individual blood cells in early mammalian embryos with Doppler swept source OCT," *Opt Lett.* 34(7), 986-988 (2009).

132. R. S. Udan, V. G. Piazza, C. Hsu, A. K. Hadjantonakis, and M. E. Dickinson, "Quantitative imaging of cell dynamics in mouse embryos using light-sheet microscopy," *Development.* 141(22), 4406-4414 (2014).

133. Y. N. Tallini, B. Shui, K. S. Greene, K. Y. Deng, R. Doran, P. J. Fisher, W. Zipfel, and M. I. Kotlikoff, "BAC transgenic mice express enhanced green fluorescent protein in central and peripheral cholinergic neurons," *Physiol Genomics.* 27(3), 391-397 (2006).

134. Y. S. Huang, H. Y. Ku, Y. C. Tsai, C. H. Chang, S. H. Pao, Y. H. Sun, and A. Chiou, "5D imaging via light sheet microscopy reveals cell dynamics during the eye-antenna disc primordium formation in Drosophila," *Sci Rep.* 7(44945 (2017).

135. T. V. Truong, W. Supatto, D. S. Koos, J. M. Choi, and S. E. Fraser, "Deep and fast live imaging with two-photon scanned light-sheet microscopy," *Nat Methods.* 8(9), 757-760 (2011).

136. T. Vettenburg, H. I. Dalgarno, J. Nylk, C. Coll-Llado, D. E. Ferrier, T. Cizmar, F. J. Gunn-Moore, and K. Dholakia, "Light-sheet microscopy using an Airy beam," *Nat Methods.* 11(5), 541-544 (2014).

137. A. Bassi, B. Schmid, and J. Huisken, "Optical tomography complements light sheet microscopy for in toto imaging of zebrafish development," *Development.* 142(5), 1016-1020 (2015).

138. J. Mayer, A. Robert-Moreno, R. Danuser, J. V. Stein, J. Sharpe, and J. Swoger, "OPTiSPIM: integrating optical projection tomography in light sheet microscopy extends specimen characterization to nonfluorescent contrasts," *Opt Lett.* 39(4), 1053-1056 (2014).

139. J. F. Colas, and J. Sharpe, "Live optical projection tomography," *Organogenesis.* 5(4), 211-216 (2009).

140. W. N. Charman, "The eye in focus: accommodation and presbyopia," *Clin Exp Optom.* 91(3), 207-225 (2008).

141. A. Glasser, and M. C. W. Campbell, "Presbyopia and the optical changes in the human crystalline lens with age," *Vision Res.* 38(2), 209-229 (1998).

142. K. R. Heys, S. L. Cram, and R. J. W. Truscott, "Massive increase in the stiffness of the human lens nucleus with age: the basis for presbyopia?," *Mol Vis.* 10(114), 956-963 (2004).

143. A. Glasser, M. A. Croft, and P. L. Kaufman, "Aging of the human crystalline lens and presbyopia," *Int Ophthalmol Clin.* 41(2), 1-15 (2001).

144. H. Pau, and J. Kranz, "The increasing sclerosis of the human lens with age and its relevance to accommodation and presbyopia," *Graefes Arch Clin Exp Ophthalmol.* 229(3), 294-296 (1991).

145. S. Yoon, S. Aglyamov, A. Karpiouk, and S. Emelianov, "The mechanical properties of ex vivo bovine and porcine crystalline lenses: age-related changes and location-dependent variations," *Ultrasound Med Biol.* 39(6), 1120-1127 (2013).

146. M. Reilly, and N. Ravi, "Microindentation of the Young Porcine Ocular Lens," *J Biomech Eng-T Asme.* 131(4), (2009).

147. T. N. Erpelding, K. W. Hollman, and M. O'Donnell, "Mapping age-related elasticity changes in porcine lenses using bubble-based acoustic radiation force," *Exp Eye Res.* 84(2), 332-341 (2007).

148. K. W. Hollman, M. O'Donnell, and T. N. Erpelding, "Mapping elasticity in human lenses using bubble-based acoustic radiation force," *Exp Eye Res.* 85(6), 890-893 (2007).

149. H. Lubatschowski, S. Schumacher, M. Fromm, A. Wegener, H. Hoffmann, U. Oberheide, and G. Gerten, "Femtosecond lentotomy: generating gliding planes inside the crystalline lens to regain accommodation ability," *J Biophotonics.* 3(5-6), 265-268 (2010).

150. T. Ripken, U. Oberheide, M. Fromm, S. Schumacher, G. Gerten, and H. Lubatschowski, "fs-Laser induced elasticity changes to improve presbyopic lens accommodation," *Graef Arch Clin Exp.* 246(6), 897-906 (2008).

151. A. Glasser, "Restoration of accommodation: surgical options for correction of presbyopia," *Clin Exp Optom.* 91(3), 279-295 (2008).

152. G. H. Reggiani Mello, and R. R. Krueger, "Femtosecond laser photodisruption of the crystalline lens for restoring accommodation," *Int Ophthalmol Clin.* 51(2), 87-95 (2011).

153. S. Yoon, S. Aglyamov, A. Karpiouk, and S. Emelianov, "A high pulse repetition frequency ultrasound system for the ex vivo measurement of mechanical properties of crystalline lenses with laser-induced microbubbles interrogated by acoustic radiation force," *Phys Med Biol.* 57(15), 4871-4884 (2012).

154. S. L. Jacques, and S. J. Kirkpatrick, "Acoustically modulated speckle imaging of biological tissues," *Opt Lett.* 23(11), 879-881 (1998).

155. C. B. Raub, V. Suresh, T. Krasieva, J. Lyubovitsky, J. D. Mih, A. J. Putnam, B. J. Tromberg, and S. C. George, "Noninvasive assessment of collagen gel microstructure and mechanics using multiphoton microscopy," *Biophys J.* 92(6), 2212-2222 (2007).

156. K. D. Mohan, and A. L. Oldenburg, "Elastography of soft materials and tissues by holographic imaging of surface acoustic waves," *Opt Express.* 20(17), 18887-18897 (2012).

157. G. Scarcelli, R. Pineda, and S. H. Yun, "Brillouin optical microscopy for corneal biomechanics," *Invest Ophthalmol Vis Sci.* 53(1), 185-190 (2012).

158. G. Scarcelli, P. Kim, and S. H. Yun, "In vivo measurement of age-related stiffening in the crystalline lens by Brillouin optical microscopy," *Biophys J.* 101(6), 1539-1545 (2011).

159. X. Liang, A. L. Oldenburg, V. Crecea, E. J. Chaney, and S. A. Boppart, "Optical micro-scale mapping of dynamic biomechanical tissue properties," *Opt Express.* 16(15), 11052-11065 (2008).

160. K. M. Kennedy, S. Es'haghian, L. X. Chin, R. A. McLaughlin, D. D. Sampson, and B. F. Kennedy, "Optical palpation: optical coherence tomography-based tactile imaging using a compliant sensor," *Opt Lett.* 39(10), 3014-3017 (2014).

161. J. Li, Z. Han, M. Singh, M. D. Twa, and K. V. Larin, "Differentiating untreated and cross-linked porcine corneas of the same measured stiffness with optical coherence elastography," *J Biomed Opt.* 19(11), 110502-110502 (2014).

162. S. R. Aglyamov, A. R. Skovoroda, H. Xie, K. Kim, J. M. Rubin, M. Donnell, T. W. Wakefield, D. Myers, and S. Y. Emelianov, "Model-based reconstructive elasticity imaging using ultrasound," *Int J Biomed Imaging.* 2007((2007).

163. X. Su, C. Vesco, J. Fleming, and V. Choh, "Density of ocular components of the bovine eye," *Optom Vis Sci.* 86(10), 1187-1195 (2009).

164. J. Vaughan, and J. Randall, "Brillouin scattering, density and elastic properties of the lens and cornea of the eye," *Nature.* 284(5755), 489-491 (1980).

165. Z. Han, C. Tao, D. Zhou, Y. Sun, C. Zhou, Q. Ren, and C. J. Roberts, "Air puff induced corneal vibrations: theoretical simulations and clinical observations," *J Refract Surg.* 30(3), 208-213 (2014).

166. Y. Kikkawa, and T. Sato, "Elastic properties of the lens," *Exp Eye Res.* 2(2), 210-215 (1963).

167. H. A. Weeber, and R. G. Van Der Heijde, "Internal deformation of the human crystalline lens during accommodation," *Acta ophthalmologica.* 86(6), 642-647 (2008).

168. N. M. Ziebarth, E. P. Wojcikiewicz, F. Manns, V. T. Moy, and J. M. Parel, "Atomic force microscopy measurements of lens elasticity in monkey eyes," *Mol Vis.* 13(52-55), 504-510 (2007).

169. F. A. Duck, "Medical and non-medical protection standards for ultrasound and infrasound," *Prog Biophys Mol Biol.* 93(1-3), 176-191 (2007).

170. H. M. Herbert, A. Viswanathan, H. Jackson, and S. L. Lightman, "Risk factors for elevated intraocular pressure in uveitis," *J Glaucoma.* 13(2), 96-99 (2004).

171. D. S. Friedman, J. T. Holbrook, H. Ansari, J. Alexander, A. Burke, S. B. Reed, J. Katz, J. E. Thorne, S. L. Lightman, and J. H. Kempen, "Risk of elevated intraocular pressure and glaucoma in patients with uveitis: results of the multicenter uveitis steroid treatment trial," *Ophthalmology.* 120(8), 1571-1579 (2013).

172. A. Grise-Dulac, A. Saad, O. Abitbol, J. L. Febbraro, E. Azan, C. Moulin-Tyrode, and D. Gatinel, "Assessment of corneal biomechanical properties in normal tension glaucoma and comparison with open-angle glaucoma, ocular hypertension, and normal eyes," *J Glaucoma.* 21(7), 486-489 (2012).

173. M. Detry-Morel, J. Jamart, and S. Pourjavan, "Evaluation of corneal biomechanical properties with the Reichert Ocular Response Analyzer," *Eur J Ophthalmol.* 21(2), 138-148 (2011).

174. M. J. Girard, J. K. Suh, M. Bottlang, C. F. Burgoyne, and J. C. Downs, "Biomechanical changes in the sclera of monkey eyes exposed to chronic IOP elevations," *Invest Ophthalmol Vis Sci.* 52(8), 5656-5669 (2011).

175. D. V. Litwiller, S. J. Lee, A. Kolipaka, Y. K. Mariappan, K. J. Glaser, J. S. Pulido, and R. L. Ehman, "MR elastography of the ex vivo bovine globe," *J Magn Reson Imaging.* 32(1), 44-51 (2010).

176. H. J. Burd, G. S. Wilde, and S. J. Judge, "An improved spinning lens test to determine the stiffness of the human lens," *Exp Eye Res.* 92(1), 28-39 (2011).

177. H. Baradia, N. Nikahd, and A. Glasser, "Mouse lens stiffness measurements," *Exp Eye Res.* 91(2), 300-307 (2010).

178. H. A. Weeber, G. Eckert, W. Pechhold, and R. G. van der Heijde, "Stiffness gradient in the crystalline lens," *Graefes Arch Clin Exp Ophthalmol.* 245(9), 1357-1366 (2007).

179. A. S. Vilupuru, and A. Glasser, "Optical and biometric relationships of the isolated pig crystalline lens," *Ophthalmic Physiol Opt.* 21(4), 296-311 (2001).

180. R. Sinkus, M. Tanter, T. Xydeas, S. Catheline, J. Bercoff, and M. Fink, "Viscoelastic shear properties of in vivo breast lesions measured by MR elastography," *Magn Reson Imaging.* 23(2), 159-165 (2005).

181. M. Tanter, J. Bercoff, A. Athanasiou, T. Deffieux, J. L. Gennisson, G. Montaldo, M. Muller, A. Tardivon, and M. Fink, "Quantitative assessment of breast lesion viscoelasticity: initial clinical results using supersonic shear imaging," *Ultrasound Med Biol.* 34(9), 1373-1386 (2008).

182. S. Wang, and K. V. Larin, "Shear wave imaging optical coherence tomography (SWI-OCT) for ocular tissue biomechanics," *Opt Lett.* 39(1), 41-44 (2014).

183. B. Y. Hsieh, S. Song, T. M. Nguyen, S. J. Yoon, T. T. Shen, R. K. Wang, and M. O'Donnell, "Moving-source elastic wave reconstruction for high-resolution optical coherence elastography," *J Biomed Opt.* 21(11), 116006 (2016).

184. V. Crecea, A. Ahmad, and S. A. Boppart, "Magnetomotive optical coherence elastography for microrheology of biological tissues," *J Biomed Opt.* 18(12), 121504 (2013).

185. A. Ahmad, J. Kim, N. A. Sobh, N. D. Shemonski, and S. A. Boppart, "Magnetomotive optical coherence elastography using magnetic particles to induce mechanical waves," *Biomed Opt Express.* 5(7), 2349-2361 (2014).

186. S. Rossi, M. Hallett, P. M. Rossini, and A. Pascual-Leone, "Safety, ethical considerations, and application guidelines for the use of transcranial magnetic stimulation in clinical practice and research," *Clin Neurophysiol.* 120(12), 2008-2039 (2009).

187. U. Herwig, A. J. Fallgatter, J. Hoppner, G. W. Eschweiler, M. Kron, G. Hajak, F. Padberg, A. Naderi-Heiden, B. Abler, P. Eichhammer, N. Grossheinrich, B. Hay, T. Kammer, B. Langguth, C. Laske, C. Plewnia, M. M. Richter, M. Schulz, S. Unterecker, A. Zinke, M. Spitzer, and C. Schonfeldt-Lecuona, "Antidepressant effects of augmentative transcranial magnetic stimulation: randomised multicentre trial," *Br J Psychiatry.* 191(441-448 (2007).

188. Y. Xu, and B. He, "Magnetoacoustic tomography with magnetic induction (MAT-MI)," *Phys Med Biol.* 50(21), 5175 (2005).

189. P. Grasland-Mongrain, J.-M. Mari, J.-Y. Chapelon, and C. Lafon, "Lorentz force electrical impedance tomography," *IRBM.* 34(4), 357-360 (2013).

190. X. Li, K. Yu, and B. He, "Magnetoacoustic tomography with magnetic induction (MAT-MI) for imaging electrical conductivity of biological tissue: a tutorial review," *Phys Med Biol.* 61(18), R249-r270 (2016).

191. P. Grasland-Mongrain, R. Souchon, F. Cartellier, A. Zorgani, J.-Y. Chapelon, C. Lafon, and S. Catheline, "Imaging of Shear Waves Induced by Lorentz Force in Soft Tissues," *Phys Rev Lett.* 113(3), 038101 (2014).

192. C. Li, G. Guan, Z. Huang, M. Johnstone, and R. K. Wang, "Noncontact all-optical measurement of corneal elasticity," *Opt Lett.* 37(10), 1625-1627 (2012).

193. S. Niehues, J. Unger, M. Malinowski, J. Neymeyer, B. Hamm, and M. Stockmann, "Liver volume measurement: reason of the difference between in vivo CT-volumetry and intraoperative ex vivo determination and how to cope it," *Eur J Med Res.* 15(8), 345 (2010).

194. W. M. Vannah, and D. S. Childress, "Modelling the mechanics of narrowly contained soft tissues: the effects of specification of Poisson's ratio," *J Rehabil Res Dev.* 30(205-205 (1993).

195. T. Deffieux, G. Montaldo, M. Tanter, and M. Fink, "Shear wave spectroscopy for in vivo quantification of human soft tissues visco-elasticity," *IEEE Trans Med Imaging.* 28(3), 313-322 (2009).

196. J. Y. Park, C. Y. Park, and J. M. Lee, "Estimation of saline-mixed tissue conductivity and ablation lesion size," *Comput Biol Med.* 43(5), 504-512 (2013).

197. C. K. Loo, A. Alonzo, D. Martin, P. B. Mitchell, V. Galvez, and P. Sachdev, "Transcranial direct current stimulation for depression: 3-week, randomised, sham-controlled trial," *Br J Psychiatry.* 200(1), 52-59 (2012).

198. K. Wawrzyn, V. Demidov, B. Vuong, M. K. Harduar, C. Sun, V. X. Yang, O. Doganay, V. Toronov, and Y. Xu, "Imaging the electro-kinetic response of biological tissues with optical coherence tomography," *Opt Lett.* 38(14), 2572-2574 (2013).

199. A. F. Pena, J. Devine, A. Doronin, and I. Meglinski, "Imaging of the interaction of low-frequency electric fields with biological tissues by optical coherence tomography," *Opt Lett.* 38(14), 2629-2631 (2013).

**First Author Journal Publications**

1. **Chen Wu**, Narendran Sudheendran, Manmohan Singh, Irina V. Larina, Mary E. Dickinson, and Kirill V. Larin. *"Rotational imaging optical coherence tomography for full-body mouse embryonic imaging."* Journal of Biomedical Optics 21(2), 26002 (2016).

2. **Chen Wu**, Shihao Ran, Henry H. Le, Manmohan Singh, Irina V. Larina, David Mayerich, Mary E. Dickinson, and Kirill V. Larin. *"Comparison of rotational imaging optical coherence tomography and selective plane illumination microscopy for embryonic study."* Biomedical Optics Express, 8(10), 4629-4639 (2017).

3. **Chen Wu**, Zhaolong Han, Shang Wang, Jiasong Li, Manmohan Singh, Chih-hao Liu, Salavat Aglyamov, Stanislav Emelianov, Fabrice Manns, and Kirill V. Larin. *"Assessing age-related changes in the biomechanical properties of rabbit lens using a coaligned ultrasound and optical coherence elastography system."* Investigative Ophthalmology & Visual Science 56(2), 1292-1300 (2015).

4. **Chen Wu**, Manmohan Singh, Zhaolong Han, Raksha Raghunathan, Chih-Hao Liu, Jiasong Li, Alexander Schill, and Kirill V. Larin. *"Lorentz force optical coherence elastography."* Journal of Biomedical Optics. 21(9), 090502 (2016).

5. **Chen Wu**, Aglyamov Salavat, Chih-Hao Liu, Zhaolong Han, Manmohan Singh, Kirill V. Larin. *"Assessing biomechanical properties of the porcine crystalline lens as a function of intraocular pressure with optical coherence elastography."* Biomedical Optics Express (**Under revision**)

6. Raksha Raghunathan, **Chen Wu**, Manmohan Singh, Chih-Hao Liu, Rajesh C. Miranda, and Kirill V. Larin. *"Evaluating the effects of maternal alcohol consumption*

*on murine fetal brain vasculature using optical coherence tomography."* Journal of Biophotonics 11(5), e201700238 (2018). (**Equal Contribution**)

## Intellectual Property

1. US Patent No. 9687145. “Optical Coherence Elastography to Assess Biomechanics and Detect Progression of Ocular and Other Tissue Degenerative Diseases.” June 2017.